Characterization of water sorption cycle in the cement microstructure of controlled oxide composition

École
polytechnique
fédérale
de Lausanne

2022

आचार्यात् पादमादत्ते
पादं शिष्यः स्वमेधया ।
पादं सब्रह्मचारिभ्यः
पादं कालक्रमेण च ॥

From the teacher is learned a quarter,
a quarter from the student's intelligence,
a quarter from peers,
and a quarter with the passage of time.

  -Haradatta (called "Ujjvalā") on the Āpastamba Dharmasūtra
(circa 11th century)

Acknowledgements

My love and gratitude go out to my family for always believing in me. Thanks to my mother for her never wavering confidence in me; my sister for words of encouragement and her witty humour; my brother-in-law for being a constant source of motivation; and my cute and innocent niece for the very real reminder on why we need to work hard towards creating a better and sustainable future. Also, I hope I've made you proud, dad; I'm sorry we didn't have more time.

Words fail me to describe the strength and motivation that I received from my husband during this PhD. A PhD in the time of a global pandemic is one of the most challenging things that I have done, and it would not have been possible without your continuous encouragement and positivity. Thank you for being my best friend, philosopher, and guide as and when I needed it.

December 2021   Leimen, Germany

Abstract

This thesis investigates the water vapour sorption behaviour of samples with maximized calcium-silicate-hydrate (C-S-H) content. Primarily, the role of heterogeneous and homogeneous cavitation has been studied during the drying of cementitious materials. Classical nucleation theory has been used to investigate the parameters affecting cavitation pressures. The volume balance analysis showed that homogeneous cavitation should occur in the gel pores of the inner product of the C-S-H. The results also indicate that it is crucial to consider the role of cavitation when using desorption isotherms for determining the pore size distribution.

Further, the effect of the hydration temperature on the microstructure of the samples has been investigated by analysing their water desorption behaviour. The amount of capillary and gel water content determined using water desorption isotherms were found to be in good agreement with the mass balance calculations. These mass balance calculations have been carried out by using multiple characterization techniques including X-ray diffraction (XRD), thermogravimetric analysis (TGA), proton nuclear magnetic resonance relaxometry (^{1}H NMR), and scanning electron microscope-energy dispersive X-ray analysis (SEM-EDX).

Thereafter, the water vapour desorption behaviour of the C-S-H samples synthesized using three different techniques has been compared. The first technique involved preparing a single-phase C-S-H using double decomposition and dropwise precipitation. The Gibbs Energy Minimization Software (GEMS) has been used to simulate the relationship between the calcium to silica (Ca/Si) ratio of synthetic C-S-H and the pH, as alkalis are introduced. In the second technique, the reactive belite binder has been hydrated to produce samples with maximized C-S-H content and the Ca/Si ratio has been varied using supplementary cementitious materials. The third technique involved mixing white cement with silica fume so that the content of C-S-H is maximized at the expense of portlandite.

Finally, the moisture absorption behaviour of the samples has been investigated using static as well as dynamic tests. Disjoining pressure-based concept of excess surface work has been used to explain the absorption behaviour. The sorption isotherms of Mobil Composition of Matter No. 41 (MCM-41) have been used to study the role of surface interactions on water sorption. The sorption behaviour of isopropanol as an adsorptive has also been discussed.

Résumé

Cette thèse étudie le comportement de sorption de la vapeur d'eau d'échantillons ayant une teneur maximale en calcium-silicate-hydrate (C-S-H). Princisopropanollement, le rôle de la cavitation hétérogène et homogène a été étudié pendant le séchage des matériaux cimentaires. La théorie classique de la nucléation a été utilisée pour étudier les paramètres affectant les pressions de cavitation. L'analyse du bilan volumique a montré que la cavitation homogène devrait se produire dans les pores du gel du produit interne du C-S-H. Les résultats indiquent également qu'il est crucial de prendre en compte le rôle de la cavitation lors de l'utilisation des isothermes de désorption pour déterminer la distribution de la taille des pores.

De plus, l'effet de la température d'hydratation sur la microstructure des échantillons a été étudié en analysant leur comportement de désorption d'eau. La quantité d'eau capillaire et de gel déterminée à l'aide des isothermes de désorption d'eau s'est avérée en bon accord avec les calculs de bilan massique. Ces calculs de bilan massique ont été effectués en utilisant de multiples techniques de caractérisation, notamment la diffraction des rayons X (XRD), l'analyse thermogravimétrique (TGA), la relaxométrie par résonance magnétique nucléaire protonique (1H NMR) et l'analyse par microscope électronique à balayage et rayons X à dispersion énergétique (SEM-EDX).

Ensuite, le comportement de désorption de la vapeur d'eau des échantillons C-S-H synthétisés à l'aide de trois techniques différentes a été comparé. La première technique consistait à préparer un C-S-H monophasé par double décomposition et précipitation en gouttes. Le logiciel de minimisation de l'énergie de Gibbs (GEMS) a été utilisé pour simuler la relation entre le rapport calcium/silice (Ca/Si) de la C-S-H synthétique et le pH, lorsque des alcalis sont introduits. Dans la deuxième technique, le liant bélite réactif a été hydraté pour produire des échantillons avec une teneur maximale en C-S-H et le rapport Ca/Si a été modifié en utilisant des matériaux cimentaires supplémentaires. La troisième technique consistait à mélanger du

ciment blanc avec de la fumée de silice de manière à maximiser la teneur en C-S-H au détriment de la portlandite.

Enfin, le comportement d'absorption d'humidité des échantillons a été étudié à l'aide d'essais statiques et dynamiques. Le concept de travail superficiel excédentaire basé sur la pression disjointe a été utilisé pour expliquer le comportement d'absorption. Les isothermes de sorption de Mobil Composition of Matter No. 41 (MCM-41) ont été utilisés pour étudier le rôle des interactions de surface sur la sorption de l'eau. Le comportement de sorption de l'isopropanol comme adsorbant a été également discuté.

Mots clés : Isothermes de sorption de la vapeur d'eau, C-S-H, cavitation, pâtes de ciment, séchage, sorption dynamique de la vapeur.

Zusammenfassung

In dieser Arbeit wird das Wasserdampfsorptionsverhalten von Proben mit maximiertem Calcium-Silikat-Hydrat (C-S-H) Gehalt untersucht. In erster Linie wurde die Rolle der heterogenen und homogenen Kavitation während der Trocknung von zementhaltigen Materialien untersucht. Zur Untersuchung der Parameter, die den Kavitationsdruck beeinflussen, wurde die klassische Keimbildungstheorie herangezogen. Die Volumenbilanzanalyse ergab, dass homogene Kavitation in den Gelporen des inneren Produkts des C-S-H auftreten sollte. Die Ergebnisse zeigen auch, dass die Rolle der Kavitation bei der Verwendung von Desorptionsisothermen zur Bestimmung der Porengrößenverteilung unbedingt berücksichtigt werden muss.

Ferner wurde die Auswirkung der Hydratationstemperatur auf die Mikrostruktur der Proben durch Analyse ihres Wasserdesorptionsverhaltens untersucht. Die mit Hilfe von Wasserdesorptionsisothermen ermittelten Kapillar- und Gelwassergehalte stimmten gut mit den Massenbilanzberechnungen überein. Diese Massenbilanzberechnungen wurden mit Hilfe verschiedener Charakterisierungstechniken durchgeführt, darunter Röntgenbeugung (XRD), thermogravimetrische Analyse (TGA), protonenmagnetische Kernresonanz-Relaxometrie (1H NMR) und Rasterelektronenmikroskop-Energiedispersions-Röntgenanalyse (SEM-EDX).

Anschließend wurde das Wasserdampfdesorptionsverhalten der C-S-H-Proben, die mit drei verschiedenen Techniken hergestellt wurden, verglichen. Bei der ersten Technik wurde ein einphasiges C-S-H durch doppelte Zersetzung und tropfenweise Ausfällung hergestellt. Die Gibbs Energy Minimization Software (GEMS) wurde verwendet, um die Beziehung zwischen dem Verhältnis von Calcium zu Siliciumdioxid (Ca/Si) von synthetischem C-S-H und dem pH-Wert zu simulieren, wenn Alkalien hinzugefügt werden. Bei der zweiten Technik wurde das reaktive Belit-Bindemittel hydratisiert, um Proben mit maximalem C-S-H-Gehalt herzustellen, und das Ca/Si-Verhältnis wurde mit Hilfe zusätzlicher zementhaltiger Materialien variiert.

Bei der dritten Technik wurde Weißzement mit Silikastaub gemischt, so dass der C-S-H-Gehalt auf Kosten des Portlandits maximiert wurde.

Schließlich wurde das Feuchtigkeitsaufnahmeverhalten der Proben mit statischen und dynamischen Tests untersucht. Zur Erklärung des Absorptionsverhaltens wurde das auf dem Trennungsdruck basierende Konzept der überschüssigen Oberflächenarbeit verwendet. Die Sorptionsisothermen von Mobil Composition of Matter No. 41 (MCM-41) wurden verwendet, um die Rolle der Oberflächeninteraktionen bei der Wasseraufnahme zu untersuchen. Das Sorptionsverhalten von Isopropanol als Adsorptionsmittel wurde ebenfalls diskutiert.

Schlüsselwörter: Wasserdampfsorptionsisothermen, C-S-H, Kavitation, Zementpasten, Trocknung, dynamische Dampfsorption.

Contents

List of figures

List of tables

Chapter 1   Thesis background

1.1   Overview

For centuries, concrete has remained one of the most used man-made materials for construction. This can be attributed to its low price, high performance, versatility, and durability. However, its extensive production is a major source of greenhouse gases emissions, generating about 8% of global CO_2 emissions. Understanding the factors contributing towards improved performance and lifespan of cementitious material is a key step towards reducing the carbon footprint of construction activities.

In the same lead, Marie Curie Initial Training Network (MC ITN) Engineered Calcium-Silicates-Hydrates for Applications (ERICA) aims to understand how the cementitious materials can be engineered at the nanoscale for improved applications. More information can be found at: https://www.erica-etn.eu/aims-and-objectives/.

ERICA consists of 13 individual but cross-related projects as shown in figure 1.1, which are aimed at creating a multiscale understanding of the cement hydrates. The programme is divided into three princisopropanoll Work Packages (WP): WP1 aims at synthesizing, characterizing, and modelling the 'as-grown' calcium-silicates-hydrates (C-S-H), the main binding phase of cementitious materials. WP2 addresses the reversible and irreversible changes that occur when the hydrates are dried and re-wetted. Finally, WP3 addresses the transport of water and ions into and out of the agglomerates and its upscaling for various applications. The research presented in this thesis is a part of WP2 and corresponds to project number 6. This project closely collaborated with the project 1 and 13 of WP1 and WP3, respectively.
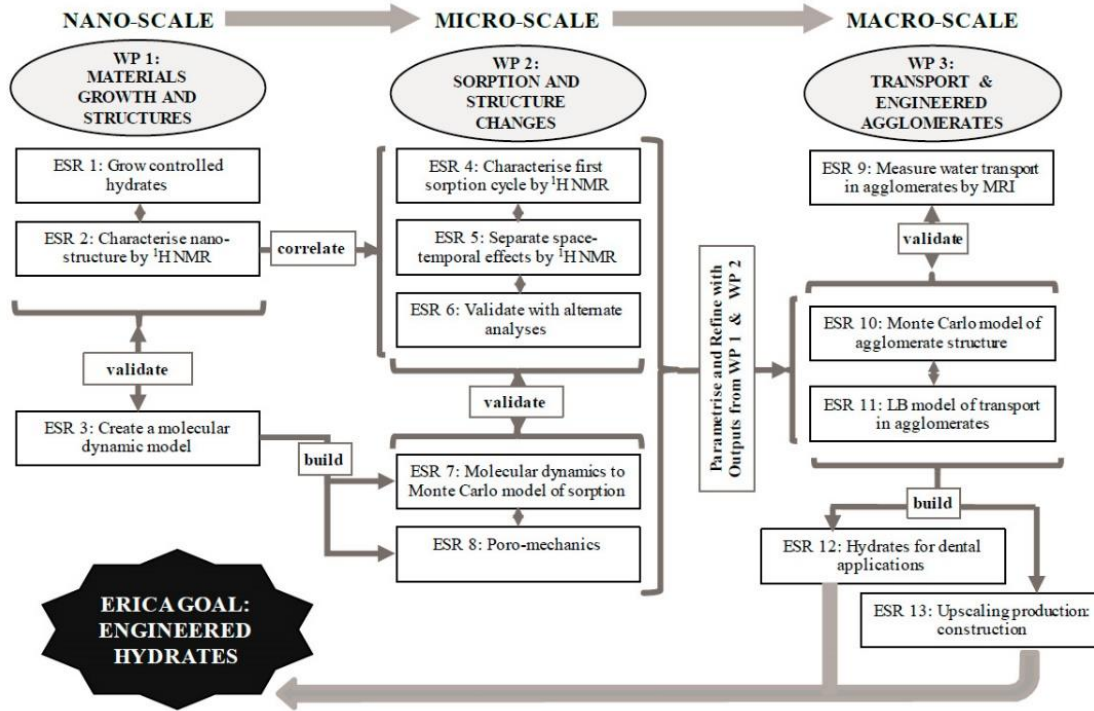
Figure 1.1: Organigram of the 13 ERICA projects and their interconnectivity. Project/ESR6 corresponds to the work done in this thesis.

1.2   Aims of the thesis

Durability assessments are crucial for predicting the service life of cementitious materials. Durability itself depends on several chemical and physical processes such as chloride or sulphate ingress, carbonation, and alkali-silica reaction among others[1–5]. However, all these chemical and physical processes, though diverse in nature, are mostly related to the moisture content and its transport. For example, chloride ions need a liquid phase to enter and diffuse in the cementitious materials. Carbonation has also been observed to be affected by the relative humidity (RH) (favoured in low RH regime [6–8] or high RH regime [9]). Moisture movement also affects the volumetric stability (creep and shrinkage) and the ability to resist cracking[10,11]. Therefore, the understanding of moisture behaviour is crucial for improving the prediction for the service life of cement-based materials.

Water vapour sorption isotherms (WVSIs) provide the relationship between the equilibrium moisture content of the material as a function of RH at a fixed temperature and thus, helps in understanding the moisture behaviour. WVSIs have been also expressed as "hygro-structural identity cards" of cement-based materials

as they have been used extensively to interpret the physical microstructure through interaction with moisture[12–14]. In this research work, WVSIs are acquired to understand the sorption behaviour of the hardened cement pastes with maximized C-S-H content.

The primary objective of this thesis is to identify the factors affecting the desorption behaviour of the samples. Drying in cement pastes is known to produce some microstructural changes. Therefore, the first desorption isotherms are of prime interest to obtain information about the "as-prepared" samples. Thereafter, the role of curing temperature on the microstructure is studied using water desorption isotherms along with other multiple characterization techniques. Furthermore, the desorption behaviour of C-S-H synthesized by ESR 1 and ESR 13, based on double decomposition and dropwise precipitation and the belite hydration technique, respectively has been compared with the C-S-H samples synthesized in this project (6). Finally, absorption isotherms have also been investigated with respect to microstructural changes.

1.3   Outline of the thesis

This thesis has the following 7 chapters.

Chapter 1: This chapter gives the general background and outline of the thesis.

Chapter 2: This chapter provides a basic overview of cement chemistry, hydration, development of the microstructure, and porosity. Thereafter, the theoretical framework for sorption in porous media has been introduced. Finally, the working principle of dynamic vapour sorption has been discussed, as it is the most used technique in this research work.

Chapter 3: In this chapter, the manuscript with the title 'The role of cavitation in drying cementitious materials' has been provided. The parameters that affect the cavitation pressures have been examined by using classical nucleation theory.

Chapter 4: In this chapter, the manuscript with the title 'The role of hydration temperature on the microstructure of the samples with maximized C-S-H

content' has been presented. Multiple techniques have been used to study the microstructure of the samples and the porosity assessment has been compared between dynamic vapour sorption and mercury intrusion porosimetry.

Chapter 5: This chapter presents the manuscript with the title 'The desorption behaviour of C-S-H synthesized using three different techniques". The C-S-H has been synthesized by (a) the double decomposition and dropwise precipitation method, (b) belite hydration, and (c) mixing white cement and silica fume. The microstructure of all the C-S-H samples has been characterized before water sorption analysis.

Chapter 6: This chapter provides insights into the water absorption behaviour of various samples with maximized C-S-H content. The role of disjoining pressure has been discussed.

Chapter 7: The final chapter presents a summary of the salient results presented in this thesis. Furthermore, their potential implications and possible future research directions have also been presented.

Chapter 2   Literature review

2.1   Hydration of Portland cement

The chemical composition of cement clinker is usually given as the weight percentage of oxides. The most important oxides that are present in clinker as clinker phases are CaO, SiO_2, Al_2O_3, and Fe_2O_3. The four main clinker phases that are found in cement clinker are tricalcium silicate (Ca_3SiO_5 or $3CaO.SiO_2$), dicalcium silicate (Ca_2SiO_4 or $2CaO.SiO_2$), tricalcium aluminate ($Ca_3Al_2O_6$ or $3CaO.Al_2O_3$), and tetracalcium aluminoferrite ($Ca_4Al_2Fe_2O_{10}$ or $4CaO.Al_2O_3.Fe_2O_3$). In cement chemistry, short notation is usually used and the four clinker phases are denoted as C_3S, C_2S, C_3A and C_4AF, respectively. Portland cement is the mixture of cement clinker and gypsum ($Ca\ SiO_4.2H_2O$) denoted as CSH_2.

When water is added to cement, several complex chemical reactions occur owing to the dissolution of clinker phases. Water reacts with C_3S, C_2S, C_3A, and C_4AF simultaneously, which results in different hydration products. These reactions are coupled to an extent, however, the hydration of the cement can be understood by the sum of hydration of the pure clinker phases that are summarized as follows [15–18]:

C_3S and C_2S react with water to produce C-S-H (calcium-silicate-hydrate) and CH (calcium hydroxide).

$$C_3S + (3 + m - n)H = C_n - S - H_m + (3 - n)CH \tag{2.1}$$

$$C_2S + (2 + m - n)H = C_n - S - H_m + (2 - n)CH \tag{2.2}$$
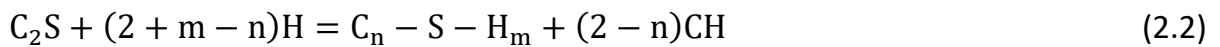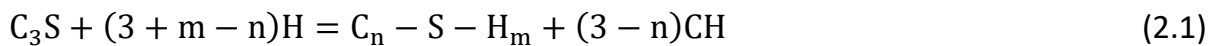
Here, m and n are variables that correspond to H/S and C/S ratios, respectively. Both m and n are dependent on the hydration conditions that include temperature, water to binder ratio, RH, presence of additives, and supplementary cementitious materials among others.

The hydration reactions of C_3A and C_4AF are more complex than that of C_3S and C_2S. The hydration of C_3A depends on the presence of sulphate ions. In the absence of sulphate ions, the reaction in pure water results in the formation of hydrogarnet (C_3AH_6). A considerable amount of heat is released in this reaction which results in the 'flash setting' of concrete that is detrimental to its workability and mechanical properties. This is avoided by the addition of gypsum (sulphate) that results in the formation of ettringite (AFt, $C_6A\bar{S}H_{32}$) in place of hydrogarnet. When the sulphate is depleted, ettringite becomes unstable, resulting in the formation of monosulfoaluminates (Afm). These phases can exist simultaneously in a hardened cement paste. The above-mentioned reactions are summarized as follows:

- In absence of sulphates

$$2C_3A + 21H \rightarrow C_2AH_9 + C_2AH_8 \rightarrow 2C_3AH_6 + 9H$$
(2.3)

- In presence of sulphates

$$2C_3A + 3C\bar{S}H_2 + 26H \rightarrow C_6A\bar{S}H_{32}$$
(2.4)
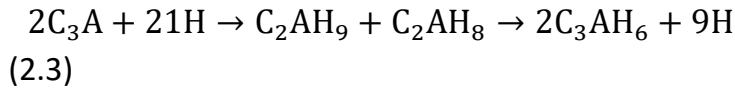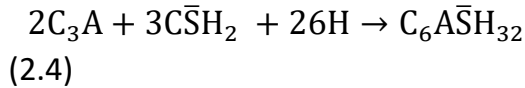
- In case of sulphate depletion

$$2C_3A + C_6A\bar{S}H_{32} + 4H \rightarrow 3C_4A\bar{S}H_{12}$$ (2.5)
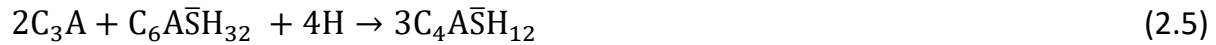
In case of C_4AF, it initially reacts with gypsum and water to form ferrite-ettringite (where some aluminium is replaced by iron, as indicated by brackets (A,F)), alumina hydroxide, and portlandite. Thereafter, as sulphates deplete it further reacts with the formed ettringite to produce garnets as described by the following equations:

$$C_3AF + 3C\bar{S}H_2 + 30H \rightarrow C_6(A,F)\bar{S}_3H_{32} + (A,F)H_3 + CH$$ (2.6)

$$C_4AF + C_6(A,F)\bar{S}_3H_{32} + 2CH + 23H \rightarrow 3C_4(A,F)\bar{S}_3H_{18} + (A,F)H_3$$ (2.7)
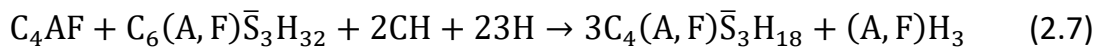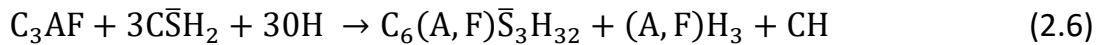
As most of these processes are exothermic, isothermal calorimetry can be used to identify the different phenomenon in cement hydration. Figure 2.1 shows a typical heat evolution curve for the hydration of Portland cement. The hydration process can mainly be divided into four phases based on its heat evolution behaviour[69].

In phase A, the preinduction/initial period, calcium and hydroxide ions are released from the cement grains as the water interacts with cement along with other alkaline ions such as sodium and potassium. The alkalinity of the solution increases as further C_3A reacts. Phase B is the induction or dormant stage in which the rate of hydration slows down, as explained by the protective layer theory or delayed nucleation and growth theory. Thereafter, in phase C or the acceleration stage, the rate of hydration increases for C_3S and the hydration for C_2S also becomes noticeable. The rate of hydration attains its maximum value at the end of this stage. Finally, in phase D or post-acceleration stage, the rate of hydration gradually decreases. C_2S continues to hydrate and the main hydration product C S H grows. 'Sulfate depletion' peak is marked as E and is a feature which is often found in the measurements of Portland cement systems and corresponds to the start of secondary aluminate hydration.
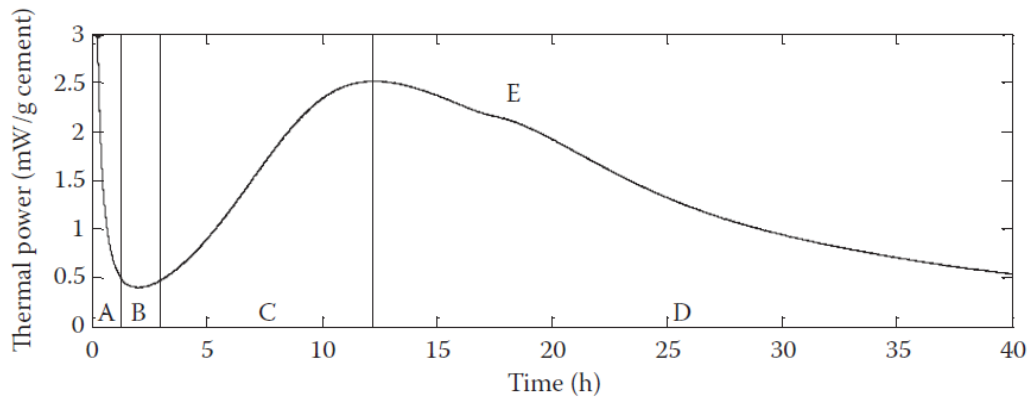
Figure 2.1: A typical heat evolution curve during the hydration of Portland cement[69].

2.2   Microstructure of cementitious materials

2.2.1   Hydration products

As mentioned in the previous section (2.1), the main products of hydration of Portland cement are calcium-silicate-hydrate (C-S-H), calcium hydroxide (CH), ettringite (AFt), and monosulfate aluminate (AFm). CH, Aft, and AFm are crystalline products whereas C-S-H is poorly crystalline in nature. Generally, it has been observed that C-S-H has a crystalline structure at the short-range, whereas at the long-range it is amorphous. C-S-H is the most important phase as it occupies more

than 60% of the total volume in hydrated cement paste and controls several important mechanical properties. Owing to its variable chemical composition, nanostructure, and morphology, the exact nature of C-S-H is still debated. The following section (2.2.2) provides a summary of the models that have been proposed to explain the structure of C-S-H.

2.2.2   Various models to explain the structure of C-S-H

The structure of C-S-H has been defined at a multi-scale level. At an atomic level, the structure of C-S-H has been compared to the natural minerals such as 1.4 nm Tobermorite (Ca/Si = 0.83, molar water content: 42%) and jennite (Ca/Si = 1.5, molar water content: 42%). Figure 2.2 shows the schematic illustration of the layered structure of 1.4 nm Tobermorite[20].
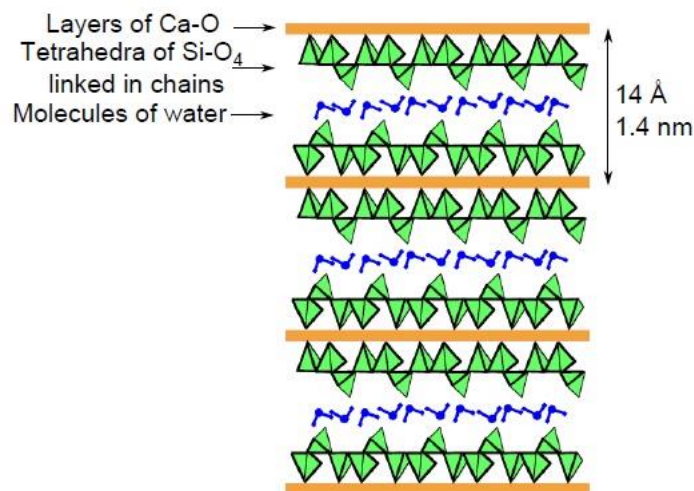
Figure 2.2: The layered structure of 1.4 nm Tobermorite [20].

At the larger scales, **Power and Brownyards (P-B)** (1946-47), proposed a model for the microstructure of the cement paste, and particularly its main binding phase C-S-H, using water vapour sorption isotherms[14,21]. The paste volume was treated as an assembly of three main components, which were unreacted cement paste, hydration products, and capillary pores. It was proposed that hydrated cement is a colloid that is composed of small, layered units that form a porous product. Figure 2.3 (a) shows the structure of C-S-H after the Powers and Brownyard model.

This model was improved by **Feldman and Sereda** (1968-71) who considered that the C-S-H sheet does not have an ordered, layered structure but is rather composed of an irregular array of single layers in which water molecules are incorporated in the C-S-H structure[22–24]. Further, these surfaces are covered by the hydroxyl groups that make hydrogen bonds with the surrounding water molecules. A schematic of the C-S-H model proposed by the authors and the water movement upon drying and wetting has been shown in figure 2.3 (b) and (c), respectively.
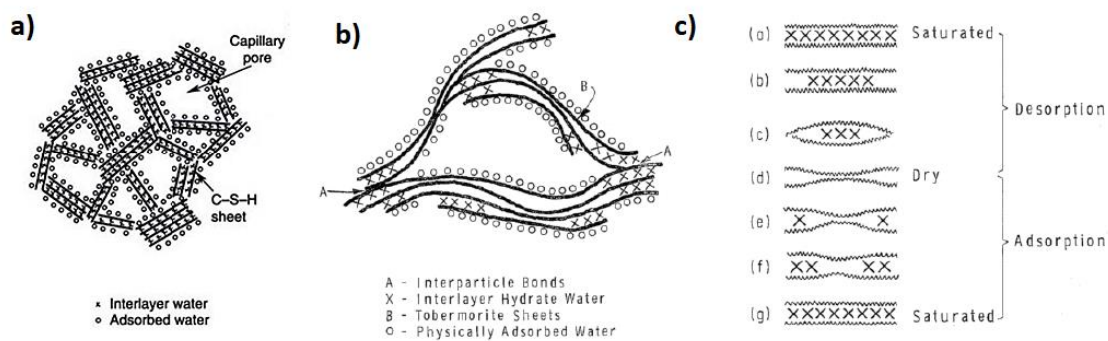
Figure 2.3: (a) Powers model for the structure of cement gel (b) Feldman and Sereda's model of C-S-H. (c) Proposed mechanism for water movement within cement paste upon drying and wetting according to the model of Feldman and Sereda.[14,21,24]

Whittmann (1973) proposed the **Munich model** that described the C-S-H as a three-dimensional arrangement of colloidal particles[25,26]. These arrangements are significantly affected by the moisture conditions, such that it depends on the equilibrium of the attractive Van der Waals forces that brings the surface together and the repulsive pressure that is exerted by the strongly adsorbed film on the outer surface. It was also proposed that water vapour is not capable of measuring the surface area of cement owing to the interaction of C-S-H with vapour, which agrees with the model suggested by Feldman and Sereda.
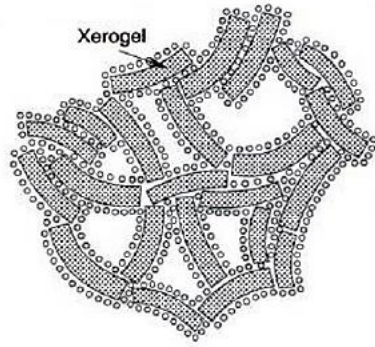
Figure 2.4: Munich model for C-S-H [25,26].

Jennings and co-workers proposed the **colloidal model (CM I)** and later refined it in 2008 as **CM II** [27–30]. In the original model, the authors proposed that the cement paste can be described as a colloid made up of particles called globules, which flocculate together to make a porous C-S-H network. Small-angle neutron and X-Ray scattering techniques were used to investigate the nanostructure of these globules (figure 2.5). This was found to be essentially comparable to the tobermorite structure, with disordered calcium silicate layers having water between them. The presence of three types of water could be detected including physically adsorbed water, physically bound water, and chemically bound water.

In the refined CM II model, the following four types of pores were proposed:

- Within the globule, two locations of water were identified as the interlayer spaces and the intraglobular pores (IGP) that had sizes less than 1 nm. The removal of water from interlayer spaces induces the collapse of the structure. However, water removal from IGP does not induce any changes in the microstructure.

- Further, small gel pores (SGP) were defined as pores that were filled with water trapped between the globules and which percolates to the outer regions. The reported characteristic size was between 1-3 nm in diameter.

- Large gel pores (LGP) were identified as the pores or spaces arising from the overlap of globular flocks, and the reported characteristic size for LGP was 3-12 nm in diameter.

- Finally, the capillary pores were identified as pores filled with free water that was non-intrinsic to C-S-H, and the lower limit for the size was found to be 10 nm.
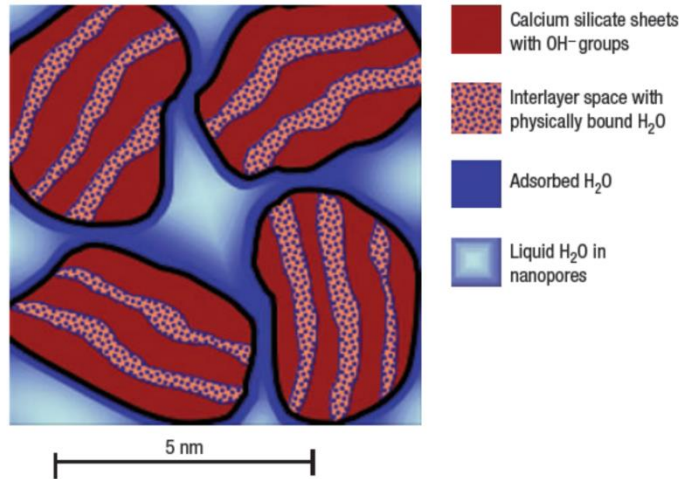
Figure 2.5: Schematic illustration of a C-S-H globule as determined using SANS and SAXS experiments [25,26].

Several other morphologies for C-S-H have also been reported such as C-S-H gel of Type I and Type II, with needle-shaped and honeycomb morphologies, respectively. At the early stage of curing, C-S-H is formed in the shape of long fibres as proposed by Locher et.al. [19]. Thereafter, Type III C-S-H is formed which has the shape of small disks or spheres that is also referred to as short fibres. C-S-H has also been distinguished by outer and inner product, in which the inner product of C-S-H is formed in the space left by the dissolving cement grains. The outer product is formed in the spaces originally filled with water. Middle and late products as well as groundmass and phenograins are also some classifications that have been proposed for C-S-H[19]. The recent **building block model of C-S-H** proposes that it is composed of a defective, nanocrystalline tobermorite with missing bridging silicate tetrahedra, resulting in a decrease of silicate chain length. Further, the silanol groups are deprotonated silanol groups with its charge compensated by additional calcium ions[31].

2.2.3   Porosity in cementitious materials

The porosity and the state of water present in cementitious materials significantly influence their mechanical properties. These are also largely governed by the water to binder ratio, age, and curing conditions among others. As shown in figure 2.6, the porosity spans from nanometers to millimetres [32].
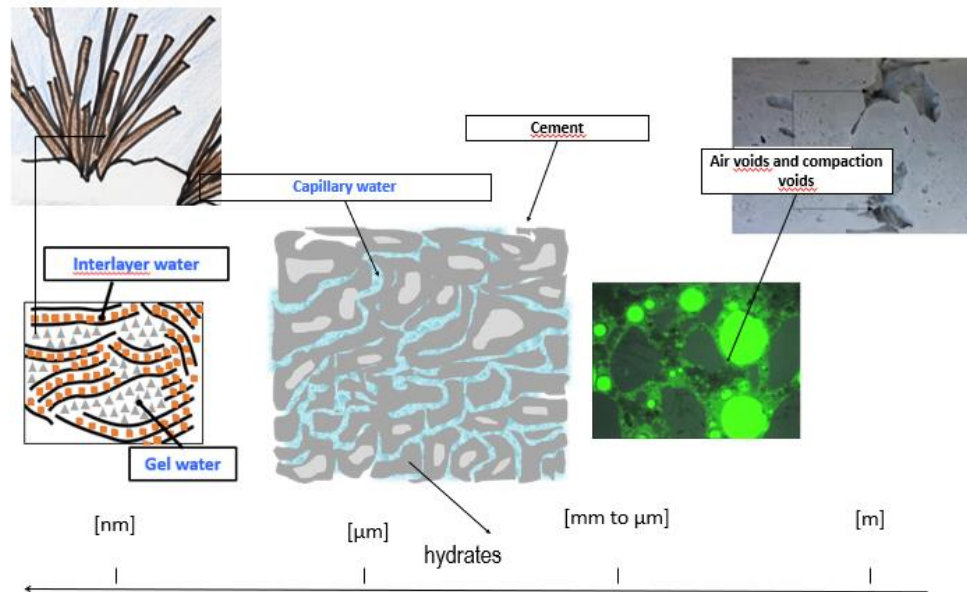
Figure 2.6: Porosity in concrete / cement. Adapted from [32].

Water has also been classified according to the type/size of the pore that confines it. In cement, water can exist in interlayer spaces, as gel porosity, in the interhydrates, and as capillary porosity. The characteristic sizes of these pores are a matter of investigation and the limit is debatable. Table 2.1 provides a summary of several investigations made in this direction.

Table 2.1 Classification of water-filled spaces and pores in hydrated cement paste according to different sources. Adapted from [33].

Pore type /space	IUPAC Classification	Description	Characteristic sizes
Interlayer C-S-H Spaces	Micropores	Spaces between the C-S-H sheets	≤ 1 nm [26,29,34,35] 1.5 nm [36] 1.8 [37] <2 nm [38]
Gel pores	Mesopores	Spaces between agglomerated C-S-H sheets	1–3 nm (small gel pores) [29] 3–12 nm (large gel pores between the globule flocks)[29] 2–3 nm [26,34] 7 nm [37] 2–8 nm[38]
Interhydrate pores		Pores between C-S-H Needles	~10 nm [26,34] >8 nm [38] 50 nm [37]
Capillary pores	Macropores	Larger pores remaining after consumption of water	>8 nm [38] ≥100 nm [26,34,37]

2.3   Sorption in porous materials: common definitions and theoretical framework

Adsorption is a surface phenomenon that involves the adhesion of atoms, ions, or molecules at the liquid-solid interface. As shown in figure 2.7, the solid is called the adsorbent and the gas/vapour, which is capable of being adsorbed, is called the adsorptive. The gas/vapour in the adsorbed state is called adsorbate.

Absorption is bulk/volume phenomenon and the adsorptive permeates the entire volume of the adsorbent.
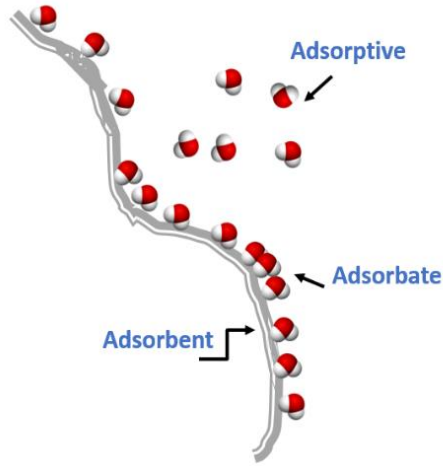
Figure 2.7: Representation of adsorbent, adsorbate, and the adsorptive in a system.

Adsorption and absorption together are called **sorption**. However, in the literature concerning cement, sorption is often referred to as absorption. Hence, the same notation shall be followed in this thesis unless mentioned otherwise[12,39,40].

Similarly, **desorption** is the removal of adsorbate from the adsorbent.

The amount of adsorptive adsorbed/removed on an adsorbent depends on the absolute temperature T, the pressure P, and the interaction potential E. Hence, at a given equilibrium pressure and temperature, the weight W of adsorbate on a unit weight of adsorbent is given by

$$W = f(P, T, E) \tag{2.8}$$

Generally, W is measured under isothermal conditions. Hence, equation (2.8) reduces to

$$W = f(P, E) \tag{2.9}$$

A plot of W as the function is P is known as the **desorption or absorption isotherm** of a given vapor-solid interface.

2.3.1 Factors governing sorption in porous materials

The sorption behaviour of fluids in porous materials is governed by several factors. The most important factors are fluid-solid interactions and the effect of pore size.

2.3.1.1 Effect of fluid-solid interactions

Based on the strength of the fluid-solid interactions, all adsorption processes can be divided into the two categories of **chemisorption** (chemical sorption) and **physiosorption** (physical adsorption).

Chemisorption is usually characterized by chemical specificity and often requires activation energy. Further, owing to reaction or surface dissociation, the chemical nature of the adsorptive may change, because of which the original form of the adsorbate cannot be removed on desorption. This in turn makes the process irreversible. In chemisorption, true equilibrium may be achieved very slowly (or in practice not at all). In several cases of adsorption of gases by solids, at a constant gas pressure, the extent of adsorption has been found to increase with an increase in temperature in this mode of sorption[41].

On the other hand, physisorption is characterized by intermolecular forces or Van der Waals forces and activation energy is not required. Further, the chemical nature of adsorbate does not change significantly and remains chemically identical to that in the fluid phase. This makes the process reversible. Equilibrium may be achieved slowly and is governed by temperature (extent of adsorption decreases with increase in temperature) and rate-determining transport processes. In several systems where hysteresis is observed, the equilibrium has also been found to be metastable.

It is important to note that in many practical cases, a sharp distinction between the two sorption processes cannot be made and intermediate cases exist such as adsorption involving strong hydrogen bonds or weak charge transfer.

2.3.1.2   Effect of Pore size

The International Union of Pure and Applied Chemistry (IUPAC) proposed categorizing pores based on their internal width[1]: micropores have a pore size less than 2 nm, mesopores have pore sizes between 2 and 50 nm, and macropores have pore sizes greater than 50 nm[42].

In micropores, fluid-solid interactions govern the sorption behaviour. In fact, the adsorption potential of the opposite walls overlaps as shown in figure 2.8(a). In mesopores, both fluid-wall and fluid interaction governs sorption and leads to capillary condensation, figure 2.8(b). In macropores, sorption is the same as that on nearly flat surfaces, figure 2.8(c).
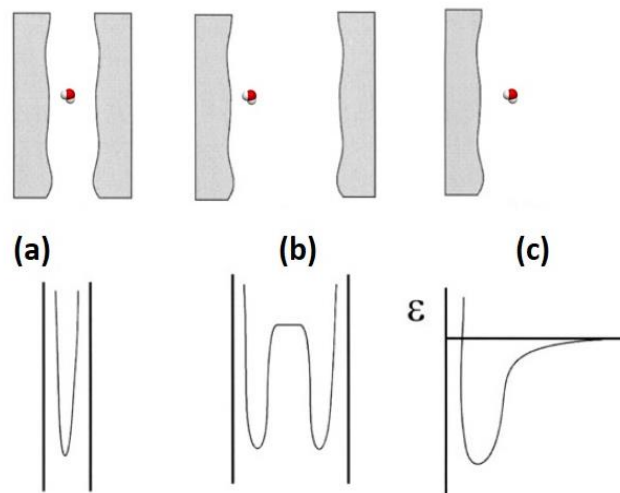
Figure 2.8: Schematic illustration of adsorption potential, E, on (a) planar, nonporous surface; (b) mesopore; (c) micropore. Adapted from [40].

Adsorption of fluid on porous materials is dependent on the pore size. According to the IUPAC classification, physiosorption isotherms are classified into six categories as shown in figure 2.9. Type I (a) and (b) isotherms are observed for microporous materials. The difference between the two types arises from the size of

---

[1] The diameter in case of a cylindrical pore and as the distance between opposite walls in case of a slit pore.

micropores involved. Type I (a) isotherms are observed for materials that have micropores of size less than 0.7 nm, whereas Type I (b) isotherms result from micropores of size between 0.7-2 nm. Type II isotherms are generally obtained for non-porous or microporous materials, in which monolayer sorption is followed by multilayer sorption. Type III isotherms are observed for materials where fluid-wall interaction is weak, or the adsorbate does not wet the surface completely. Such isotherms have been commonly reported for materials where the adsorptive is water. The Type IV isotherm are commonly observed for mesoporous materials and can be (a) with or (b) without hysteresis [described further in section (2.4)]. A significant increase in sorption amount of Type IV isotherm is usually associated with **capillary condensation**, which is a first-order phase transition between a liquid filled in a pore and the vapour adsorbed on the pore wall and coexisting with the liquid film. This reflects the shift in bulk transition, as the vapour condenses to liquid-like phase in pores at a pressure less than the saturation pressure, owing to the attractive fluid-wall interactions.
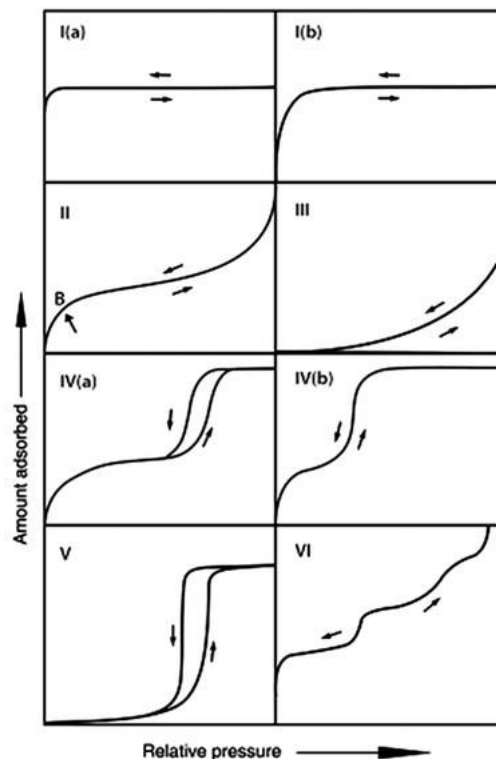
Figure 2.9: IUPAC classification of physisorption isotherms. Adapted from [32].

Type V isotherms, like Type III isotherms, are observed for mesoporous materials where the interaction between adsorbate and adsorbent is weak. In the rare Type VI isotherm, a multilayer formation is observed, where each step indicates the formation of a new layer of adsorbate on a smooth, non-porous surface.

2.4   Hysteresis in porous materials

Hysteresis is the difference in the adsorptive content in the desorption and absorption isotherm at a given RH and, as shown in figure 2.9, is common for mesoporous adsorbents. There are several explanations and models for the occurrence of hysteresis. Some of the common explanations have been discussed as follows.

Occurrence of hysteresis in mesoporous materials :

a) In a single cylindrical pore, differences in the shape of the meniscus during evaporation (hemispherical) and condensation (cylindrical) results in hysteresis[42].

b) In a single pore, hysteresis could occur due to the difference in metastable fluid states during absorption and desorption. This refers to the delay in pore condensation or evaporation[41,43,44].

c) The interconnectivity of the porous network within the materials with a wide distribution of pore sizes would result in hysteresis due to pore blocking effects. For example, if a pore has access to the external gas phase only through a narrow constriction, the pore will be filled at higher relative pressures. However, it will only empty after the narrow constriction has been emptied[42,45,46]. A difference in the value of contact angle during desorption and absorbtion would also result in hysteresis.

A correlation between the shape of the hysteresis loop and the texture of the adsorbent (pore geometry, pore size distribution, connectivity) is widely accepted. IUPAC provided a general classification of hysteresis loops into types H1, H2, H3, and H4, as shown in figure 2.10. Generally, H1 hysteresis is observed in mesoporous materials with uniform cylindrical pores or agglomerates or compacts of approximately uniform spheres. H2 hysteresis has been observed for materials that have more complex pore systems with ink-bottle pores. Type H3 hysteresis is commonly observed in slit-shaped pores and shows significantly high adsorption at high relative pressure. In the same way, type H4 loops are also often associated with narrow slit pores but now also include pores in the micropore region[42].
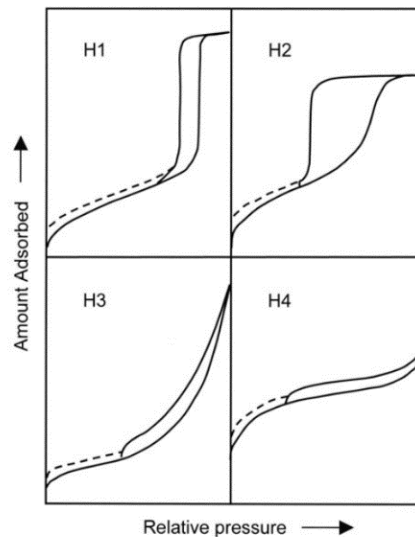
Figure 2.10: IUPAC classifications of hysteresis loops[42].

As shown by the dashed lines in figure 2.10, low-pressure hysteresis is also observed in several materials. This may be associated with the change in swelling of the non-rigid pores or the irreversible uptake of the molecules in pores that have the same width as that of the adsorptive molecule. Furthermore, chemisorption is also responsible for low-pressure hysteresis in certain cases. Low-pressure hysteresis is commonly observed in WVSIs of cementitious materials. An example has been shown in figure 2.11 that corresponds to water sorption isotherms and scanning isotherms for hydrated cement paste (hcp) with water to binder (w/b) ratio of 0.45 and 0.35[12].

19
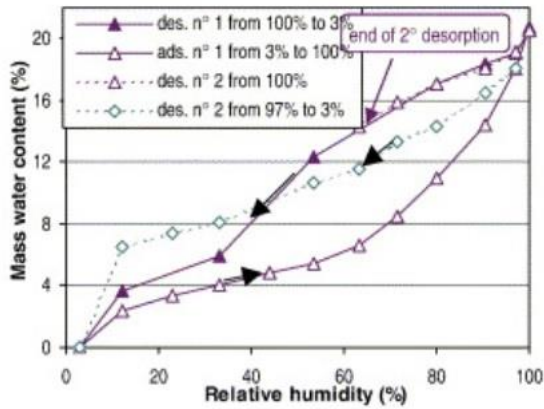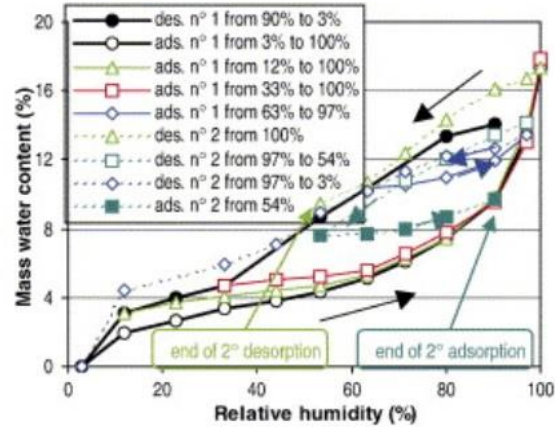
Figure 2.11: Water vapour desorption, absorption, and scanning isotherms within various RH ranges for hcp samples with a w/b of (a) 0.45 and (b) 0.35.[12]

The low-pressure hysteresis in cementitious materials has been explained by several hypotheses. Feldman *et al.* suggested that in the interlayer space, very thin planar layers of aqueous condensate localizes, which results in low-pressure hysteresis[22]. Many researchers proposed that the pore collapses owing to the removal of water from the C-S-H interlayer and results in low-pressure hysteresis[30][12].

However, Bazant and co-workers debated the pore collapse explanation as it has not been documented experimentally. They explained the low-pressure hysteresis by snap-through instabilities that follow different paths during absorption and desorption[47]. Furthermore, they also presented a model in which the adsorbed layer is in a metastable state[48]. As shown in figure 2.12, during sorption this adsorbed layer can combine into non-uniform patches or droplets at low RH because of the short-range intermolecular attractions. If humidity is increased, the adsorbate gets thermodynamically unstable and separates into locally stable low- and high-density phases [figure 2.12 (b)]. After a certain higher RH, the adsorbate again becomes homogeneous with a higher density [figure 2.12 (c)]. During desorption, the homogenous adsorbate destabilizes and forms the stable high- and low-density phase, which consecutively forms into low-density adsorbate [figure 2.12 (e)and (f)]. Therefore, the low-pressure hysteresis occurs due to the difference in metastable states in absorption and desorption.
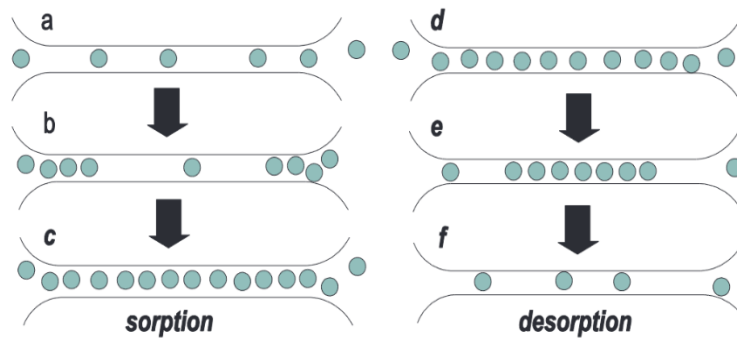
Figure 2.12: Molecular condensation in monolayer-thick pore during absorption and desorption[48].

2.5 Dynamic vapour sorption: working principle and technique

Dynamic Vapour Sorption (DVS) is a gravimetric sorption technique that measures how much adsorptive is taken up by the adsorbent at a given RH.
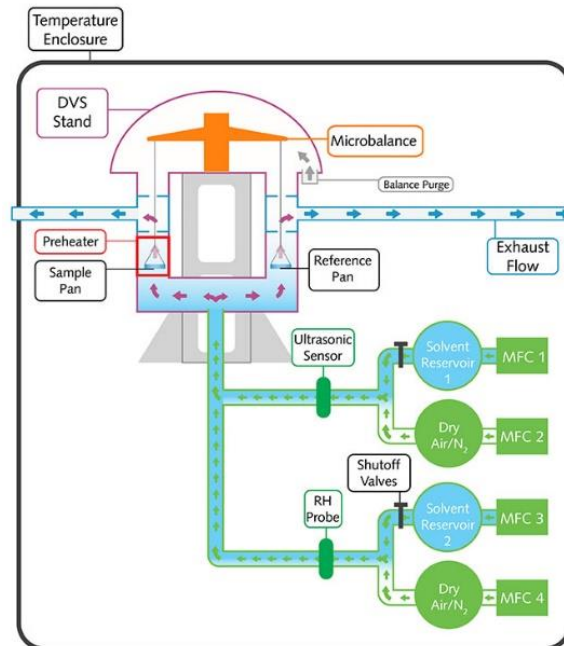
Figure 2.13: Schematic illustration of a DVS equipment. Credits: Surface Measurement Systems.

The desired RH is achieved by mixing a carrier gas (nitrogen or air) and the adsorptive from the solvent reservoir as shown in figure 2.13. The solvent reservoir acts as a vapour source for either water or any other organic solvent. To achieve precise control over RH, the ratio of saturated adsorptive (solvent reservoir) and dry gas flow is maintained with mass flow control that is combined with real-time vapour concentration monitoring.

For independent verification of the RH, humidity probes are also situated below the sample and the reference holders. The sample is suspended from a recording microbalance which measures the weight change during absorption or desorption as a known concentration of the selected vapour flows over it. The microbalances are capable of measuring mass changes at a resolution of 0.1 ug with peak-to-peak noise of less than or equal to 0.2 ug. The temperature of the whole unit can be controlled by the user and is precisely regulated using closed-loop conditions such that the adsorptive vapour pressure at the sample is constant. The isolation valves are situated near the adsorptive reservoir that ensures that the contamination of the sample area is prevented.

In this thesis, two DVS equipment have been used: DVS Adventure and DVS Endeavour (Surface measurement systems) and their pictures have been provided in figure 2.14. Even though the working principle is the same for both these devices, the major difference lies in the number of sample pans. DVS Adventure can measure one sample at a time, whereas DVS Endeavour can acquire sorption isotherms of 5 samples, simultaneously.
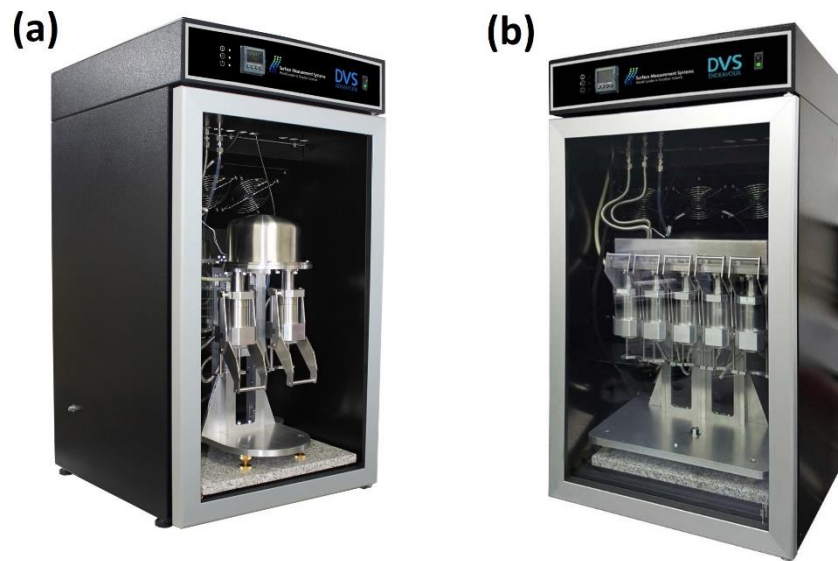
Figure 2.14: Picture of (a) DVS Adventure and (b) DVS Endeavour equipment. Credits: Surface Measurement Systems.

Chapter 3   The role of cavitation in drying cementitious materials

Monisha Rastogi[ab], Arnaud Müller[a], Mohsen Ben Haha[a], Karen L. Scrivener[b]

[a]HeidelbergCement Technology Center, Leimen, Germany

[b]École polytechnique fédérale de Lausanne, Switzerland

Contribution of the doctoral candidate: Writing of the first manuscript draft, experimental design, carrying out the experiments presented in the manuscript, editing and compilation of input from the other authors.

Abstract

This study examines the role of cavitation in drying cementitious materials. Classical nucleation theory is used to understand and study the parameters that influence cavitation pressures. The water desorption isotherms indicate that both heterogeneous and homogeneous cavitation occur during the drying of saturated cement pastes and the commonly observed large moisture loss at 0.3 p_v/p_{sat} can be explained by homogeneous cavitation. This homogeneous cavitation is suggested to occur in the gel porosity of the inner product that is disconnected from the rest of the porosity. The findings of this study indicate that it is important to consider the effects of cavitation for the characterization of pore sizes from moisture desorption isotherms.

Keywords: Cavitation, calcium-silicate-hydrate, dynamic vapour sorption, bubble nucleation, cement, shrinkage reducing admixture

3.1   Introduction

Water vapour sorption isotherms (WVSIs) provide the relationship between external relative humidity (RH) and evaporable water content. WVSIs are also referred to as the 'hygro-structural' identity card of cementitious materials[12,13]. They have a history of providing insights into the microstructure of hardened cement pastes (hcp) and are helpful in understanding durability[14,22,29,49]. Nevertheless, the interpretation of water isotherms is not straightforward and has been the subject of much debate[30,39,50,51]. Drying may produce some irreversible changes in the microstructure, so the first desorption isotherm is considered to be of most interest for providing information on the as-cured (undried) hcp[52–54]. A particular feature of desorption isotherms is a distinct steep water loss or "step" at around 0.3 p_v/p_{sat} [2] (or 30 % RH)[40,55,56].

Baroghel-Bouny investigated several cement pastes and concretes with a broad range of water-to-cement ratios from 0.20 to 0.84. This step at around 0.3 p_v/p_{sat} was observed for all the samples[12]. Following the Barrett, Joyner, and Halenda (BJH) method this large moisture loss at 0.3 p_v/p_{sat} was interpreted as a large population of pores of entry radius around 1.5 nm [12,56–58]. However, such a large number of pores in this size range is not observed by other techniques such as ^{1}H NMR relaxometry[59].

Other arguments have been used to explain the step at 0.3 p_v/p_{sat}, such as microstructural changes, phase-specific dehydration of Ca^{2+} ions or a change in basal space of calcium-silicate-hydrate (C-S-H) [12][60,61]. But these explanations fail to explain the occurrence of this step at the same place in the desorption isotherm irrespective of the differences in the composition of raw materials, water to binder ratio, or synthesis procedure.

---

[2] Symbols p_v and p_{sat} denote the pressure imposed by the vapour and the saturation vapour pressure of water at the given temperature, respectively.

Water (pore solution) filled spaces in cementitious materials can be divided into four categories according to ^{1}H NMR relaxometry[26,62]:

(I) Interlayer spaces corresponding to the water present between the C-S-H sheets, with a size of around 1 nm.

(II) Gel pores, which are usually viewed as spaces between agglomerated C-S-H sheets, with characteristic size between 2-8 nm.

(III) Interhydrate pores that exist between C-S-H "needles" with a characteristic size of 8-10 nm.

(IV) Capillary pores, which are larger pores containing solution or air, with sizes spanning from 10 nm to several micrometres.

In a porous material, evaporation occurs by receding meniscus. However, owing to the confinement of fluid in nanopores, cavitation can occur resulting in a drastic change from the liquid phase into the vapour phase. Evaporation induced cavitation has been reported to occur in several domains of biology, materials science, and engineering such as in mineral inclusions, trees, propagation of spores, lipid bilayers, and cell membranes among others[63–65].

Recently, Maruyama *et al.* considered the role of cavitation in hcp during water vapour desorption. The authors investigated several porous materials including zeolites, portlandite, and a model mesoporous material MCM-41. The high moisture loss observed around 0.3 p_v/p_{sat} in the desorption isotherm of these materials was attributed to cavitation. Furthermore, the authors reported the influence of dissolved ions and surface effects such as hydrophobicity/hydrophilicity on the cavitation pressure[66].

This paper aims to explain cavitation in the desorption isotherm of hcp using classical nucleation theory (CNT). According to CNT, the surface tension at the liquid-vapour interface σ_{lv} is an important parameter that affects cavitation pressure. To change the surface tension, the sorption temperature was increased and samples were made with surface reducing admixture (SRA), as SRA also reduces surface tension at the liquid-vapour interface.

3.2   Cavitation theory

Based on the energy of nucleation, cavitation in a porous medium can be either homogenous or heterogeneous.

3.2.1   Homogeneous cavitation

Capillary pressure is induced in the pore liquid as drying takes place in the nanopores. The strong cohesion of water molecules enables water to resist very high negative pressures. However, as this pressure becomes more negative, intermolecular forces dominate over short-range repulsion forces and the liquid becomes metastable. This metastability is ended by either the homogeneous nucleation process (with a nucleation barrier) arising from the thermodynamic instability or the spinodal breakdown (without a nucleation barrier, also known as the tensile strength of the liquid) which can be attributed to the mechanical instability. The stress for homogeneous cavitation in water has been predicted to be 140 MPa at 25 ℃[67]. This is discussed in more detail in the supplementary information SI3 (I) by using the phase diagram of water.

The classical nucleation theory gives a thermodynamic framework for homogeneous cavitation. The expressions that allow quantification of this process such as the rate of homogenous nucleation of vapour bubbles, cavitation stress, the energy cost of bubble creation, and free energy barrier are provided by CNT and discussed in SI3 (II) [equations 3(i)-(v)]. It can be observed that the surface tension at the liquid-vapour surface energy σ_{lv} , strongly influences the cavitation stress by affecting the rate of homogeneous nucleation of bubbles, the energy cost of bubble creation, and the free energy barrier. Therefore, by changing σ_{lv}, the role of homogeneous cavitation can be investigated and understood.

3.2.2   Heterogeneous cavitation

The energy barier of nucleation is lower for heterogeneous nucleation [readers are directed to SI3 (III), equation 3(vi)]. The nucleation mechanism corresponding to heterogeneous cavitation is less understood but is governed by

factors such as surface imperfections and wettability contrasts, which are abundant in cementitious materials. Nevertheless, stress of around 20-25 MPa has been associated with heterogeneous cavitation of water in a variety of porous materials[65,68].

3.3   Materials and methods

As C-S-H is the continuous phase that dominates the pore structure of cementitious materials, samples were prepared with the aim to maximize the amount of C-S-H and minimise the amounts of other phases. To achieve this, finely ground white cement clinker was used for its high content of calcium silicate phases. To produce more C-S-H, silica fume (SF) was added to react with calcium hydroxide.

White cement clinker provided by Aalborg Portland was used in this study. The phase composition of the anhydrous powder analysed through X-ray diffraction (XRD) Rietveld refinement was found to be: C_3S (65.3 wt.%), C_2S (28.8 wt.%), C_3A (1.9 wt.%), and CH (2.51 wt.%) with the rest of the phases below 1%. To maximise hydration and minimise remaining anhydrous grains, the clinker was ground to d_{50} and d_{90} values of ~6 and 18 μm, respectively. The condensed silica fume (SF) was provided by ELKEM. It was composed of 96% SiO_2 with a d_{50}~ 0.478 μm. Table 3.1 shows the X-ray fluorescence (XRF) analysis of the white cement clinker and SF used in this study.

Table 3.1 - XRF analysis of the white cement clinker and SF ; values are given in weight %.

Chemical content	SiO_2	Al_2O_3	TiO_2	MnO	Fe_2O_3	CaO	MgO	K_2O	Na_2O	SO_3	P_2O_5	total XRF - 950 °C
Clinker	25.25	2.07	0.05	0.01	0.13	69.91	0.64	0.15	0.22	0.19	0.14	99.48
SF	96.19	0.19	0	0.01	0	0.23	0.45	0.8	0.16	0	0.07	99.1

The paste composition was optimized through multiple iterations to maximize the content of C-S-H in the resulting hydrated cement paste samples. The formulation selected was: ground white-cement clinker 84.5% by wt., hemihydrate 5.5% by wt., and silica fume 10% by wt. This binder was mixed with water at a water-to-binder (w/b) ratio of 0.7 using a high-speed mechanical mixer Ultraturrax at 24000 rpm for 90 s with a further 30 s during lowering the speed (24000-0 rpm).

Samples were cured underwater at 55 ℃ for 90 days to accelerate the hydration. The set of samples prepared using this procedure are referred to as the 'control samples' in this article. With the objective of reducing surface tension at the liquid-vapour interface, two other sets of samples were produced, incorporating a liquid shrinkage reducing admixture (SRA) (0.2% solid content). The SRA was provided by SIKA (SIKA control 40) and added at 2% and 3% by weight of water. The samples with SRA were prepared following the same procedure as the control sample and were also cured at 55 ℃ for 90 days.

For XRD analysis and Rietveld refinement, fresh discs of 3 mm thickness were cut from the sealed cylinders after 90 days. A Bruker D8 Advance diffractometer with monochromatic Cu-Kα radiation (λ = 1.541 Å) and a step-size of approximately 0.02° was used to acquire data in the range of 5° to 70° (2θ). The degree of hydration of clinker phases was calculated by Rietveld refinement using Topas software, with quartz as the external standard following a pre-described procedure[69].

Further microstructural characterization were made on samples that were dried using the solvent exchange method. Solvent exchange was selected as it is considered to be the least damaging among drying techniques[70–72]. A disc of ~2.5-3 mm thickness was cut from the hardened cement cylinders and stored in isopropanol, which was replaced after 1 hour and 1 day. After 3 days of isopropanol immersion, the samples were stored under vacuum, in desiccators with silica gel beads for 14 days. Thereafter, this disc was crushed and 30(± 2) mg of the resulting powder was used for thermogravimetric analysis (TGA) (Netzsch STA 449 F3 ''Jupiter") from 20 to 700 ℃ in a nitrogen atmosphere with a heating rate of 10 ℃/min. The portlandite content was calculated from the TGA analysis with the tangent method[69].

Scanning electron microscope (SEM) images were acquired using an FEI Quanta 200 microscope coupled with a Bruker XFlash 4030 EDS detector. A 2 mm thick disc (solvent exchanged) was impregnated with epoxy resin in a mould under vacuum. The impregnated samples were polished down to 1 μm using diamond sprays and a petrol-based lubricant.

For porosity analysis of the control sample, mercury intrusion porosimetry (MIP) was carried out on crushed solvent exchanged samples that were investigated

up to a maximum pressure of 400 MPa using a Pascal 140/440 Porosimeter (Thermo Scientific). The surface tension of the mercury was considered to be 0.48 N/m.

[1]H nuclear magnetic resonance (NMR) Carr–Purcell–Meiboom–Gill (CPMG) measurements were made on undried control sample for analysis of the state of water. The crushed sample was equilibrated at 0.95 p_v/p_{sat} for 6 months. The experiments with 256 echoes, logarithmically spaced between 60 μs and 0.5 s, were made on a benchtop magnet operating at 20 MHz using Kea[2] spectrometer (Magritek, New Zealand). The 90° excitation pulse length was 6 μs and the spectrometer dead time was 10 μs. Eight points per echo were acquired with a dwell time of 1 μs. The experimental repetition time (τ_{rd}) was 1 s and the number of scans was 1024.

Sorption isotherms were acquired using dynamic vapour sorption (DVS). Measurements were carried out on as-cured saturated samples using a DVS Adventure (Surface Measurement Systems). The samples were cured for 90 days before the measurement of the isotherms. The sorption temperature was 20 °C for all samples. The control sample was also measured at 50 °C. Samples weighing ~25 mg were crushed and subjected to drying or desorption with the starting point at 0.98 p_v/p_{sat}, followed by step-wise data acquisition from 0.98 p_v/p_{sat} to 0.03 p_v/p_{sat} with a step size of 0.05. For the control sample, data were also acquired at additional steps. The initial mass from the balance (once the balance was considered stable) was also recorded and considered to be nearly equal to the mass of the saturated sample m_s at ($p_v/p_{sat} \approx 1$). Mass equilibrium was identified as the point at which the mass change was less than 0.0001 mg/min or exceeding the assigned time limit of 1440 mins for the control sample. For all other samples (including the control sample measured at 50 °C) the time limit was 1440 mins for 0.98 p_v/p_{sat} step and 480 mins at all other steps. If the equilibrium was not attained in the given time interval, the moisture content was extrapolated by using the asymptotic function for moisture ratio MR:

$$MR = \frac{m_t - m_0}{m_{eq} - m_0} = 1 - \exp(-k_m t)$$

(3.1)

m_t : mass at time t

m_0: mass at time 0

m_{eq}: Equilibrium mass at a given p_v/p_{sat}

k_m: fitting parameter

This equation has been previously used in several investigations on moisture sorption and is based on the analytical solution of the diffusion equation[39,58,73,74]. The data is normalized to per gram of dry cement paste.

3.4   Results and discussion

3.4.1   Microstructural analysis of the hydrated cement pastes

The phase assemblage of the hydrated cement pastes for the control sample and the sample prepared with 3 % SRA were quantified after 90 days of hydration at 55 °C using Rietveld refinement. The Portlandite content was additionally measured by TGA. Table 3.2 provides information on the phase assemblage of the samples. The data are normalised per 100 g of paste.

Table 3.2 – Phase assemblage of the pastes quantified using XRD Rietveld refinement and portlandite content quantified using TGA. Measurement error is ± 2%.

Phase		Control sample	Sample with 3 % SRA
Alite (C_3S)		3.4	5.6
Belite (C_2S)		4.3	3.9
Ettringite (AFt)		3.6	5.5
Portlandite (CH)	Rietveld	8.1	7.6
	TGA	8.9	10.6
Amorphous content		80.5	77.2

The proportion of the remaining clinker phases and hydrated compounds of the control sample and the sample prepared with the SRA were considered equivalent within experimental error. The degree of hydration of clinker phases was ~ 90 % after 90 days, for all the samples investigated.
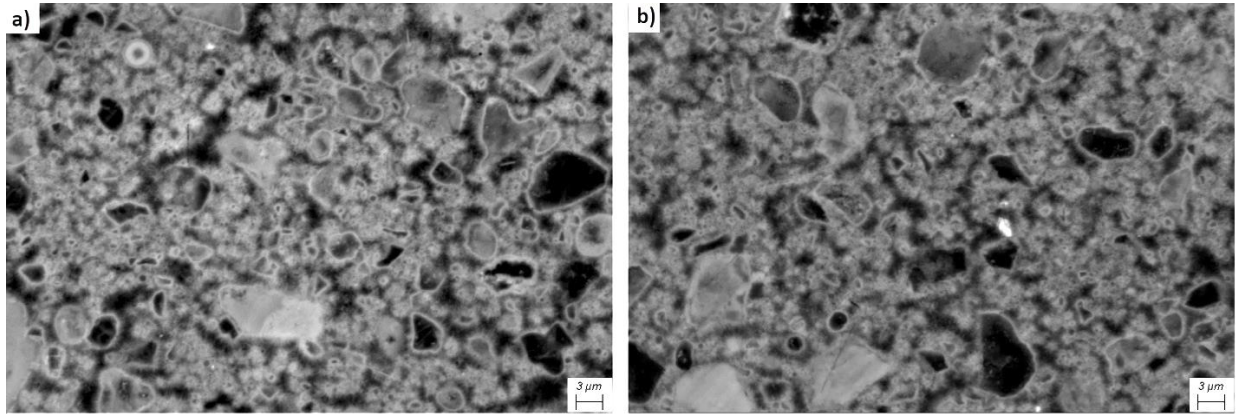
Figure 3.1: SEM micrographs for (a) control sample and (b) sample prepared with 3 % SRA.

Figures 3.1 (a) and (b) show the SEM micrographs for the control sample and the sample prepared with 3 % SRA, respectively. No distinguishable difference was observed between the microstructure of the two samples. EDS analysis indicated that the Ca/Si ratio of the C-S-H was ~1.4-1.5 for both samples.

The pore structure of the control sample was studied by MIP and ^{1}H NMR. Figure 3.2 (a) shows the intruded pore volume (MIP) as a function of applied pressure. The Washburn equation was used to calculate the equivalent pore entry diameter, considering a contact angle of 140°. The critical pore diameter (which is defined as the pore diameter with the steepest recorded slope of the cumulative intrusion curve) was estimated to be 56 nm. Additionally, the threshold pore entry diameter (interpreted as the minimum diameter that is geometrically continuous throughout the whole sample) was found to be 66 nm. An additional scale considering a contact angle of 120° for the determination of pore diameter is also presented in figure 3.2. The equivalent critical and threshold pore entry diameters were found to be 38 and 44 nm, respectively.

Figure 3.2 (b) shows the multi-exponential fitting applied to analyse the ^{1}H NMR CPMG data to separate the mobile water signal into different components. The fitting of NMR data was done by minimizing the squared error of fit. As the sample was equilibrated at 0.95 p_v/p_{sat} before the NMR measurement, the capillary pores were partly empty. Therefore, only the signal from gel and interlayer spaces was considered in this analysis. The ratio of the relaxation times was fixed such that the T_2 value of gel pore water was equal to 3 times the T_2 value of interlayer water, as observed in earlier studies[62,75]. The shortest time and different amplitudes were allowed to vary, as applied in several previous studies [76,77]. T_2 values of 192 and 576 μs were attributed to the interlayer and gel pore water of the C-S-H, respectively. These accounted for 26.6% and 56.2% of the total signal, leading to a gel to interlayer amplitude ratio of 2.13, which is comparable to several other studies for mature white cement pastes[32][59].
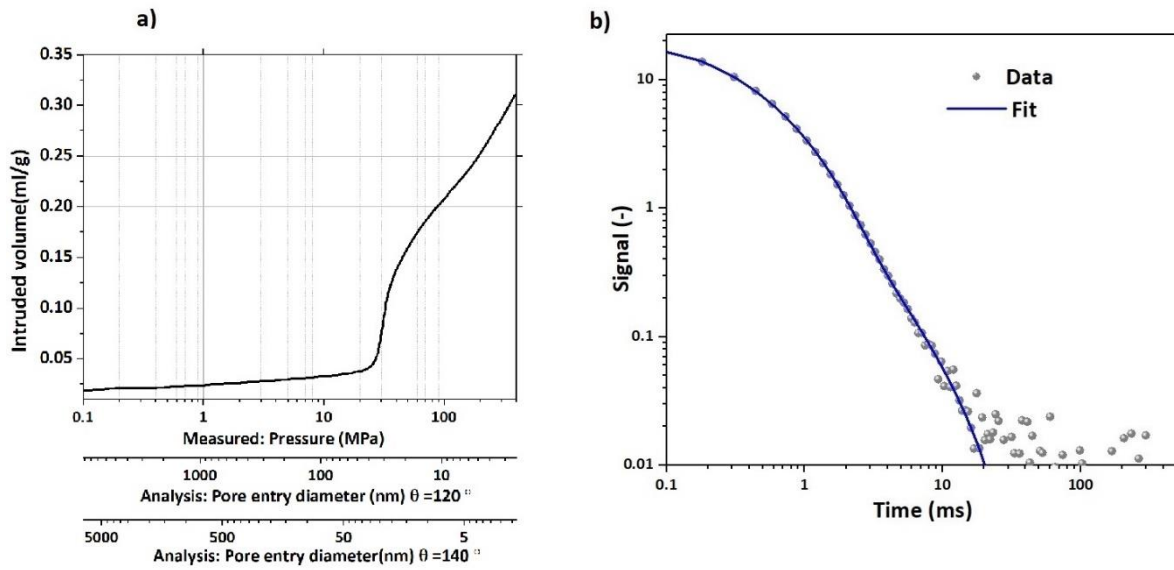
Figure 3.2: Cumulative pore volume as obtained from the MIP analysis using 140° as a contact angle (additional scale corresponding to pore entry diameter with contact angle 120 ° has also been plotted); and (b) CPMG decay data as obtained from ^{1}H NMR relaxometry for the control sample and the corresponding multi-exponential fit.

3.4.2 Sorption isotherms and BJH pore size distributions

Figure 3.3 shows the desorption isotherm of the control sample, samples prepared with 2% and 3% SRA (measured at 20°C), and for the control sample measured at 50 °C.

Using the BJH method, the pore size distributions from the desorption isotherms were obtained and are shown in figure 3.4 (see SI3 (V) for details). Distinct sharp peaks can be observed around 1-2 nm for all the samples. As previously discussed, there is no other evidence for the porosity to be dominated by pores in this size range. Moreover, for the same sample where the desorption was measured at 20 and 50 °C, the pore size of the peaks shifts from 1.1 to 2 nm, which makes no physical sense. Further analysis of the desorption experiments showed that there is always a large step first at 0.3-0.4 and another at 0.8-0.7 p_v/p_{sat} (as indicated by arrows in figure 3.3), which also corresponds to higher equilibration times.
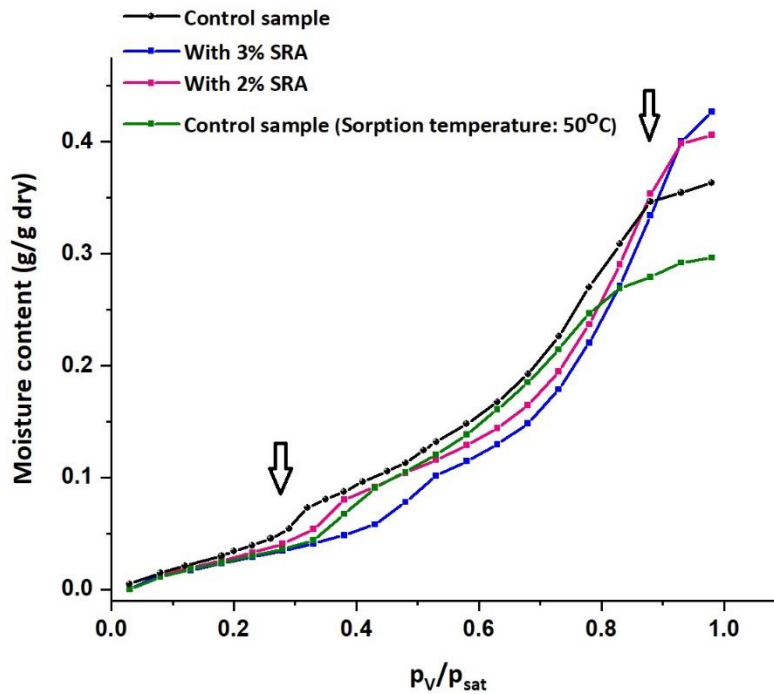
Figure 3.3: Desorption isotherms for the control sample, samples prepared with 2% and 3 % SRA at 20 °C, and for the control sample acquired at higher sorption temperature of 50 °C. The arrows indicate two steep steps in the desorption isotherms of all the samples, except for the 50 °C at higher p_v/p_{sat}.
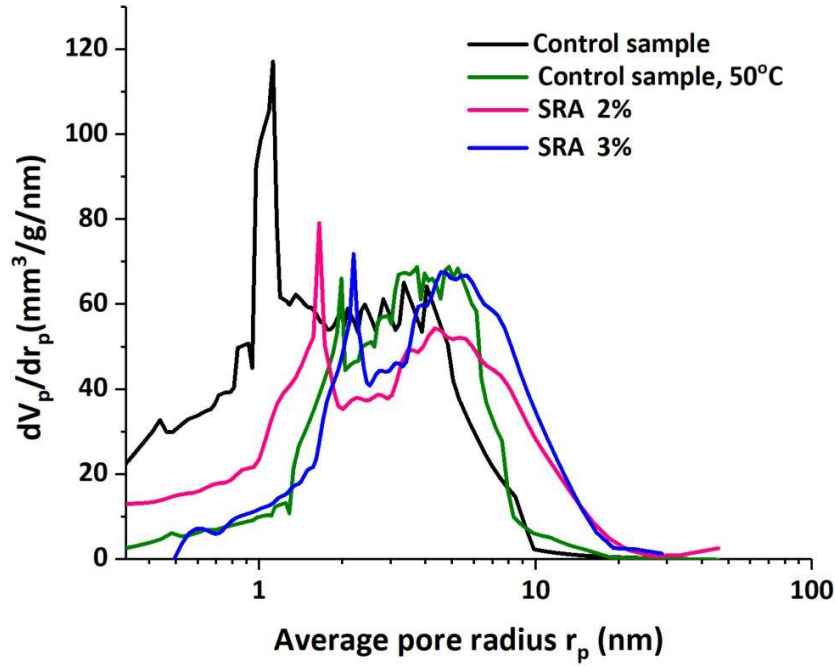
Figure 3.4: BJH pore size distributions obtained from the desorption isotherm of the various samples considered in this study.

Figure 3.5 shows an example of the detailed analysis of sorption data at different p_v/p_{sat}. Figure 3.5 (a) shows the moisture loss (%) as a function of equilibration time for the control sample, whereas figure 3.5 (b) shows this analysis for the sample prepared with 3% SRA, in the range 0.03-0.5 p_v/p_{sat}. Figure 3.5 (c) and (d) shows this analysis for equilibration time as a function of the induced-stress in the pore liquid [as calculated using Kelvin equation SI3 (IV), equation 3(vii)) for the control sample and sample prepared with 3 % SRA, respectively.
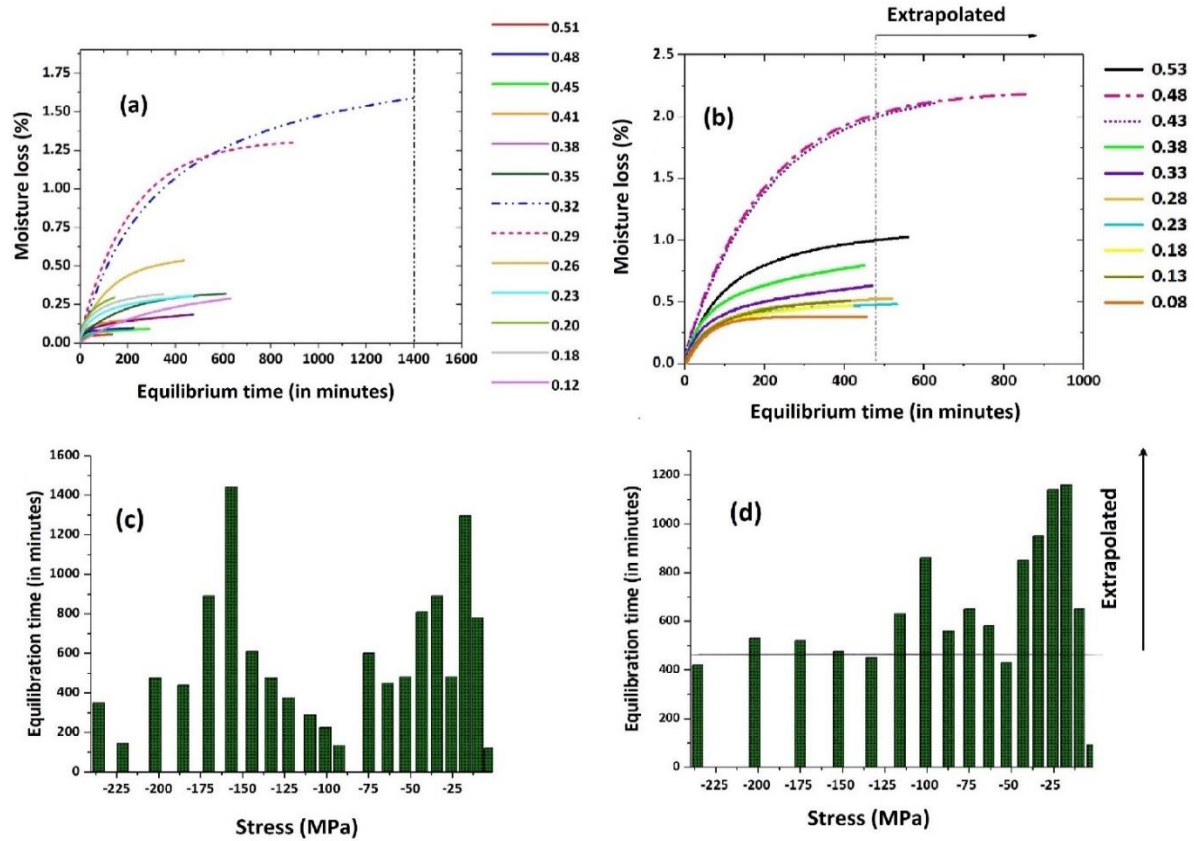
Figure 3.5: Moisture loss as a function of equilibration time in the desorption regime of 0.03-0.5 p_v/p_{sat} for (a) the control sample and (b) the sample prepared with 3 % SRA, measured at 20 °C. Data with high moisture losses are indicated with a dotted line. Equilibration time as a function of stress for (c) the control sample and (d) sample prepared with 3 % SRA.

A summary of these specific p_v/p_{sat} steps with their corresponding equilibration time and the induced stress in the pore liquid has been provided in Table 3.3. Furthermore, the predicted values for homogeneous (SI3 (II) equation 3(ii)) and heterogeneous cavitation for various samples are also provided.

Table 3.3 – The values for the p_v/p_{sat} associated with higher moisture loss, equilibration time, and the corresponding induced stress in the pore liquid for samples considered in this study. The predicted values for homogeneous and heterogeneous cavitation are also provided.

Sample	p_v/p_{sat} steps with higher moisture loss	Equilibration time (min) for dm/dt = 0.0001 mg/min	Induced stress (MPa) Error (±2)	Cavitation stress, predicted by CNT, homogeneous cavitation (MPa)	Stress predicted for heterogeneous cavitation (MPa)
Control sample	0.32-0.29	1420	150-165	145.5	
	0.83-0.78	1350	20-25		20-25
Control sample 50°C	0.43-0.48	960	115-120	121.6	
					20-25
2 % SRA	0.38-0.33	840	128-135	118.4	
	0.88-0.83	900	17-23		20-25
3 % SRA	0.48-0.43	870	95-105	98.0	
	0.88-0.83	1150	17-23		20-25

3.4.3 Cavitation phenomena

In general, there is good agreement with the stress at these specific steps and the stress predicted for homogeneous and heterogeneous cavitation, which gives strongly supports the hypothesis that evaporation induced cavitation is occurring at these steps.

Assessing heterogeneous cavitation around 0.8 p_v/p_{sat} according to the modified Kelvin-Laplace equation (SI3 (V), equation 3(ix)) reveals that it would occur in the capillary pores with diameter >18 nm that are accessible only by smaller necks (or throats). From MIP analysis of the control sample, the minimum pore size that is continuous throughout the geometry (threshold pore entry diameter) was found to be 66 nm. Therefore, pores bigger than 18 nm are likely to be interconnected with smaller pores making the heterogeneous cavitation feasible. Furthermore, the absence of heterogeneous cavitation in the desorption isotherm of the control

sample measured at 50°C could be attributed to pores >18 nm that would already be empty at the starting p_v/p_{sat} in a 50 °C environment.

In general, the stresses predicted by CNT for homogeneous cavitation are also in good agreement with the stresses induced from the specific steps around 0.3 and 0.4 p_v/p_{sat} for all the samples. Some differences can be expected as the surface tension of water is dependent on several other factors such as the contact angle, the radius of curvature (Tolman type corrections), nanoconfinement, and presence of ions, the exact determination of which is beyond the scope of this study[78,79]. Furthermore, the desorption data were collected at each 0.05 p_v/p_{sat} (0.03 for control sample) which limits determination of the exact value of p_v/p_{sat} at which homogeneous cavitation occurs. Nevertheless, it can be concluded that reducing σ_{lv} reduces the magnitude of the capillary stress that can be sustained before homogeneous cavitation. This could be attributed to a decrease in the work of nucleation and the energy barrier associated with the creation of bubbles (SI3 (II), equations 3(ii, iii, and v)).

However, for homogeneous cavitation to occur at an induced tension of ~150 MPa (0.3 p_v/p_{sat}), cavitation bubbles must be larger than 1 nm (SI3 (II), equation 3(iv)). This indicates that homogeneous cavitation events cannot take place in the interlayer space of the C-S-H.

Moreover, homogeneous cavitation is observed at ~0.3 p_v/p_{sat}, which is well separated from the heterogeneous cavitation events at ~0.8 p_v/p_{sat}. This implies that the pores in which homogeneous cavitation occurs must be isolated from the rest of the porosity, and particularly from the capillary pore space in which the heterogeneous cavitation occurs. To investigate this, we determined the water content and volume distribution in detail by a combination of ^{1}H NMR relaxometry and mass and volume balance analysis.

3.4.4 Water content distribution of the control sample

Two methods were used to determine the water content distribution in the control sample.

In the first method, the amount of water in the C-S-H was first evaluated using a calcium mass balance. The mass of calcium within the C-S-H was calculated

by subtracting the calcium present in ettringite and portlandite from the calcium provided by the reacted clinker phases. A H_2O/Ca ratio of 0.482 [59] was used to calculate the amount of water present in the C-S-H interlayer. A gel/interlayer ratio of around 2.13, as measured using ^{1}H NMR CPMG analysis, was then used to calculate the amount of C-S-H gel water in the sample. In the second method, data from multiple techniques including ignition test, MIP, TGA analysis, and careful weighing has been used. The detailed calculations for both methods have been provided in SI3 (VI).

Figure 3.6 gives an overview of the repartition of water obtained from both approaches normalized to 100 % of water in the sample. The amount of water present in the sample before and after homogeneous cavitation events (shown in blue), as obtained from the DVS sorption data is also provided in figure 3.6. This comparison indicates that after homogeneous cavitation the amount of water remaining in the sample is very close to the sum of chemically bound and interlayer water. Moreover, the difference in the water before and after the homogeneous cavitation corresponds to about 30% of total gel pores from the calcium balance approach and 26% of the total gel pores from other multiple techniques.
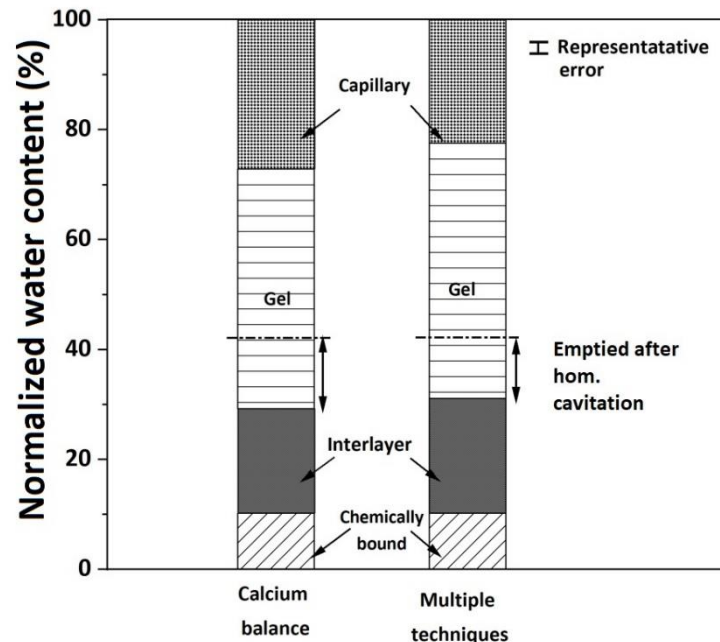
Figure 3.6: Water content overview of the control sample obtained using various methods. The double headed arrows indicate the amount of gel pores that were emptied after homogeneous cavitation.

Given that the pores emptied during the homogeneous cavitation step are isolated from the rest of the porosity, it is postulated that they may correspond to gel pores in the inner product.

The volume of the inner product of C-S-H was calculated according to the assumptions detailed in SI3 (VII). It was found that the inner product contains 34% of all gel water. This is in very good agreement (considering the errors and estimates) with 26% from multiple techniques and 30% from the calcium balance approach. Hence, gel pores that were considered isolated from the capillary porosity and in which homogeneous cavitation is supposed to occur, could be inside the inner product of the C-S-H and can only be accessed through the interlayer.

3.4.5   Proposed mechanism for homogeneous cavitation in hardened cement pastes

The proposed mechanism for homogeneous cavitation events is shown in figure 3.7: (i) C-S-H is saturated and the black arrows represent the drying front; (ii) as p_v/p_{sat} reduces, drying occurs by receding menisci in the gel pores that have access to the drying front; (iii) p_v/p_{sat} reduces to 0.3 and the tensile stress in the metastable pore liquid reaches ~ 150 MPa. However, the menisci cannot recede any further owing to the small radius of the interlayer spaces facing the drying front. Nevertheless, the liquid in the interlayer spaces and the liquid in the isolated gel pores still experiences high tensile stress owing to low p_v/p_{sat} . This stress would lead to homogeneous nucleation of a bubble in the gel pores, which would grow because of the tensile pull. Once the size of the bubble is greater than the critical radius (SI3 (II), equation 3(iv)), it results in cavitation. Figure 3.7 (iv) corresponds to the domain where cavitation events have occurred and the water in the isolated gel pores has changed into water vapour.

Homogeneous cavitation events as presented in Figure 3.7 are proposed to occur in the gel porosity of the inner C-S-H products, which are considered to be further away from the drying front than the C-S-H outer product. The homogeneous cavitation events would stop only if the bubble nucleation and growth ceases, moisture transport stops, or capillary pressure is lowered. Hence, this would explain

the long equilibration time observed in the desorption isotherm for the steps around p_v/p_{sat} = 0.3, at which evaporation induced cavitation takes place (see SI3 (VIII) for analogies with nanofluidic devices).
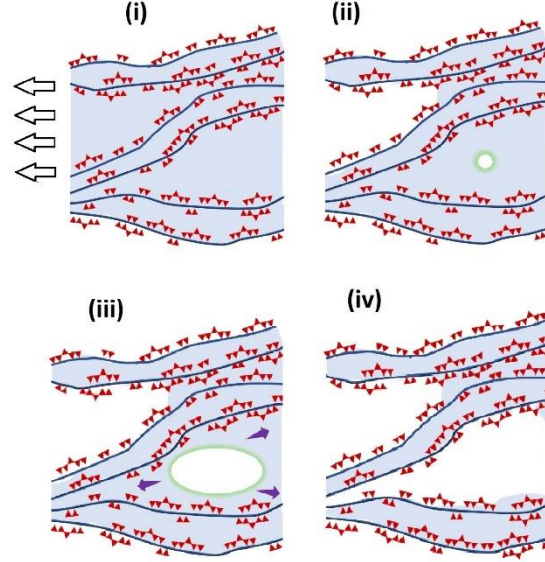
Figure 3.7:   Proposed homogeneous cavitation event in C-S-H(black arrows representing the drying front) (i) saturated C-S-H; (ii) drying occurs first in gel pores pores and in pores connected to the gel pores by receding meniscus; (iii) bubble expansion in the isolated gel pore because of induced tensile pull upon reaching p_v/p_{sat} = 0.3; (iv) drying by cavitation has occurred.

3.5   Conclusions

In this chapter, we examine the role of cavitation in drying cementitious materials using the classical nucleation theory (CNT). The presence of pre-existing bubbles and surface imperfections first promote heterogeneous cavitation around 0.8 p_v/p_{sat}. Thereafter, the connected porosity is progressively emptied. At about 0.3 p_v/p_{sat} a homogeneous cavitation event occurs which must be confined to pores isolated from the rest of the porosity. The volume balance analysis indicates that homogeneous cavitation happens in the gel pores of the inner product. As predicted by CNT, reducing the surface tension at the liquid-vapour interface by

introducing SRA and increasing sorption temperature reduce the homogeneous cavitation stress. Further, it was observed that cavitation results in a higher moisture loss and longer overall equilibration time. The results presented in this study also suggests that it is crucial to consider the anomalies of water for investigating the microstructure of cementitious materials using desorption isotherm.

Acknowledgements

Supporting information

SI3 (I) Phase diagram of water
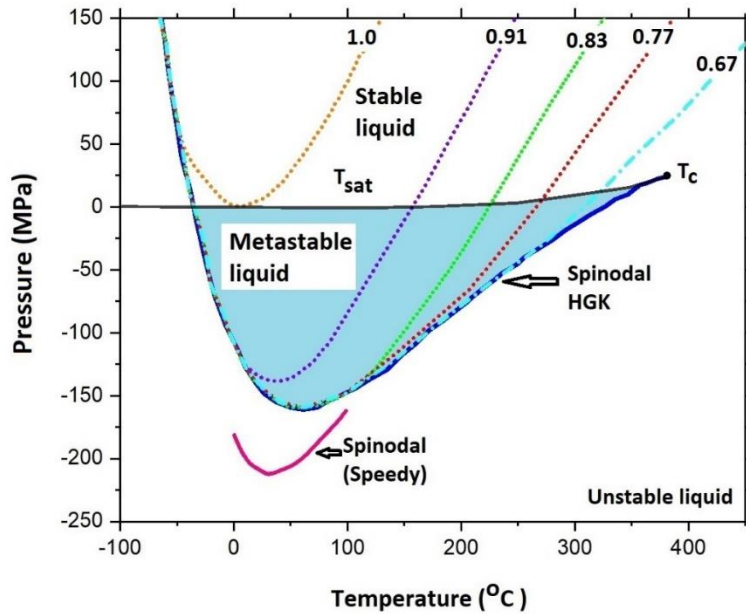
Figure 3-A1: Phase diagram of water based on the extrapolation of HGK equation of state of water and Speedy's equation (corresponding to spinodal decompositionof water) for different densities of water (g/ml) as indicated by the dotted lines. Reproduced with permissions [67].

Figure 3-A1 shows the phase diagram of water. The presented isochores are acquired by extrapolation of the HGK (Haar-Gallagher-Kerr H-G-K) equation below the equilibrium vapour pressure line[67] as a function of the density of water. The H-G-K equation itself is based on high precision experimental data collected in the positive pressures regime[80]. As shown in figure 3-A1, if the tensile stress on the liquid is increased, intermolecular forces dominate over short-range repulsion forces and the liquid attains a state of metastability. This metastability is ended by the homogeneous nucleation process. The spinodal of HGK equation has been

determined by the simpler Speedy's equation which in itself is based on the extrapolations obtained from the series of expansion of the liquid volume in the temperature range of 0 to 190°C. The spinodal decomposition of water is feasible in the unstable region of the phase diagram of water and occurs without the nucleation barrier. Further, much larger values for the tensile strength has been predicted for the spinodal decomposition using Speedy's equation as compared to the homogeneous cavitation. In the practical systems, the homgeneous cavitation would always occur and the spinodal decomposition cannot be observed experimentally. It is also important to emphasize again that the density of water in the pore also influences the cavitation pressure. As the density of water in confinement is different from the bulk and varies from one sample to the other, the tensile stress sustained before cavitation can also vary up to a certain extent. Additionally, using Tolman type corrections on the magnitude of surface tension can also result in lowering the overall magnitude of tensile stress.

SI3 (II) Expressions from CNT for homogeneous cavitation

The rate of homogenous nucleation of vapour bubbles E_b [81–83] is given by:

$$E_b = \frac{N_A kT}{v_m h} \exp\left[-\left(Q + \frac{16\pi\sigma_{lv}^3}{3(P)^2}\right)/kT\right] \tag{3-i}$$

N_A: Avogadro's constant (6.023×10^{23})

v_m: molar volume of water (1.805×10^{-5} m³/mol)

k: Boltzmann constant

h: Planck's constant

Q: activation energy required for molecular transport across the liquid-vapour interface.

For a measurable nucleation rate E_b of 1 cm⁻³s⁻¹, the cavitation stress could be approximated by[83]:

$$P^0 \approx \sqrt{\frac{16\pi\sigma_{lv}^3}{3kT \ln(\frac{N_A kT}{v_m h})}} \tag{3-ii}$$

Additionally, for a bubble of radius r, the energy cost of bubble creation W_{homo} can be represented by equation (3-iii)[84] :

$$W_{homo} = \frac{4}{3}\pi r^3 \Delta g_v + 4\pi r^2 \sigma_{lv} \qquad \text{(3-iii)}$$

Δg_v: Difference in free energy per unit volume between the thermodynamic phase nucleation is occurring in and the phase that is nucleating and can be considered equal to P as $P \gg p_{sat}$.

The energy cost is maximized at r^* [85], such that

$$r^* = 2\sigma_{lv} / \frac{RT}{\rho_l} \ln\left(\frac{p_v}{p_{sat}}\right) \qquad \text{(3-iv)}$$

Therefore, at a given p_v/p_{sat}, the probability of formation of bubble nucleus of size r^* is minimum. This energy cost would decrease again as the radius of the bubble would start to increase with respect to r^*.

Further, CNT assumes that the decay of the metastable liquid under tension proceeds through the formation of small vapour bubbles, whose formation is initially opposed by a free energy barrier. The energy barrier corresponding to the nucleation of a spherical vapour bubble of radius r, is given by[86]:

$$\Delta G^* = (16\pi \sigma_{lv}{}^3)/3(P)^2 \qquad \text{(3-v)}$$

Equations 3- (i), (iii), and (v) indicate that as σ_{lv} is decreased at a fixed temperature, the cavitation stress P^0, the energy cost of bubble creation W_{homo}, and the energy barrier ΔG^* all decrease. Therefore, modifying the liquid surface tension should modify the cavitation pressure.

SI3 (III) Heterogeneous cavitation

Heterogeneous nucleation is dependent on the surface chemistry of the system, and bubble nucleates on the pore wall or other available nucleation site. This makes the nucleation barrier or work for heterogeneous cavitation lower compared to homogeneous cavitation where a nucleation site is absent. Additionally, the work of heterogeneous nucleation is determined by the differences

in the surface areas ΔS and volumes of the unstable and stable bubbles ΔV and is given as[87].

$$W_{hetro} = \sigma_{lv}(\Delta S) - \frac{2\sigma_{lv}}{r}(\Delta V)$$ (3-vi)

Comparing the work for homogeneous nucleation as given by equation (3-iii) and equation (3-vi), it can be concluded that $W_{hetro} < W_{homo}$.

SI3 (IV) Kelvin and Young-Laplace equations

The Kelvin and Young-Laplace equations are used to calculate the pore capillary pressure as a function of p_v/p_{sat}.

Upon exposing the sample to sub-saturated vapour ($p_v/p_{sat} < 1$), the curvature of the menisci increases, and tensile stress is induced in the pore liquid. Thermodynamic equilibrium is achieved if the chemical potential of water in the pores is equal to that of the imposed vapour. If vapour is an ideal gas and the liquid is incompressible, the relation between pore pressure and imposed vapour pressure is given by the Kelvin equation as:

$$P = p_{sat} + \frac{RT}{v_m}\ln\left(\frac{p_v}{p_{sat}}\right)$$ (3-vii)

P : pore capillary pressure

R : Universal gas constant (8.314 J/K)

T: Temperature (in Kelvin)

Further, from the Young–Laplace equation,

$$P - p_v = -\frac{2\sigma_{lv}\cos\theta_r}{r_k}$$ (3-viii)

σ_{lv} : surface tension at the liquid-vapour interface,

θ_r : contact angle of the meniscus in a pore of radius r_k.

The original Young-Laplace equation (equation 3-vii) does not consider any fluid-wall interactions. Therefore, to account for these interactions the statistical thickness of the adsorbed layer before evaporation t_c is added to the core radius r_k. The corrected pore radius r_P for a cylindrical pore is given by:

$$r_P = r_k + t_c \qquad\qquad (3\text{-ix})$$

SI3 (V) The Barret-Joyner-Halenda (BJH) method

The BJH method was initially proposed to determine the pore size distribution in the mesopore range (pore size between 2 and 30 nm, according to IUPAC classification) and in the micropore range (<2 nm) from gas desorption isotherms[88]. This method is also used extensively to obtain pores size distribution from moisture sorption isotherms of cementitious materials [12,56,57]. This method is based on the modified Kelvin equation which can be determined using equation (3-vii), (3-viii), and (3-ix). Considering that pore pressure P is much larger in magnitude ($\approx$ MPa) than p_v and p_{sat} ($\approx$ KPa) the modified Kelvin-Laplace equation is given as:

$$r_P = -\frac{2\sigma_{lv}cos\theta_r}{\frac{RT}{v_m}\ln\left(\frac{p_v}{p_{sat}}\right)} + t_c \qquad\qquad (3\text{-x})$$

The statistical thickness t_c of the adsorbed layer as a function of p_v/p_{sat} can be obtained by several empirical and theoretical methods which include Halsey's equation, Hagymassy t-curve, Badmann equation, and Brunauer- Emmett-Teller (BET) surface area among others[89,90]. For this study, t_c has been calculated using Brunauer- Emmett-Teller (BET) equation and the detailed calculations have been provided in the following section.

Calculation of statistical thickness t_c

The 0.05 to 0.35 p_v/p_{sat} range of the absorption isotherm has been used for the calculation of BET surface area. The BET equation is given by:

$$\frac{1}{w[(p_{sat}/p_v)-1]} = \frac{c-1}{w_m}\left(\frac{p_v}{p_{sat}}\right) + \frac{1}{w_m c}$$
(3-xi)

w: weight of the adsorbed sample at a given p_{sat}/p_v

w_m: monolayer of water

c: BET constant

On plotting the term $\frac{1}{w[(p_{sat}/p_v)-1]}$ on y-axis and $\frac{p_v}{p_{sat}}$ on x-axis and considering the linear plot between 0.05 and 0.35 p_v/p_{sat}, it is possible to obtain the BET surface area A_{BET} by following set of equations:

$$w_m = \frac{1}{M+I}; c = \frac{M}{I}$$
(3-xii)

M: slope of the linear plot

I: intercept of the linear plot

$$A_{BET} = \frac{\sigma_w N_A w_m}{m_s}$$
(3-xiii)

σ_w: water adsorption cross-sectional area (1.14×10^{-19} m^2)

m_s: is the mass of dry cement sample

Statistical thickness has been then calculated by using the following expression:

$$t_c = w/(A_{BET} * \rho_w)$$
(3-xiv)

ρ_w: density of water

The BJH method considers the desorption isotherm as a series of steps and divides the pore sizes into groups such that all the pores in each group have an average radius r_P. As the pressure is reduced, the amount of adsorbate is removed from the inner core of the pore (r_k) and the thickness of the adsorbed film is

reduced (Δt_c). Further decrease in pressure not only removes adsorbate from the core of second group of pore sizes but also decreases the thickness of adsorbed layer of the first group of pores. For each group, the pore core radius r_k and the change in the thickness is calculated as p_v/p_{sat} is lowered. The total pore volume and the surface area of the pores are obtained by adding the values in each group of pores.

Moreover, for this analysis the modified values of σ_{lv} were used for the sample measured at higher sorption temperature and for the samples prepared with SRA. For the control sample measured at 50 °C, σ_{lv} was determined by using the following equation, as given by the International Association for the Properties of Water and Steam[91]:

$$\sigma_{lv} = 235.8 \left[\frac{647.15 - T}{647.15}\right]^{1.256} \left[1 - 0 \cdot 625 \left(\frac{647.15 - T}{647.17}\right)\right] \qquad \text{(3-xiv)}$$

Hence, at 50 ° C σ_{lv}= 67.97 mN.m^{-1}. For samples prepared with 2% and 3% SRA, reduced values of surface tension were used following the experimental results in previous studies[92][93]. The considered values for σ_{lv} for all samples are shown in the table 3-A1. The table also gives the values for the BET surface area used for the calculation of t_c and the corresponding position of the sharp peak in BJH pore size distribution for all the samples.

Table 3-A1: Values for surface tension, BET surface area, and position of the sharp peak in the BJH pore size distribution for various samples considered in this study.

Sample	Surface tension (mN.m^{-1})	BET surface area (m^2.g^{-1})	Position of the sharp peak (nm)
Control sample	72.86	185.5	1.1
Control sample (50°C)	67.97	160.6	2
Sample 2 % SRA	65	187.4	1.9
Sample 3 % SRA	57	190.0	2.2

SI3 (VI) Water content distribution

- **Calcium balance approach**

The following table 3-A2 gives the initial and final amount of calcium that was used to calculate the water content distribution in C-S-H.

Table 3-A2: The values for the initial and final calcium content in the control sample cured at 55 °C for 90 days. The values are provided in grams and have been normalized per 100 g of cement paste.

Phase	Initial Content	Final content
C3S	17.41	1.78
C2S	6.65	1.89
From other phases (CH+C_3A+HH)	3.05	
Portlandite		4.39
Ettringite		0.89

- **Multiple techniques approach**

In this approach, at first an ignition test was used to determine the effective w/b ratio. As the samples were cured under water, a higher w/b ratio of 0.78 (initially 0.7 during mixing) was found after igniting the sample to 1050 °C and accounting for the loss of carbonates and the loss on ignition (LOI) from XRF analysis. Samples were weighed before (saturated state) and after the solvent exchange drying method. Based on the average results of 10 samples (~0.5 g each), the weight loss due to solvent exchange was found to be 25.3 g/100 g paste. This weight loss was assumed to be equal to the sum of water in capillary pores, voids, and 75% of the C-S-H gel water, as reported in [75]. The amount of water remaining in the C-S-H after solvent exchange drying was calculated following the approach mentioned in [94] using TGA analysis.

SI (VII) Calculation of inner and outer products of C-S-H

The following approach has been used to evaluate the volume of the inner and the outer product. Firstly, the density of the saturated cement was calculated by weighing 10 slices of saturated cement paste of average diameter 32.82 mm and thickness 1.82 mm. This density was found to be 1.6 g/cm³ which was used for calculating the total volume of the sample.

The volume of the inner product of C-S-H was calculated assuming that it forms exclusively in the spaces left by the dissolving cement grains[95]. Considering the formation of hollow shells, the maximum volume of the inner C-S-H product should be equal to the volume of reacted alite and belite. Using the reacted mass of alite and belite from XRD Rietveld refinement (Table 3.1) and their densities as mentioned in the table 3-A3 [69], the volume of reacted alite and belite was calculated to be 10.57 and 3.97 cm³/ 100 g of paste, respectively.

Table 3-A3 – Density and volume of different components in the control sample. Volumes were normalised per 100g of hydrated saturated paste.

Name		Density (g/cm³)	Volume cm³
Total volume of 100 g paste		1.6	62.5
Inner product (reacted clinker phases)	Alite	3.15	9.57
	Belite	2.99	3.97
Ettringite		1.78	2.02
Portlandite		2.26	3.58
Interhydrate, capillary, voids		1	14.6
Unreacted clinker	Alite	3.15	1.08
	Belite	2.99	1.44
Outer product		-	25.21

The volume of ettringite could be calculated in a similar manner using the mass of ettringite obtained from XRD Rietveld refinement and the theoretical density of ettringite. The volume of portlandite was calculated using the mass obtained by TGA analysis. The volume of the outer product of C-S-H was calculated by subtracting the volume of inner product, unreacted clinker phases, ettringite, portlandite, and capillary water from the total volume of saturated hardened cement paste. Assuming that the amount of interlayer water and gel water is the

same between the outer and the inner C-S-H, it was found that the inner product contains 34% of all gel water.

Another approach to quantify the volume of saturated C-S-H is by assuming its bulk density. Based on the extensive work of Gajewicz *et al.* and Müller *et al.*, it has been assumed to be 1.94 g/cm^3[32,62]. Further, the number of moles in bulk C-S-H can be determined by matching the water content found in the calcium balance approach to be 5.1. The volume of C-S-H in 100 g cement paste was found to be 36.65 g/cm^3, which is very close to the 38.75 g/cm^3 value determined by the previous approach that also includes the volume of hollow shells.

SI3 (VIII) Results of cavitation in this study vs. direct observations of cavitation in nanofluidic devices

Some relevant results from direct observations of cavitation events in transparent nanofluidic devices can provide some insight that could be helpful in understanding the high moisture loss and equilibration time observed in this study.

Duan *et al.* fabricated silica nanochannels with varying height from 20-120 nm and observed the role of cavitation in the drying of the nanochannels[63]. The authors also observed faster drying or evaporation rate that was an order of magnitude higher than what is obtained by receding meniscus. This observation is comparable to the results presented in this study where high moisture loss was associated with cavitation events. The evaporation induced cavitation was found to be aided by advective liquid transport and the bubbles showed unusual motion as well as transitional stability, which was attributed to the balance between two competing mass fluxes driven by thermocapillarity and evaporation.

Vincent *et al.* experimentally investigated a synthetic sample with extreme ink-bottle geometry that had nanometer-sized necks connecting to micrometre-sized voids. The drying dynamics were analysed by time-lapse photography. The drying stress was noted to be in the range of 24-30 MPa. Further, the deterministic mass transport and the stochastic events were suggested to govern heterogeneous cavitation[96]. The authors also observed that the cavitation events were interspersed and distributed over the entire timespan until all the voids were empty.

These observations can also explain why cavitation would take longer equilibration times than usual drying by receding meniscus the porous media with interconnected pores.

Chapter 4 The effect of hydration temperature on the microstructure of calcium-silicate-hydrates

Monisha Rastogi[ab], Mohsen Ben Haha[a], Karen L. Scrivener[b]

[a]HeidelbergCement Technology Center, Leimen, Germany

[b]École polytechnique fédérale de Lausanne, Switzerland

Note: This chapter is a "manuscript in preparation" that is planned to be submitted as a research article.

Contribution of the doctoral candidate: Writing of the first manuscript draft, experimental design, Carrying out the experiments presented in the manuscript, editing and compilation of input from the other authors.

Abstract

This study aims to identify the role of hydration temperature on the microstructure of the samples with maximized calcium-silicate-hydrate (C-S-H) content. Several techniques including X-ray diffraction, scanning electron microscopy, and ^{1}H nuclear magnetic resonance relaxometry have been used to calculate the water content distributions and the pore volumes of the samples cured at 5, 20, 40, and 55°C. The moisture desorption isotherms of the 'as-prepared' samples, acquired using dynamic vapour sorption technique were also analysed to determine the water content distributions and pore volumes. Finally, a comparison of accessible porosity between mercury intrusion porosimetry and moisture desorption analysis is presented.

Keywords: C-S-H, curing temperature, dynamic vapour sorption, pore volumes.

4.1   Introduction

Hydration or curing temperature plays an important role in the properties of cementitious materials. For instance, it has been reported that at higher temperatures, the porosity is coarsened and AFm phases (calcium monosulphoaluminate) are more stable as compared to ettringite [62,97–100].

The main binding phase of hydrated cement paste, C-S-H, has been reported to be particularly sensitive to the curing temperature. Richardson reported that elevated temperatures result in fine texture morphology, increase in polymerization, and a decrease in Ca/Si ratio as compared to the pastes cured at ambient temperatures [101]. Gallucci *et al.* studied dried cement pastes that were cured within the range of 5 to 60 ℃ using scanning electron microscopy (SEM) and X-ray diffraction (XRD). A 25% increase in the apparent (bulk/with gel water content) density of C-S-H was observed. However, Ca/Si ratio did not vary significantly[94]. Bahafid *et al.* used multiple experimental techniques including XRD, mercury intrusion porosimetry (MIP), and thermogravimetric analysis (TGA) to study the effect of hydration temperature on the microstructure of class G oil-well cement, in the range of 7 to 90 °C [57]. It was reported that the bulk density of C-S-H increased from 1.88 g/cm^3 (7 °C) to 2.10 g/cm^3 (90 °C). However, this increase was not as significant as that reported by Gallucci et al. Similarly, Gajewicz *et al.* used ^{1}H NMR relaxometry to report the results on cement pastes that were cured at temperatures in the range of 10 to 60 ℃ [62]. The C-S-H bulk density results were found to be in accordance with results reported by Bahafid *et al.* Recently, Avet *et al.* studied the change in water content of calcium-aluminate-silicate-hydrate (C-A-S-H) of plain cement and Limestone Calcined Clay Cement (LC^3) using TGA, ^{1}H NMR, and SEM. The H$_2$O/(Si+Al) ratios and bulk densities for the plain cement pastes cured at 20℃ were in good agreement with those reported by Gajewicz *et al.* Furthermore, the results from Gallucci *et al.* were also corrected by normalizing the water content to water-saturated cement in this study.

In the present study, several techniques have been used to investigate the role of hydration temperature on the samples with maximized C-S-H content. Initially, SEM-EDX, XRD Rietveld refinement, TGA, and ^{1}H NMR relaxometry were used to determine the water content distribution and pore volumes in the samples

by mass/volume balance calculations. Thereafter, the desorption isotherms were acquired on the 'as-prepared' samples using dynamic vapour sorption (DVS) technique. This data was used to estimate the amount of gel and capillary water and their respective pore volumes. These pore volumes were compared with those obtained using mass/volume balance calculations. Additionally, the porosity of the samples was also measured by MIP and a comparative overview of accessible porosity has been presented.

4.2 Materials and methods

In this study, samples were prepared in which the content of C-S-H is maximized by the procedure as described in chapter 3. The amount of hemihydrate was decided based on the heat release by hydration of cement using isothermal calorimetry, such that the aluminate peak could be distinguished from the silicate peak (see supplementary information S4.1 for details). The following cement paste composition was finally selected: ground white-cement clinker 84.5% by wt.; hemihydrate (HH) 5.5% by wt., and silica fume (SF) 10% by wt. This binder was mixed with water at a water-to-binder (w/b) ratio of 0.7 using a high-speed mechanical mixer (Ultraturrax) at 24000 rpm for 90 s followed by 30 s of lowering the speed (24000-0 rpm). The samples were cured at 5, 20, 40, and 55 ℃ under distilled water for 90 days prior to the measurements. The effective w/b ratio of the samples, found to be around 0.78(± 0.1), has been determined using the ignition test accounting for loss on ignition by following a previously reported procedure [102].

For XRD analysis and Rietveld refinement, thin slices (3 mm thick) were cut from the sealed cylinders of the as-prepared samples. Bruker D8 Advance diffractometer with monochromatic Cu-Kα radiation (λ = 1.541 Å) and a step-size of approximately 0.02° was used to acquire data in the range of 5° to 70° (2θ). The degree of hydration of clinker phases was calculated by Rietveld refinement using Topas software, with quartz as the external standard and following a previously reported procedure[69].

Samples were dried by solvent exchnage method for the microstructural characterizations such as TGA, SEM, and MIP. The solvent exchange method was

selected owing to its least invasive nature[70–72]. The samples were crushed with a mortar and pestle and around 30(± 2) mg of the resulting powder was used for TGA (Netzsch STA 449 F3 ''Jupiter''; 20 to 700 °C) under a nitrogen atmosphere with a heating rate of 10 °C/min. The portlandite content was calculated from the TGA analysis using the tangent method.

For SEM analysis, the dried samples were impregnated with epoxy resin in a mould under vacuum. Thereafter, the samples were polished down to 1 µm using diamond sprays and a petrol-based lubricant. A FEI Quanta 200 microscope coupled with a Bruker XFlash 4030 Energy dispersive X-ray spectroscopy (EDS) detector was used to acquire the SEM images and the EDS analysis.Solvent exchanged samples were crushed into 1-2 mm pieces for MIP analysis (Pascal 140/440 Porosimeter, Thermo Scientific). The maximum applied pressure was 400 MPa. The surface tension of the mercury was considered as 0.48 N/m for the analysis. Two repetitions were done on each sample to ensure reproducibility.

^{1}H NMR Carr–Purcell–Meiboom–Gill (CPMG) measurements were made on undried samples for analysis of the state of water in them. The crushed sample was equilibrated at 0.95 p_v/p_{sat} for 6 months. The experiments, with 256 echoes logarithmically spaced between 60 µs and 0.5 s, were made on a benchtop magnet operating at 20 MHz by using Kea^2 spectrometer (Magritek, New Zealand). The 90° excitation pulse length was 6 µs and the spectrometer dead time was 10 µs. Eight points per echo were acquired with a dwell time of 1 µs. The experimental repetition time (τ_{rd}) was 1 s and the number of scans was 1024.

The water vapour desorption isotherms were acquired using DVS Adventure (Surface Measurement Systems) on 'as-prepared' saturated samples. The sorption temperature was 20 °C for all samples. Samples weighing ~25 mg were crushed and subjected to desorption with the starting point at 0.98 p_v/p_{sat} followed by data acquisition from 0.98 p_v/p_{sat} to 0.03 p_v/p_{sat} with a step size of 0.05. Initial mass from the balance (once the balance was considered stable) was also recorded and considered to be nearly equal to the mass of the saturated sample m_s at $p_v/p_{sat} \approx$ 1. The mass equilibrium was identified as the point at which the mass change was less than 10^{-4} mg/min or exceeding the assigned time limit which was 1440 min for 0.98 and 0.03 p_v/p_{sat} and 720 min for all other steps. If the equilibrium was not

attained in the given time interval, the moisture content was extrapolated by using the asymptotic function for moisture ratio MR:

$$MR = \frac{m_t - m_0}{m_{eq} - m_0} = 1 - \exp(-k_m t) \qquad (4.1)$$

m_t : mass at time t

m_0: mass at time 0

m_{eq}: Equilibrium mass at a given p_v/p_{sat}

k_m: fitting parameter

This equation has been previously used in several investigations on moisture sorption and is based on the analytical solution of the diffusion equation[39,58,73,74]. The data is normalized to per gram of dry cement paste.

4.3 Results and discussions

4.3.1 SEM- EDS

Figure 4.1(a) and (b) show the SEM micrographs for the samples cured for 90 days at 20 and 55℃, respectively. No significant difference was observed in the microstructures of the samples under consideration. SEM-EDS analysis was used to determine the atomic composition of C-S-H. The Ca/Si ratio was determined using at least 200 independent EDS spots. As reported by Rossen *et al.*[103], the extreme Si-edge has been considered for the determination of Ca/Si ratio of the C-S-H. The Ca/Si
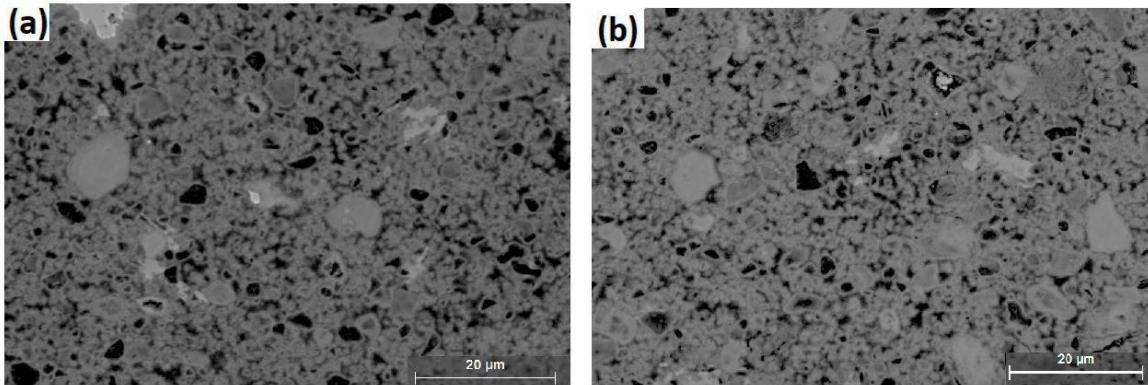
Figure 4.1: SEM micrographs for the samples cured at (a) 20 and (b) 55 ℃.

ratio was found to be in the range of 1.5-1.45 (± 0.01). This ratio did not vary significantly with an increase in the curing temperature (5 to 55 °C). Similar observations were made by Lothenbach *et al.* who also used SEM-EDS analysis to determine the Ca/Si ratio for sealed Portland-limestone cement paste. Ca/Si was found to be in the range of 1.62 to 1.72 for samples cured between 5 and 40 °C[97]. Using ^{1}H NMR relaxometry, Gajewicz *et al.* also determined the Ca/Si ratio for samples cured in the range of 10 to 60 °C and reported no significant variation in the average Ca/Si value (1.67)[62]. The relatively lower Ca/Si ratio found in this study can be attributed to the presence of the silica fume along with the high water to binder ratio as previously reported[19,58,104].

4.3.2 ^{1}H NMR relaxometry
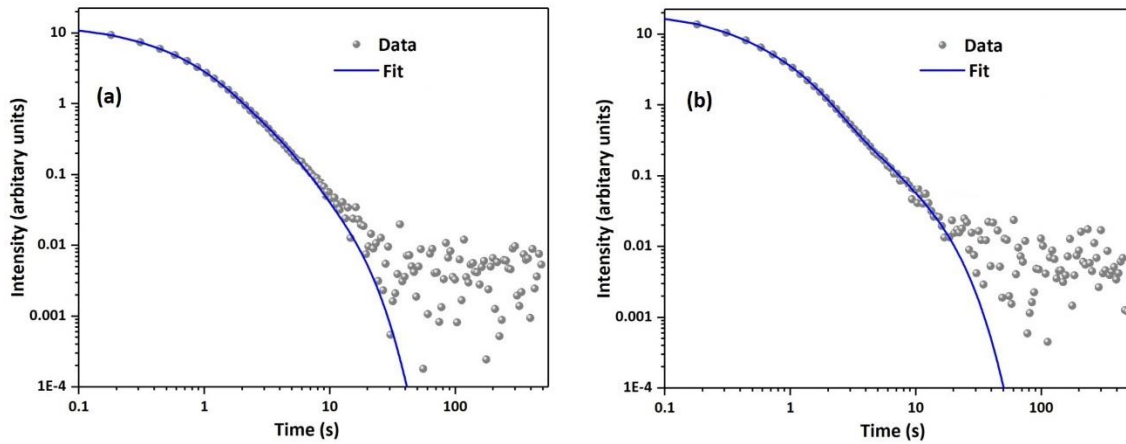
Figure 4.2 CPMG decay data as obtained from ^{1}H NMR relaxometry and the corresponding multi-exponential fit for the samples cured at (a) 20 °C and (b) 55 °C. A small baseline signal (equal to the standard deviation of the noise and resultant from analysis of magnitude data) has been subtracted.

Multi-exponential fitting was applied to analyze the ^{1}H NMR (CPMG) data obtained for the samples cured at 5, 20, and 55 °C. Figure 4.2(a) and (b) shows the multi-exponential fit for samples cured at 20 and 55 °C, respectively. As the capillary pores were partly empty owing to equilibration at 0.95 p_v/p_{sat}, only the signals from gel pores and interlayer spaces were considered in this analysis. The ratio of the relaxation times was fixed such that T_2 value of gel pore water was equal to 3 times

the T_2 value of interlayer water, as observed in earlier studies[62,75]. The shortest time and the different amplitudes were allowed to vary, as previously reported[76,77]. T_2 values of around 0.2 and 0.6 ms were attributed to the interlayer and gel pore water of the C-S-H, respectively. The gel to interlayer ratios were found to be in the range of 2.1-2.25, which are in good agreement with several other studies for mature white cement pastes[59][32].

4.3.3   Water content distribution and mass/volume balance calculations

The following sections discuss the methods that are used to determine the water content distribution, phase assemblage, and the resulting mass and volume compositions as a function of the hydration temperature.

4.3.3.1   Water content distribution

Water content or the pore solution filled spaces can be divided into four categories according to ^{1}H NMR relaxometry based on their characteristic size[105]. Briefly, water can exist in interlayer spaces (≈1 nm), gel pores (≈2-8 nm), interhydrate pores (≈ 8-10 nm), and capillary pores (≈ 8-10 nm).

To determine the amount of water in C-S-H (gel and interlayer), the calcium balance approach was used. The mass of calcium within the C-S-H was calculated by subtracting the calcium present in ettringite and portlandite from the calcium provided by the reacted clinker phases (more details in supplementary information S4.2). Briefly, a H_2O/Ca ratio of 0.482 was used to calculate the amount of water present in the C-S-H interlayer for all samples, as this ratio does not vary significantly as a function of curing temperature[59]. The gel/interlayer ratios, as measured using ^{1}H NMR CPMG analysis, were used to calculate the amount of C-S-H gel water. The only exception was the sample cured at 40 °C on which the ^{1}H NMR analysis was not carried out. The ratio for this sample was assumed to be the same as that determined for the sample cured at 55 ℃. The bound water contents were determined using the amount of portlandite and ettringite from the TGA and XRD Rietveld refinement, respectively. The remaining water that should be present in the bigger pores (interhydrate and capillary pores) has been determined by subtracting

the water in C-S-H and the bound water from the total water content. Figure 4.3 shows the water content distribution (normalized to 100%) in the various samples considered in this study.
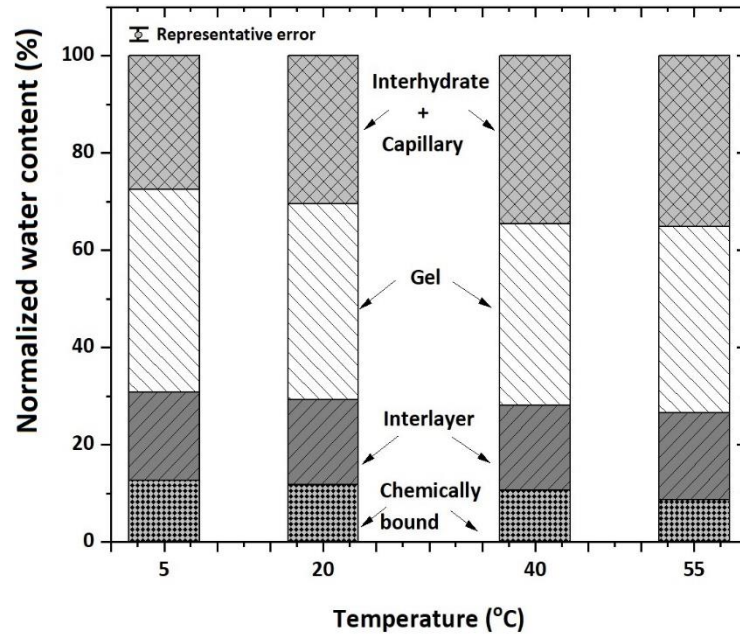
Figure 4.3: Water content distribution for the samples cured at 5, 20, 40, and 55 °C.

4.3.3.2 Mass and volume composition calculations

The mass and volume of unreacted cement, ettringite, and portlandite have been calculated using XRD Rietveld refinement. The content of portlandite has been additionally determined using TGA. For determining the mass and volume of C-S-H, it is crucial to determine the C-S-H composition. In particular, the number of moles of water per mole of C-S-H (n_{H_2O}) and the densities of solid and bulk C-S-H as a function of curing temperature are required. As reported in previous studies [62,105], the solid C-S-H corresponds to the Ca-O layers with SiO_2 tetrahedra and the water in between interlayer spaces. It does not include any water or ions on the outermost surfaces of C-S-H. The bulk C-S-H corresponds to the overall C-S-H phase that includes all the gel water.

- **Number of moles of water in solid and bulk C-S-H**

The n_{H_2O} in solid and bulk C-S-H were determined such that the gel and interlayer water content match the water content calculated using the calcium balance approach. It was found that n_{H_2O} in both solid and bulk C-S-H decreased from 2.10 to 1.67 and 5.8 to 5.1, respectively, as the temperature increased from 5 to 55 °C. Figure 4.4 shows the comparison between n_{H_2O} as determined in this study and that reported by Gajewicz et al. (for hydration temperatures ranging from 10 to 60 °C with w/b=0.4 and cured underwater for 90 days)[77]. It can be observed that the solid water content calculated in this study is very close to the reported values. Nevertheless, a considerable difference was observed in the bulk water content. This can be explained by an increased volume of gel pores owing to a higher initial w/b ratio.

Müller et al. also reported n_{H_2O} in solid and bulk C-S-H for white cement pastes that were sealed cured at various w/b ratios of 0.32, 0.40, and 0.48 at 20 °C[59]. It is interesting that for the sample cured at 20 °C, the n_{H_2O} in solid and bulk C-S-H show a good resemblance to the values reported by Müller et al. for the sample with a w/b of 0.48. The data, normalized to per mole of C-S-H, is shown in
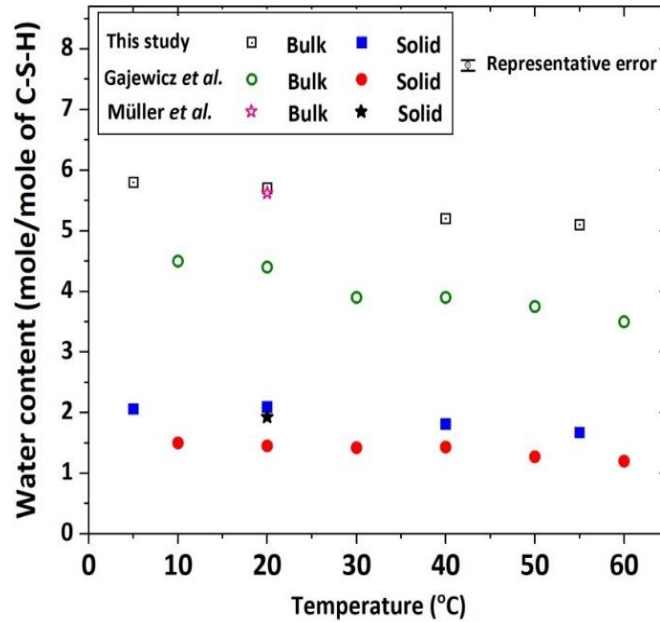
Figure 4.4: Comparison of the determined number of water moles per mole of C-S-H as a function of curing temperature [59][77].

figure 4.4.

- **<u>Solid and bulk density of C-S-H</u>**

In this study, the estimations of bulk and solid densities are based on extensive data reported by Müller *et al.* and Gajewicz *et al.* using ^{1}H NMR relaxometry on 'as-prepared' samples[59] [77].

Müller *et al.* reported the bulk and solid densities to be 1.86(±0.02) g/cm^3 and 2.75(±0.02) g/cm^3, respectively, for the sample sealed cured at 20 $^\circ$C for 28 days with a w/b ratio of 0.48. The bulk and solid densities are expected to increase slightly with the hydration time of 90 days. However, it is reasonable to assume that after a high w/b of 0.48, the gel volume would not increase (or the bulk density would not decrease) substantially and would reach a plateau. Therefore, for samples cured at 20 $^\circ$C, considering the similarity in n_{H_2O}, the bulk and solid densities have been assumed to be 1.86(±0.05) and 2.75(±0.05) g/cm^3, respectively.

Gajewicz *et al.* reported an increase of 0.11 g/cm^3 (4.25%) and 0.12 g/cm^3 (5.7%) in the solid and bulk densities, respectively, with an increase in temperature from 10 to 60 °C [77]. However, samples with curing temperatures at and above 30 °C showed a very minor difference in the solid and bulk C-S-H densities. Following that a change in curing temperature from 20 to 10°C results in a 1.92% decrease in solid density, it has been assumed that the solid density upon temperature change from 20 to 5 °C would be 2.69 g/cm^3. Similarly, the solid densities for curing temperatures of 40 and 55°C have been assumed to be 2.76 and 2.77 g/cm^3 respectively (figure 4.5). The bulk densities of other samples have also been assumed in the similar manner and reported in figure 4.5. Figure 4.5 also shows densities reported by Gajewicz *et al.* on which these assumptions are made.
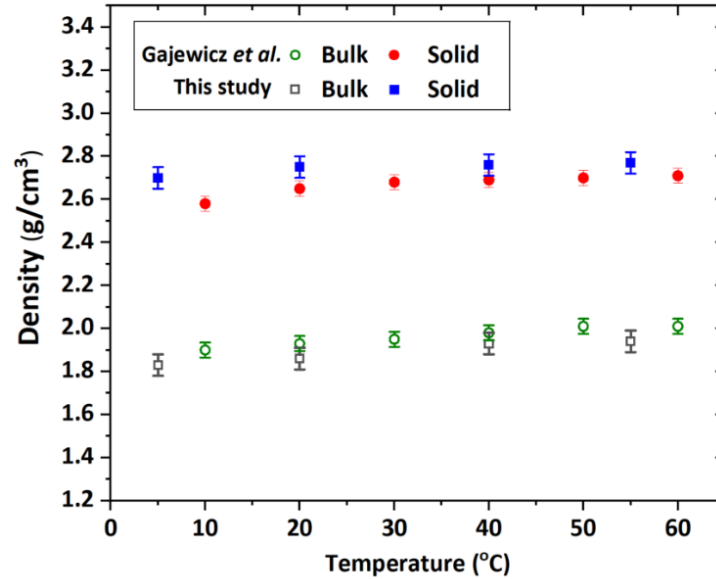
Figure 4.5: Comparison of assumed bulk and solid densities of C-S-H as a function of curing temperature. The graph also shows the data for solid and bulk densities determined by Gajewicz et al. using ^{1}H NMR relaxometry on which the assumptions for densities are based in this study[77].

Figure 4.6 shows the overall mass and volume composition of the samples cured underwater at various temperatures for 90 days. It is important to consider that chemical shrinkage induces volume reduction as the volume of hydration products is lower than the original volume of reactants. In the sealed cured samples it results in additional porosity which is termed as voids. If the pastes are cured underwater, the water is drawn into the samples that fill the voids, which in turn results in a higher final (or effective) w/b ratio (0.78±0.02) for samples considered in this study. Therefore, for samples cured underwater, the mass of paste increases whereas the total volume remains constant. Hence, the chemical shrinkage is only considered in volume calculations. Furthermore, due to the low mass (and subsequent volume) of unreacted silica fume, its amounts have been added to the amount of unreacted cement.

It can be observed that the pastes cured at higher temperatures are slightly more reacted. Further, with the increase in the curing temperature, the amount of ettringite was found to decrease, whereas the amount of portlandite was observed to be unaffected. The mass and volume of C-S-H increased with increasing temperature even though the gel water content decreased slightly. Additionally, the amount of capillary, interhydrate, and voids was observed to be higher for samples cured at higher temperatures. This is attributed to the higher coarse porosity. All these observations are in very good agreement with other studies[57,59,62].
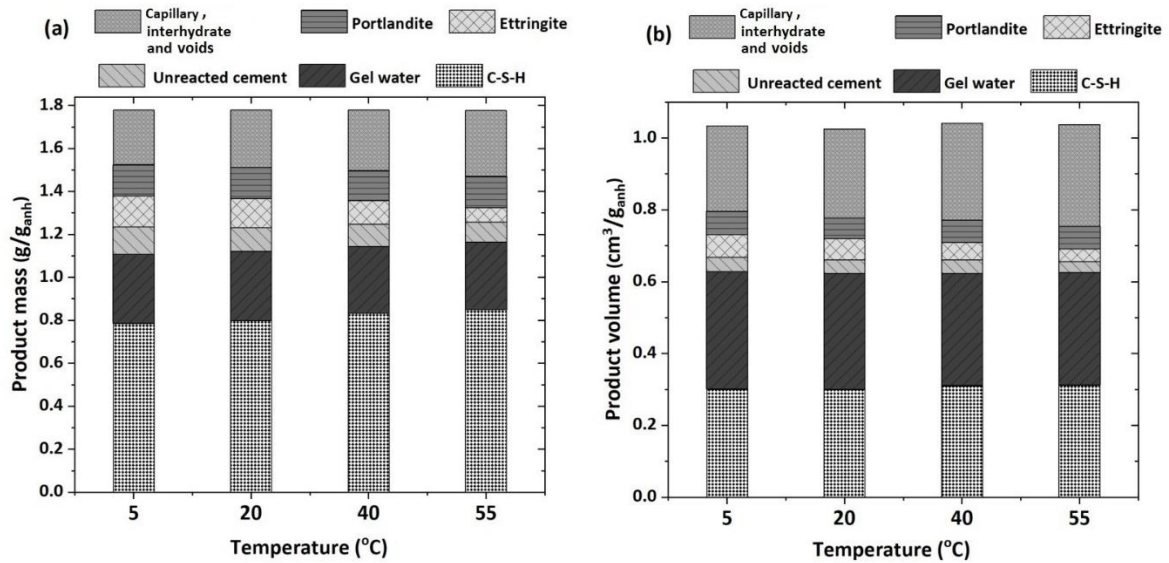
Figure 4.6 : (a) Mass and (b) volume compositions for 90 day-old cement pastes cured under water at various temperatures.

4.3.4 Dynamic vapour desorption analysis

Figure 4.7 shows the desorption isotherms for the considered samples. It is crucial to note that the highest p_v/p_{sat} attained by dynamic vapour sorption equipment, at which samples can be equilibrated reliably, lies between 0.97 to 0.96 as compared to the input value of 0.98 p_v/p_{sat}. This results in considerable variability in determining the extent of filled porosity. For instance, using the modified Kelvin-Laplace equation, all the pores smaller than 106.4 nm in diameter

would be filled at 0.98 p_v/p_{sat}. However, only pores smaller than 42.94 nm in diameter would be filled at 0.96 p_v/p_{sat}. Therefore, to have a uniform starting point
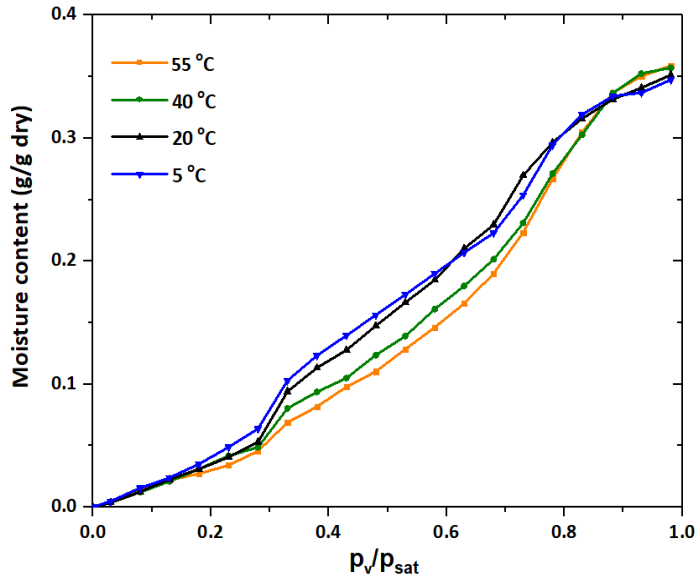
Figure 4.7: Desorption isotherms for the samples cured at 5, 20, 40, and 55°C

throughout the measurements in this study, the mass m_s (at ≈1 p_v/p_{sat}) corresponding to the mass at the start of the measurements has been considered equivalent to the mass of the saturated cement sample and used for further analysis.

It was shown in chapter 3 that the desorption isotherms are affected by heterogeneous and homogeneous cavitation. Further, it was also shown that all the capillary pores are emptied after heterogeneous cavitation (~0.83-0.78 p_v/p_{sat}, capillary pressure of 20-25 MPa, pore diameter around 18 nm-10nm). Therefore, the amount of capillary water can be obtained by subtracting the mass at 0.78 p_v/p_{sat} from the mass of saturated cement paste m_s. Figure 4.8 (a) compares the amount of capillary water calculated using desorption isotherms and the mass balance calculations. The relatively higher values from desorption isotherms can be attributed to the error in defining the starting mass. Another source of discrepancy between the capillary water content obtained from desorption isotherms arises from the nature of heterogeneous cavitation, in which the water loss from capillary pores would also be accompanied by a small amount of water loss from some gel pores/narrow necks. This would result in increasing the overall capillary water content from desorption isotherms. Nevertheless, in general, there is a good

agreement between the capillary water content obtained from the desorption isotherms and those obtained from mass/volume balance calculations. Additionally, the capillary water content determined using the mass range $m_{0.96} - m_{0.78}$ have also been presented.
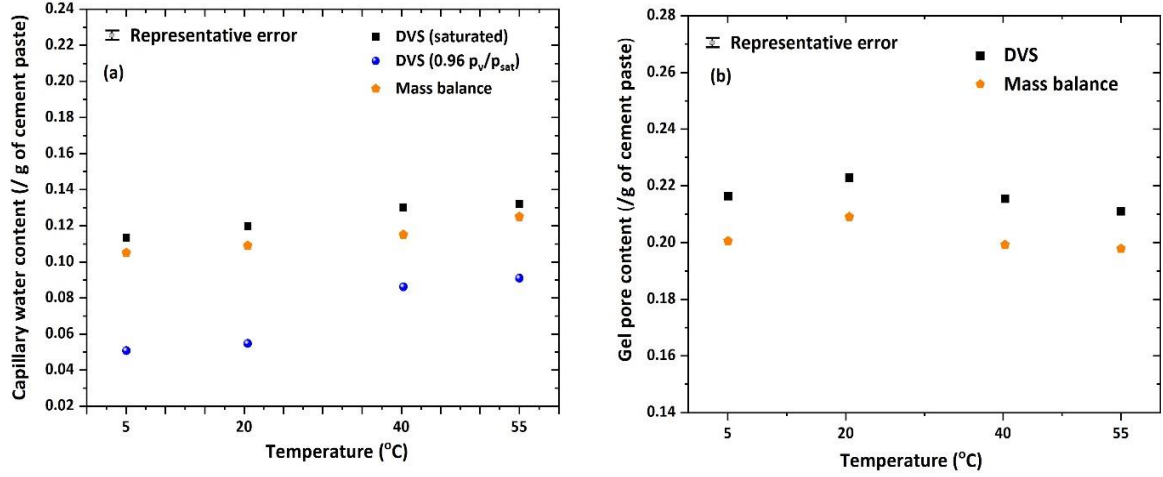
Figure 4.8: (a) Capillary water content obtained from mass balance and DVS. (b) Gel water content determined by mass balance calculations and compared with DVS gel volumes.

Furthermore, it was also shown in chapter 3 that all the gel pores are emptied once the homogenous cavitation events end at around 0.28 p_v/p_{sat}. Therefore, assuming that gel pores are emptied in the range of $m_{0.78} - m_{0.28}$, the gel pore content has been plotted in figure 4.8 (b). Figure 4.8 (b) also shows the gel volumes obtained from the mass/volume balance calculations. The slightly higher values can be explained by the nature of homogeneous cavitation, where emptying of gel pores would also be accompanied by some loss of water from the interlayer spaces. Further, comparing with the water content distribution, it was found that for the samples cured at 5, 20, 40, and 55 °C, the amount of gel pores emptied after homogeneous cavitation were 33%, 31%, 30%, and 26%, respectively.

4.3.5 MIP analysis

Figure 4.9 shows the MIP data for the samples considered in this study. The intruded volume and pore volumes (corresponding to the percentage of sample volume) have been plotted as a function of the measured pressure. The pore volume
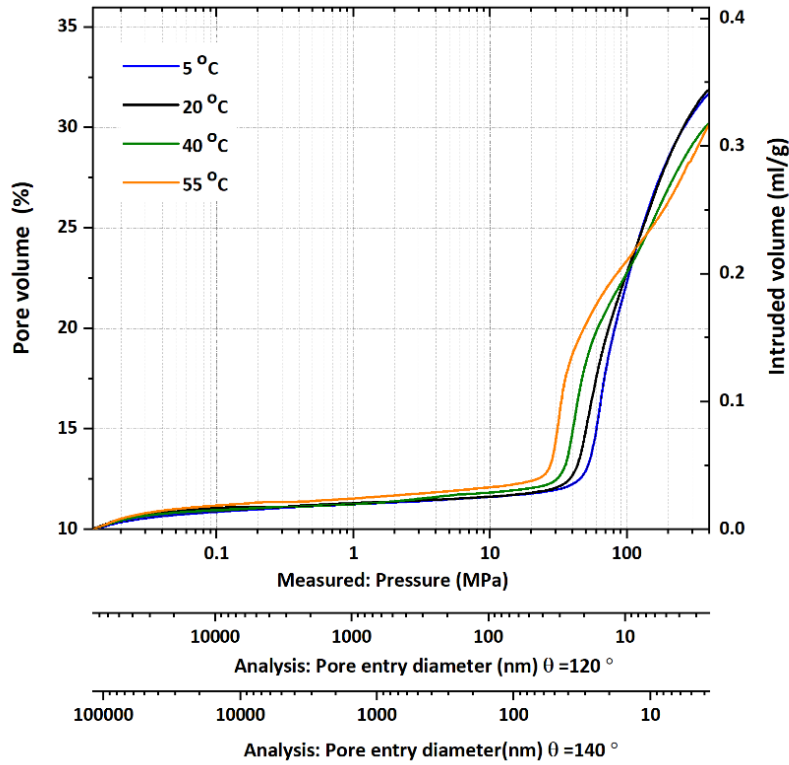
Figure 4.9: Pore and intruded volume, from the MIP analysis, as a function of applied pressure. The corresponding pore entry diameter has been plotted using 140° and 120 ° as contact angle).

and the corresponding intruded volume (in brackets) were found to be 31.9% (0.33 ml/g), 32.1% (0.34 ml/g), 30.5% (0.31 ml/g), and 30.2% (0.31 ml/g) for samples cured at 5, 20, 40 and 55 °C, respectively. Using the Washburn equation, the corresponding pore entry diameters have been plotted using the contact angles of 120° and 140°. Müller *et al.* showed that the contact angle of 120° is more suitable for the analysis of cement pastes [106] and therefore, has been used to report the threshold pore entry diameter (the minimum diameter which is geometrically continuous throughout the whole sample). It was found that this diameter increases from 19.3 to 35.3 nm as the curing temperature increased from 5 to 55 °C.

Figure 4.10 shows the pore volumes obtained using the mass/volume balance equations and compares the accessibility of these pore volumes by DVS and MIP. It can be clearly observed that only a part of the C-S-H gel volume is accessible by MIP. Furthermore, the amount of MIP accessible gel pore volume is higher for the samples cured at 5 and 20 °C as compared to the gel pore volume for samples cured at elevated temperatures of 40 and 55 °C, which merits further investigations. The

moisture desorption isotherms can be used to quantify the capillary and gel water content by accounting for heterogeneous and homogeneous cavitation. The accessible porosity, calculated through desorption isotherms, has also been presented in figure 4.10. Additionally, the figure also shows the amount of gel pores that are emptied after homogeneous cavitation (indicated by double-headed arrows)
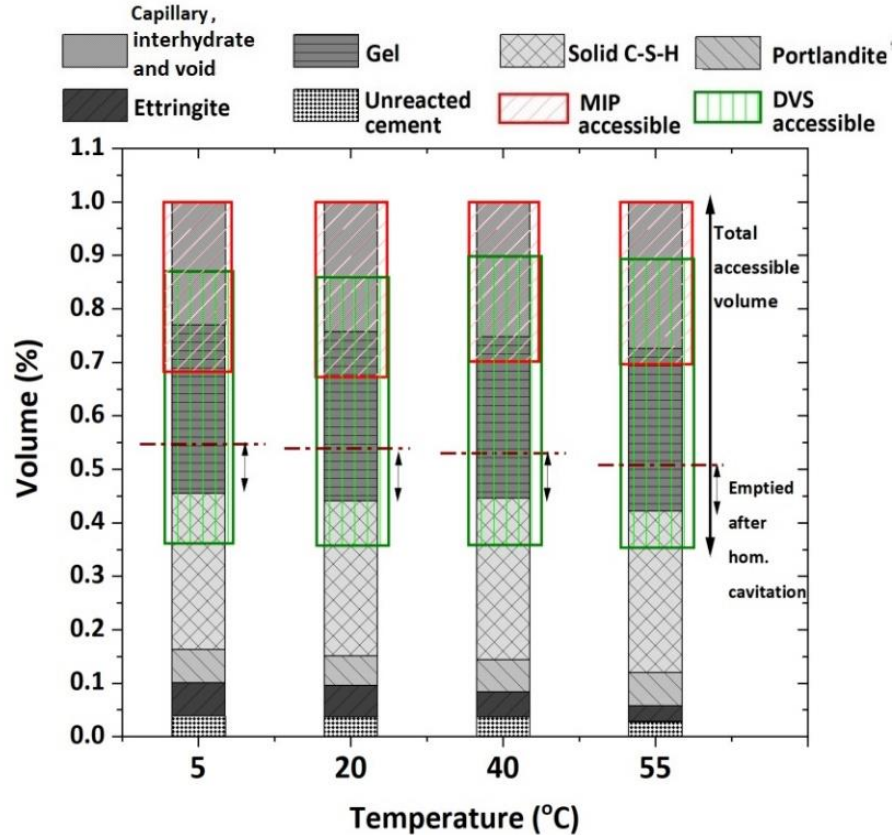
Figure 4.10: Pore volumes of the various samples and the comparative overview of the pore volumes accessible by DVS and MIP measurements. Double headed arrows indicate the amount of gel pores that were emptied after homogeneous cavitation.

for the different samples considered in this study.

4.4   Conclusions

This study indicates that curing at elevated temperatures increases the coarse porosity and decreases the gel pore content, which is in good agreement with several other studies. The number of H_2O moles per moles of C-S-H decreased from

5.8 for sample cured at 5 °C to 5.1 for the sample cured at 55 °C. The Ca/Si ratio was not significantly affected by hydration temperatures considered in this study.

The capillary water contents obtained in the regime of $m_s - m_{0.78}$ and gel water contents obtained in the regime $m_{0.78} - m_{0.28}$, from the desorption isotherms by using the DVS technique were found to be in good agreement with those obtained from mass balance calculations. The gel porosity that is emptied after homogeneous cavitation was found to decrease with an increase in the curing temperature. Additionally, it was observed that MIP completely captures the coarse porosity. Nevertheless, only small volumes of C-S-H are accessible using this technique.

Acknowledgements

Supporting information

SI4 (I) Isothermal calorimetry

An isothermal calorimeter (TAM from TA instruments) has been used to optimize the content of hemihydrate by recording the heat released from hydrating cement pastes as shown in figure 4-A1. Its dosage was selected such that the aluminate peak occurs at least 2 hours after the alite peak. Finally, 5.5 wt% HH of anhydrous cement was determined to be the optimum content.
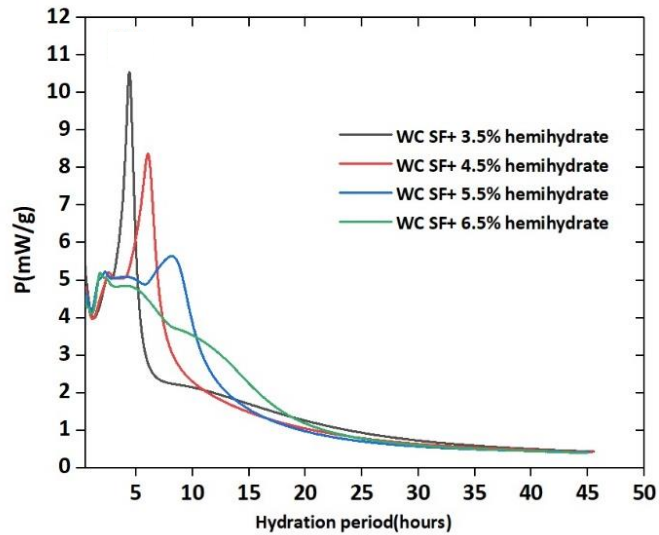
Figure 4-A1 Heat of hydration of cement paste with different dosage of hemihydrate as the function of time.

SI4 (II) Water content distributions

The following table 4-A1 gives the initial and final values of the calcium content of various phases that were used to determine the water content distribution in C-S-H.

Table 4-A1: The values for the initial and final content of calcium content in pastes cured at various temperatures for 90 days. The values are provided in grams and have been normalized per 100 g of cement paste. Measurement error is ±2 %.

Phase	Initial Content	Curing temperature			
		5 °C	20 °C	40 °C	55 °C
		(Final content)			
C_3S	17.41	2.14	1.93	1.76	1.78
C_2S	6.65	2.01	1.98	1.95	1.89
From other phases (CH+C_3A+HH)	3.05				
Portlandite		4.6	4.53	4.41	4.39
Ettringite		1.6	1.52	1.24	0.89

SI4 (III) Insights from nitrogen sorption

The cement pastes cured for 90 days at various temperatures of 5, 20, 40, and 55 °C were also investigated by N_2 sorption. The analysis was carried out using Autosorb-1 sorption instrument (Quantachrome Instruments). Nitrogen sorption is a manometric technique in which the adsorbed amount is determined by subtracting the amount of gas in the dead space from the total amount of gas that enters the sample test tube with the adsorbent. In this technique, it is crucial to remove all adsorbed gas molecules and start the measurements in a vacuum. This is significantly challenging because the initially dried samples are further subjected to a degassing procedure at an elevated temperature. For the samples under study, an optimum vacuum degassing temperature of 60 °C was selected. The period of degassing was 6 hours. Two repetitions on each sample were carried out to obtain the nitrogen sorption data. The degassing measurements were also made at temperatures of 40 and 50 °C. However, these temperatures were not found to be adequate due to low-pressure hysteresis and lack of reproducibility of the isotherms.

Before discussing the results from nitrogen sorption isotherms, it is also crucial to consider the microstructural changes which are induced solely due to the

degassing procedure. MIP was carried out on these samples (in the same way as described in section 4.3) and the intrusion data has been presented in figure 4-A2. Though MIP probes small volumes of C-S-H, nevertheless, an approximate overview of the microstructure for comparative purposes can be estimated. The pore volume (%) and the corresponding intruded volume (in brackets) were found to be 21.9% (0.32 ml/g), 22.1% (0.32 ml/g), 24.5 % (0.34 ml/g), and 26.8% (0.36 ml/g) for samples cured at 5, 20, 40, and 55 ℃, respectively. The microstructural changes could be observed in all the degassed samples as compared to solvent exchange dried
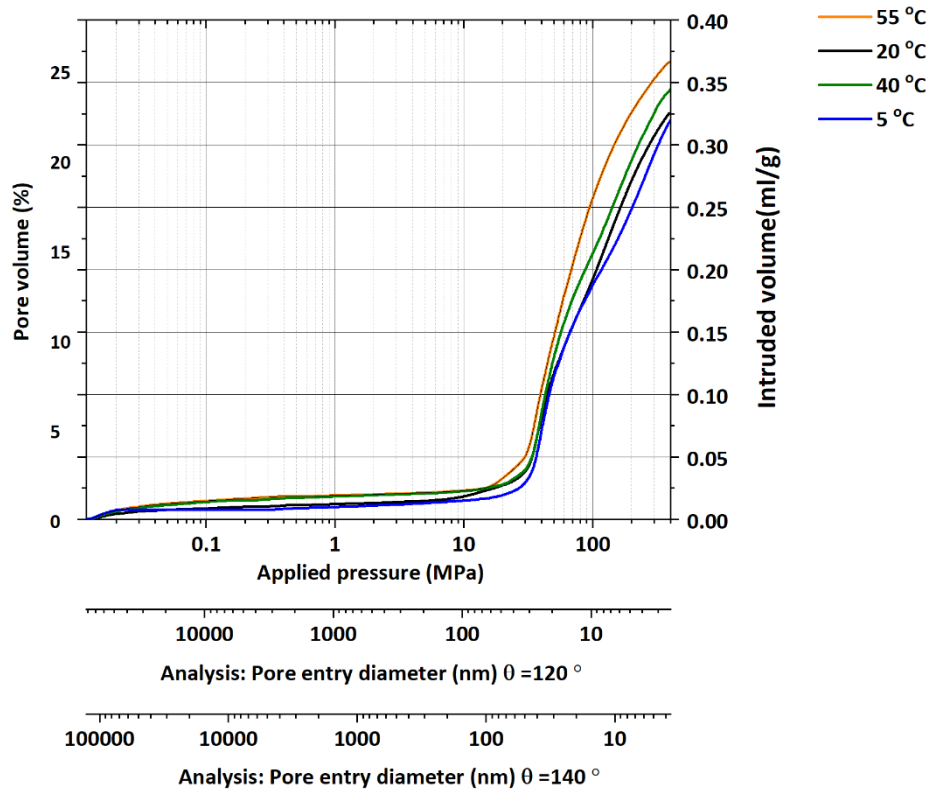
Figure 4-A2: Pore volume and intruded volume for the dried and degassed samples obtained from the MIP analysis as a function of applied pressure. The corresponding pore entry diameter has been plotted using 140° and 120 ° contact angle).

samples (section 4.5). The threshold diameter was observed to be nearly the same for all the samples, and the gel and capillary pore volumes intruded by MIP increased as a function of curing temperature.

It is interesting to note that similar observations were reported by Bahafid *et al.* for freeze-dried samples cured at 7, 20, and 40 °C [57]. The freeze-drying method is a relatively harsh method for drying or arresting the hydration in terms of preserving the microstructure and has been noted to induce damaging stresses from volume expansion, hydraulic pressure, and crystallization pressure[70,98,107]. Müller *et al.* compared MIP results for different drying methods and reported that the total capillary pore volume intruded by MIP was higher for the freeze-dried samples as compared to the solvent exchanged samples[59]. Therefore, it can be concluded that harsher drying methods can drastically change the microstructure of the cement pastes. This in turn makes the direct comparison of nitrogen and water sorption isotherms very challenging, despite the starting drying method being solvent exchange.

The nitrogen sorption isotherms obtained on the dried and degassed samples are shown in figure 4-A3(a) and have been normalized with respect to the mass of the dried cement sample (similar to water sorption isotherms). The desorption isotherms are preferred over absorption isotherms to investigate the Barret-Joyner-Halenda (BJH) pore size distributions. The corresponding BJH pore size distributions have been shown in figure 4-A3(b). Similar to homogeneous cavitation in water desorption isotherm, nitrogen desorption isotherm is affected by the tensile strength effect at around 0.4 p_v/p_{sat}. Consequently, a sharp peak is observed at 3.4 nm diameter, which is an artefact and should be ignored for comparing the pore size distributions.
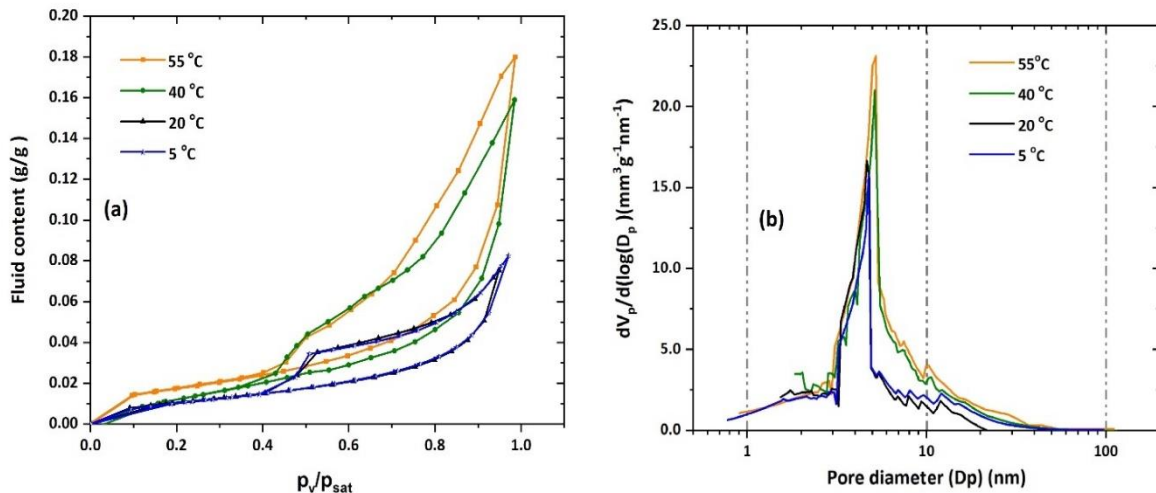
Figure 4-A3: (a) Nitrogen sorption isotherms for the dried and degassed samples, and (b) the corresponding BJH pore size distributions obtained from the desorption isotherms.

The total content and the differential pore volumes intruded by nitrogen increase as a function of curing temperature. The results are qualitatively in good agreement with the MIP results. The pore volume (%) as provided by nitrogen desorption was found to be 11.2%, 12.1%, 16.5%, and 17.1% for the samples cured at 5, 20, 40, and 55℃, respectively. This is expected as the highest p_v/p_{sat} attainable by nitrogen is 0.96 and the diameter that can be probed by nitrogen sorption is 47.2 nm. Hence, the capillary pore volume is only partially accessible. Furthermore, Tennis and Jennings proposed that the C-S-H can exist as low and high density (LD and HD C-S-H) based on the difference in their packing densities. It was reported that even though water can access both LD and HD C-S-H, only LD C-S-H is accessible by nitrogen[27,28]. Therefore, it can be concluded that, unlike water, the interlayer spaces and small gel pores or the gel pores that are accessible by interlayer spaces are not expected to be probed by nitrogen.

Moisture sorption (absorption→desorption) isotherms were also obtained for the dried and degassed sample cured at 55 ℃. Figure 4-A4 provides the comparative overview of the moisture sorption isotherms (desorption→absorption) on the as-prepared samples and moisture and nitrogen sorption isotherms (absorption→desorption) on the dried and degassed sample. The differences between nitrogen and moisture sorption isotherm are expected as one is gravimetric and the other is volumetric and also owing to a difference in the size of the probe molecules. Nevertheless, the information from moisture sorption isotherms of the as-prepared sample cannot be compared with that obtained from nitrogen sorption isotherm, as reported in several studies. Recently, Pellenq and co-workers[108] reported that the pore size distributions obtained from nitrogen sorption isotherms are more representative of the microstructure of 'as-prepared' samples. Nevertheless, the experimental investigations in this study clearly show the striking difference in the starting microstructure.
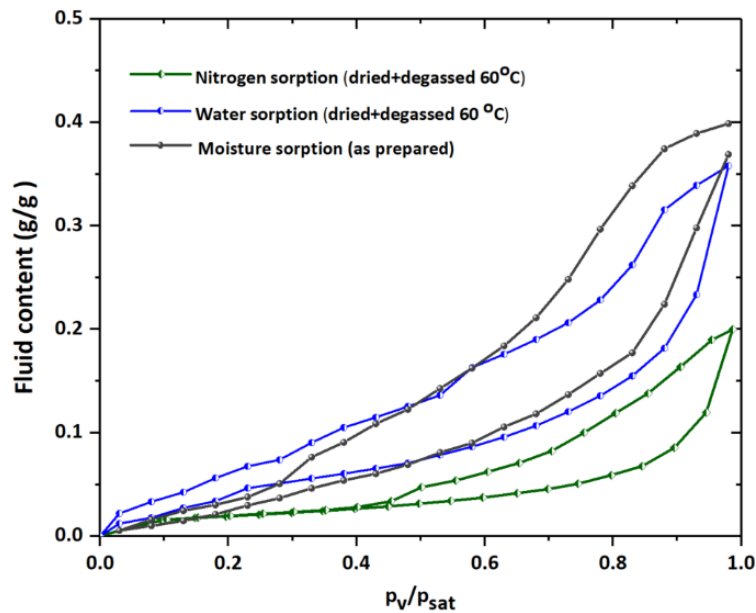
Figure 4-A4: Moisture sorption isotherm of the as-prepared, and dried and degassed sample as compared to the nitrogen sorption isotherm of dried and degassed sample.

A comparison between moisture absorption isotherms of the dried and degassed sample with that of the as-prepared sample revealed that moisture uptake increases slightly in the lower p_v/p_{sat} regime (0-0.43) and decreases afterwards. This could be attributed to microstructural rearrangements or surface interactions that would be considerably different in the dried and degassed samples because of solvent exchange. Additionally, on assessing the moisture desorption isotherms in both the systems, the lower desorption amount from the dried and degassed sample in the higher p_v/p_{sat} regime (0.96- 0.6) could be attributed to partially filled capillary pores, as the sample was not saturated in distilled water before measurement. Overall, the moisture sorption isotherms of the 'as-prepared' and dried and degassed samples clearly show the drastic difference in the microstructures between the samples.

Chapter 5   The sorption behaviour of calcium-silicates-hydrates synthesized using different techniques

Monisha Rastogi[ab], Adrian Alexandru Pirvan[ab*], Maya Harris[b*], Mohsen Ben Haha[a], Karen L. Scrivener[b]

[a]HeidelbergCement Technology Center, Leimen, Germany

[b]École polytechnique fédérale de Lausanne, Switzerland

Note: This chapter is a "manuscript in preparation" that is planned to be submitted as a research article.

Contribution of the doctoral candidate: Writing of the first manuscript draft, experimental design, Carrying out the experiments presented in the manuscript, editing and compilation of input from the other authors.

Abstract

This study examines the moisture desorption response of calcium-silicates-hydrates (C-S-H) synthesized using three different techniques. In the first technique, C-S-H has been prepared using double decomposition and dropwise precipitation method. The second technique involves hydration of reactive belite binder to produce samples with maximized C-S-H content. In the third technique, white cement is mixed with silica fume to increase the content of C-S-H and decrease the content of other phases. Several characterization techniques including XRD, SEM, TGA, and MIP have been used to assess the microstructure of cementitious materials. Thereafter, the desorption behaviour of all the C-S-H samples has been compared. The effect of varying the calcium to silica (Ca/Si) ratio on the desorption behaviour has also been investigated for several samples.

Keywords: C-S-H, synthetic C-S-H, moisture desorption, water vapour sorption isotherms.

* Authors equally contributed to this work

5.1   Introduction

C-S-H, the main hydration product of hardened cement paste, has a complex microstructure. The characterization of C-S-H is also difficult as the water is an intrinsic part of C-S-H and most of the probing techniques require removal of this water, which damages its delicate microstructure. Water vapour desorption is one of the few methods that can be used to investigate the microstructure of 'as-cured' or 'as- prepared' C-S-H. Water vapour sorption isotherms (WVSIs) provide the relationship between the moisture content in the cementitious materials and the relative humidity of the surrounding environment. Water has a very small kinetic diameter of 0.28 nm, and the sorption behaviour can be acquired at room temperature. Therefore, WVSIs are extensively used to provide insights into the microstructural properties (such as pore size distribution, specific surface area and total accessible porosity) of hardened cement pastes [39,40,55,58,60]. However, to understand and characterize C-S-H, it would be useful to first synthesize C-S-H without the presence of other phases.

In this study, samples with maximized C-S-H content have been prepared using three different techniques and their water desorption behaviour has been compared. In the first technique, a combination of direct double decomposition and dropwise precipitation has been used. In the second technique, reactive belite binder has been hydrated to produce samples with maximized C-S-H content. Finally, the third method involved using white Portland cement and silica fume to produce the C-S-H samples.

It has been observed that the change in the Ca/Si ratio results in the variation of several properties. For instance, basal spacing has been found to vary with the Ca/Si ratio and, according to a recent review, a decreasing trend in the basal space has been observed with an increase in the Ca/Si ratio[109]. Using small-angle neutron scattering (SANS), Chen *et al.* reported that the surface area of C-S-H decreases with an increase in the Ca/Si ratio[110]. Further, several experimental investigations and simulations indicate that the water content in C-S-H increases linearly with an increase in the Ca/Si ratio [111–113]. Nevertheless, owing to the difference in the degree of drying, it is challenging to assess the type of water being

investigated. In the experimental investigations involving severe drying (above 110 °C), the measured water content seems to be that of the interlayer and was found to increase with an increase in Ca/Si ratio[112,114].

These conclusions were found to be in good agreement with the results obtained using ^{1}H NMR relaxometry and SANS experiments as well as Grand Canonical Monte Carlo (GCMC) calculations [105,115,116]. However, in some mild drying experiments (below 110 °C) in which the surface water could also be included with interlayer water, this trend was not observed[1,117,118]. Therefore, the effect of variation of the Ca/Si ratio of various C-S-H samples on water desorption isotherms is also an interesting subject for investigation and hence, also forms a part of this study.

The microstructure of all the samples has been characterized using mercury intrusion porosimetry (MIP), scanning electron microscopy- energy-dispersive X-ray spectroscopy (SEM-EDX), X-ray diffraction (XRD), and thermogravimetric analysis (TGA) prior to the comparison of the water sorption behaviour.

5.2   Materials and methods

5.2.1   C-S-H synthesis by dropwise precipitation and its characterization

The C-S-H samples synthesiszed using this technique has been prepared and characterized by Maya Harris at EPFL. This synthesis technique uses a special reactor that controls the reaction conditions including Ca^{2+} ion concentration, pH, and conductivity. Complete details for the setup have been previously reported[119]. Briefly, calcium nitrate tetrahydrate (Sigma-Aldrich), sodium metasilicate (Sigma-Aldrich), and sodium hydroxide (Acros Organics) are used to prepare solutions with decarbonated water. To simulate the relationship between the Ca/Si ratio of synthetic C-S-H and pH, the Gibbs Energy Minimization Software (GEMS) is used, as alkalis are introduced in the system. Low temperatures (around 19 °C) are maintained throughout the synthesis procedure to avoid precipitation of portlandite. 100 mL of 0.224M calcium nitrate tetrahydrate and 0.1M sodium metasilicate were simulated at equilibrium with varying amounts of pH regulator, NaOH, as shown in Table 5.1 to achieve the listed target Ca/Si values.

Table 5.1. The values for the targeted Ca/Si ratio and the corresponding pH and NaOH concentration determined using GEMS.

Target Ca/Si	pH (GEMS)	10M NaOH (GEMS)
1	11.4	75 µL
1.3	11.9	675 µL
1.5	12.5	1.625 mL
1.8	12.9	3.475 mL
2	13.5	10 mL

The reactor was then purged under a flow of nitrogen at 10 mL/min and mixed at 700 rpm for a minimum of 30 minutes to ensure an even distribution of NaOH. Once the reactor reached the desired temperature, the mixing speed was increased to 1100 rpm, and 100 mL of 0.224M calcium nitrate tetrahydrate solution was introduced into the reactor at a rate of 2 mL/min. After a minimum of three hours, the precipitate was taken out of the reactor and stored as suspension. For drying, 25 grams (wet) of the filtered sample was placed in a -80 ℃ freezer for 24 hours, then freeze-dried for an additional 24 hours in an Alpha 1-2 LD plus freeze dryer operating at -50 ℃ and 0.01 mbar. The samples were later washed either with isopropanol or water.

PANalytical X'pert X-ray diffractometer with monochromatic Cu-Kα radiation was used to carry out X-ray powder diffraction. The samples were prepared through the back-loading process. XRD pattern was acquired in the range of 5°-70° (2θ) with a fixed divergence slit of ½ and a step size of 0.017° with a total measurement time of 30 min.

For TGA analysis, a Mettler Toledo AG (TGA/SDTA851e) was used in which the dried C-S-H was heated from 30 to 1000 °C under a flow of nitrogen at 10 mL/min.

For TEM analysis, 50 mg of sample was dispersed in 40 mL of isopropanol. A drop of the suspended liquid was allowed to dry on a copper grid (200 mesh grids). The copper grids were glow discharged before sample disposition. Subsequently, the samples were imaged at room temperature using a Tecnai F20 TEM (FEI, The Netherlands) operating at an acceleration voltage of 100 kV (LaB$_6$ gun) with a line resolution of 0.34 nm. The images were recorded on a high sensitivity 4k x 4k pixel CCD camera.

More details describing additional characterization results, filtering, handling, and storage of synthetic C-S-H shall be made available in an upcoming publication[120].

5.2.2 C-S-H synthesis by belite hydration and its characterization

Alexandru Pirvan was responsible for syntheisizing and characterizing C-S-H samples using the belite hydration technique. In this technique, initially, α-C$_2$SH (provided by HeidlebergCement) was used which was hydrothermally synthesized using calcium hydroxide, reactive silica, and fine α-C$_2$SH seeds. The resulting product was autoclaved and dried at 105 °C for 24 hours. Thereafter, the material was ground using a grinding aid (SikaGrind®-870), such that the d$_{50}$ value of the resulting powder was less than 3 μm. Finally, the powder was calcined at an optimum temperature of 460 °C for 2 hours. Prior to hydration, the powder was again ground in a disk mill to break any lumps formed during calcination.

X-ray fluorescence spectrometry (PANalytical AxiosMax) was used to determine the oxide composition of the synthesized belite binder, the results from which are given in Table 5.2.

Table 5.2. Chemical composition of the reactive belite binder determined by XRF analysis

Oxide	CaO	SiO$_2$	MgO	K$_2$O	Al$_2$O$_3$	SO$_3$	LOI (1050°C)
Amount, %	61.36	33.29	0.57	0.13	0.00	0.17	4.07

For X-ray diffraction analysis and Rietveld refinement, fresh discs of 3 mm thickness were cut from the sealed cylinders after 90 days. A Bruker D8 Advance diffractometer with monochromatic Cu-Kα radiation (λ = 1.541 Å) and a step-size of approximately 0.02° was used to acquire data in the range of 5° to 70° (2θ). The degree of hydration of clinker phases was calculated by Rietveld refinement using Topas software with quartz as the external standard[12].

This binder was mixed with water at w/b of 0.35. A superplasticizer admixture BASF MasterGlenium ACE30 (1% of the mass of the binder) was also used to improve the workability. The raw materials were mixed using a high-speed mechanical mixer (Ultraturrax) at 24000 rpm for 2 minutes. To vary the Ca/Si ratio, silica fume (SF, Microsilica provided by ELKEM) and metakaolin (Metastar 501, Imerys) were also added in different proportions (10-15% weight of binder). All the samples were cured under limewater at 20 °C for 1 year.

All the microstructural characterizations were made on samples dried using the solvent exchange method with isopropanol, followed by a quick washing with petroleum ether[70]. TGA was carried out on a ground hydrated binder using a NETZSCH STA F449 device. The weight loss was monitored while heating a 30±1 mg sample until 1050 °C at 20 °C/min in N_2 atmosphere.

A Zeiss EVO LS10 SEM with a Quantax400 EDS Detector from Bruker was used to investigate the microstructure of the hydrated specimens. For chemical analysis of the C-S-H, EDS point analysis and mapping were carried out on selected areas. All samples for SEM investigations were impregnated under vacuum with a spectrally transparent epoxy resin (EpoTek® 301), gradually polished down to 1 μm with a diamond spray and petrol as a lubricant, and coated with a thin conductive layer of carbon (15 nm).

MIP was carried out on solvent-exchanged crushed samples that were investigated up to a maximum pressure of 400 MPa using a Pascal 140/440 Porosimeter (Thermo Scientific). The surface tension of the mercury was considered as 0.48 N/m.

5.2.3 C-S-H from white Portland cement and silica fume and its characterization

In this synthesis technique, the content of C-S-H was maximized by using the following raw materials: ground white-cement clinker 84.5% by wt.; hemihydrate

(HH) 5.5% by wt., and SF 10% by wt. This binder was mixed with water at a water-to-binder (w/b) ratio of 0.7 using a high-speed mechanical mixer (Ultraturrax) at 24000 rpm for 90 s followed by 30 s of lowering the speed (24000-0 rpm). The samples were cured at 5, 20, 40, and 55 °C under distilled water for 90 days prior to the measurements. The effective w/b of the samples, found to be around 0.78(± 0.1), has been determined using the ignition test and accounting for loss on ignition, as described elsewhere [102].

XRD and Rietveld refinement was carried out on the samples in the same way as described in section 5.2.2. For MIP, TGA, and SEM-EDX analysis, samples were dried using solvent exchange procedure, as previously described. These samples were also characterized using the same equipment and procedure as described in section 5.2.2.

5.2.4 Sorption isotherm acquisition

Sorption isotherms for all samples were acquired using dynamic vapour sorption (DVS). Measurements were carried out on as-prepared samples using a DVS Adventure and DVS Endeavour (Surface Measurement Systems). The sorption temperature was 20 °C for all samples. Samples weighing ~25 mg were crushed and subjected to drying or desorption with the starting point at 0.98 p_v/p_{sat}, followed by step-wise data acquisition from 0.98 to 0.03 p_v/p_{sat} with a step size of 0.05. For the control sample, data was also acquired at additional steps. The initial mass from the balance (once the balance was considered stable) was also recorded and considered to be nearly equal to the mass of the saturated sample m_s ($p_v/p_{sat} \approx 1$). Mass equilibrium was identified as the point at which the mass change was less than 0.0001 mg/min or exceeding the assigned time limit which was 1440 mins for 0.98 p_v/p_{sat} step and 720 mins at all other steps. If the equilibrium was not attained in the given time interval, the moisture content was extrapolated by using the asymptotic function for moisture ratio MR:

$$MR = \frac{m_t - m_0}{m_{eq} - m_0} = 1 - \exp(-k_m t) \tag{5.1}$$

m_t: mass at time t

m_0: mass at time 0

m_{eq}: Equilibrium mass at a given p_v/p_{sat}

k_m: fitting parameter

This equation has been previously used in several investigations on moisture sorption and is based on the analytical solution of the diffusion equation[39,58,73,74]. The data is normalized to per gram of dry cement paste.

5.3   Results and discussions
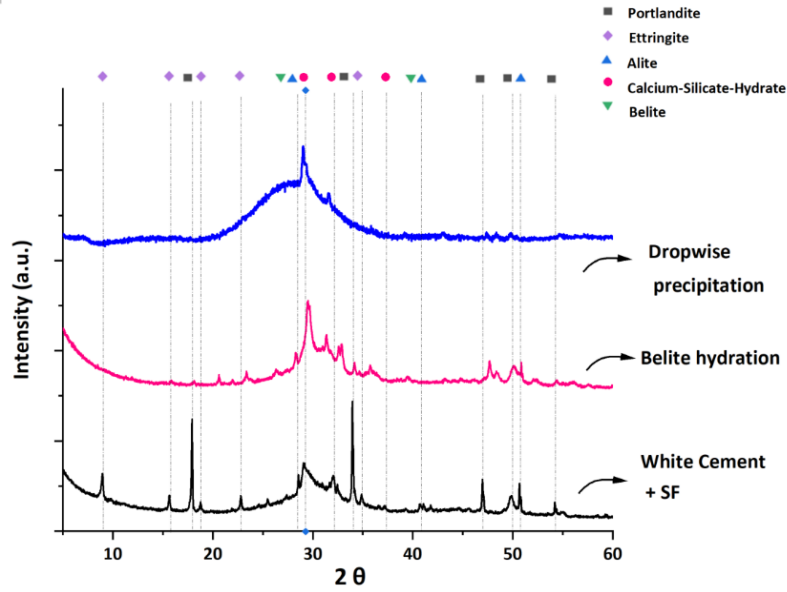
Figure 5.1: XRD patterns for the 'as-prepared' samples synthesized by double decomposition and dropwise precipitation method with Ca/Si ratio 1.5 (indicated in blue), using belite hydration technique with Ca/Si 1.94 (indicated in pink) and by the technique involving mixing of white cement and silica fume and cured at 55 °C with Ca/Si 1.45 (indicated in black).

5.3.1   Microstructural characterization

Figure 5.1 provides a comparative overview of the X-ray diffractograms of a representative sample from each synthesis technique. The characteristics peaks of C-S-H at 2θ of 29.4 and 32.1 ± 0.1° can be observed for all the C-S-H samples. For the wet samples prepared using the dropwise precipitation technique (immediately after filtration) with Ca/Si of 1.5, the signal is slightly subdued due to the presence of water. No other phase was detected for the samples synthesized using this

technique for Ca/Si less than 1.5. Some portlandite was detected for samples with a higher Ca/Si ratio and further details on the same can be found in an upcoming research article [120].
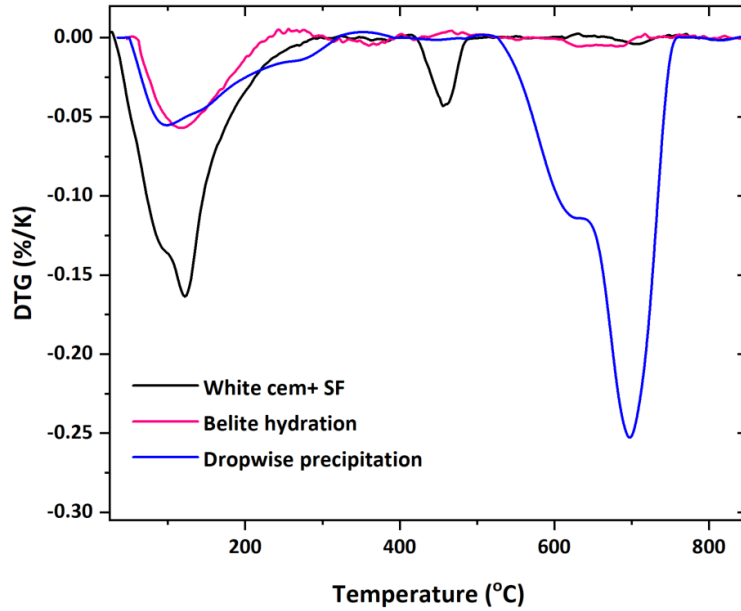
Figure 5.2: DTG curves for the C-S-H samples synthesized by double decomposition and dropwise precipitation method with Ca/Si of 1.5, belite hydration technique with Ca/Si of 1.94, and the technique involving mixing white cement and silica fume and cured at 55 °C with Ca/Si of 1.45.

Figure 5.2 shows the DTG curves for a representative sample from each synthesis technique. As shown in figure 5.2 and reported in [120], the synthetic C-S-H is susceptible to carbonation in air when subjected to TGA analysis. The losses due to carbonation in air were observed in C-S-H samples irrespective of the presence of the portlandite. The results were also verified using inductively coupled plasma spectrometry (in optical emission spectroscopy mode).[120]

The phase assemblage of the representative C-S-H samples synthesized using the belite hydration technique and the technique involving white cement and silica fume, as determined using XRD Rietveld refinement, are given in table 5.3. Additionally, portlandite content has been determined using TGA with the tangent method. The data has been normalised per 100 g of paste.

Table 5.3: Phase assemblage of the pastes synthesised by the two techniques as quantified using XRD Rietveld refinement. Portlandite content was quantified using TGA. Measurement error is ± 2%.

Phase		Belite hydration	White cement +SF
Clinker phases (C₃S, C₂S)/unreacted phases		9.4	7.7
Ettringite (AFt)		-	3.6
Portlandite (CH)/other phases (afwillite, dellaite, scawtite, killalaite)	Rietveld	13.2	8.1
	TGA	14	8.9
Amorphous content/C-S-H		71.6	80.5
Calcite (or aragonite)		6	-

Figure 5.3 (a) shows the TEM images for the C-S-H sample with Ca/Si of 1.5 with nanofoil morphology and agglomeration. Figure 5.3 (b) show the SEM micrograph for the hydrated sample prepared using belite hydration. The Ca/Si ratio determined using EDS analysis was found to be 1.94. The Ca/Si ratio was varied using different proportions of SF and MK as well as their combination. Based on the EDS analysis, the samples that are selected for water desorption behaviour are provided in table 5. 4 along with their Ca/Si ratios. Figure 5.3 (c) shows the SEM micrograph for the sample synthesized using white cement and SF and cured at 55 °C for 90 days. The Ca/Si ratio was found to be 1.41. For the samples cured at 5, 20, and 40 °C, the Ca/Si was not found to vary significantly and was in the range of 1.4-1.5.
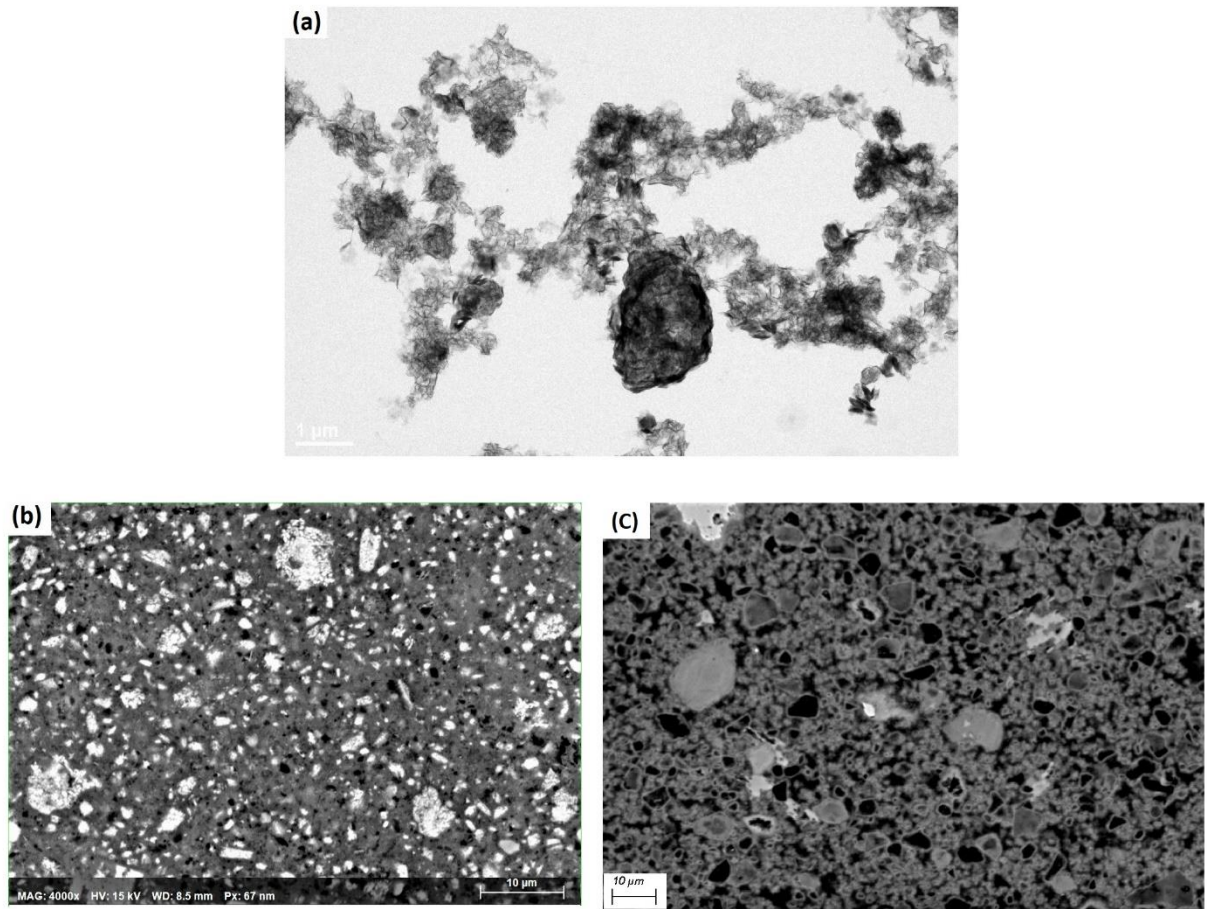
Figure 5.3: (a)TEM images for the C-S-H sample with Ca/Si of 1.5 with nanofoil morphology and agglomeration. SEM micrographs for (b) the C-S-H phase synthesized using belite hydration technique with Ca/Si 1.94 and (c) samples prepared with white cement and SF and cured at 55 °C with Ca/Si of 1.45.

Table 5.4: Various samples prepared using belite hydration and the respective Ca/Si as determined using EDS analysis and selected for water desorption isotherms.

Ca/Si ratio (SEM)	Sample composition
+/-0.04	(w/b=0.35)
1.94	C_2S
1.70	C_2S + 10% MK
1.43	C_2S + 10% SF
1.30	C_2S + 15% SF
1.23	C_2S + 10%SF + 10%MK

Figure 5.4 (a) shows the MIP data for the various samples prepared using belite hydration technique. Figure 5.4 (b) shows the MIP data for samples prepared by mixing white cement and SF, and curing at temperatures of 5, 20, 40, and 55 °C. Using the Washburn equation, the corresponding pore entry diameters have been plotted using the contact angle of 120° and 140°. Using ^{1}H NMR relaxometry, Müller *et al.* showed that the contact angle of 120° is more suitable for the analysis of cement pastes [106] and therefore, has been used to report the results. The threshold pore entry diameter (the minimum diameter which is geometrically continuous throughout the whole sample) for the various samples prepared using these two techniques has been shown in Table 5.5.
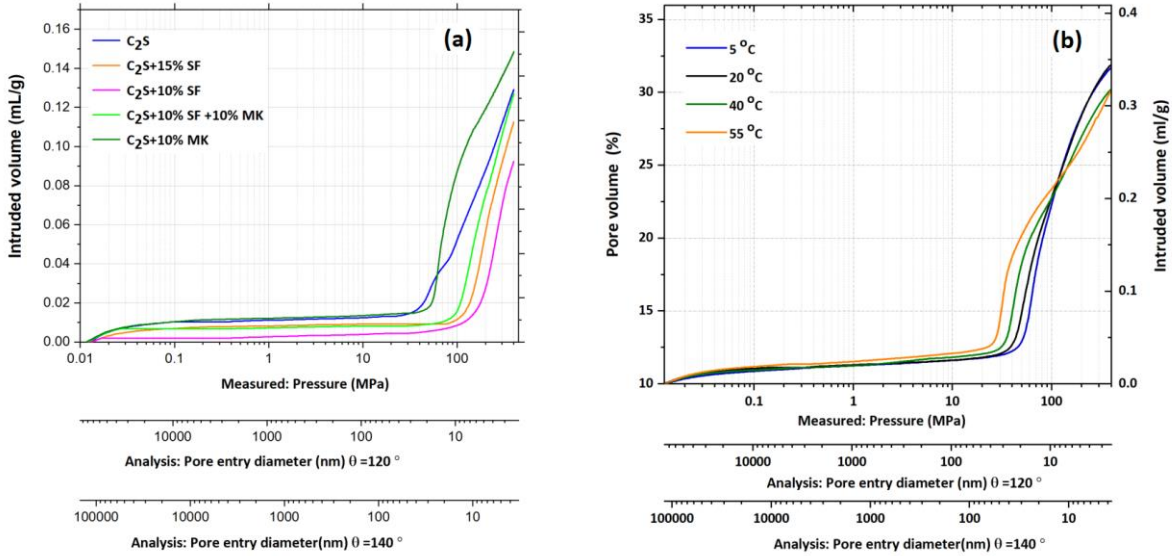
Figure 5.4: MIP curves for the (a) C-S-H samples synthesized using belite hydration technique using SCM and; (b) samples prepared with white cement and SF and cured at 5, 20, 40, and 55 °C.

Table 5.5: Threshold pore entry diameters for various samples prepared using belite hydration technique and the technique involving the mixing of white cement and SF.

Technique: Belite hydration	Threshold pore entry diameter (nm)	Technique: mixing white cement and silica fume	Threshold pore entry diameter (nm)
C_2S	26.2	Cured at 5°C	19.3
C_2S + 10% MK	18.1	Cured at 20°C	24.6
C_2S + 10% SF	7.2	Cured at 40°C	31.2
C_2S + 15% SF	7.8	Cured at 55°C	35.5
C_2S + 10%SF + 10%MK	9.2		

For samples prepared using belite hydration technique, it was found that the samples with SF have a lower threshold pore entry diameter as compared to samples without SF. This can be explained by the filler effect of SF that reduces the porosity in hardened cement pastes[121–123].

Further, for the technique involving mixing white cement and silica fume, the threshold diameter was found to increase from 29.1 to 66.2 nm as the curing temperature increased from 5 to 55 ℃. This could be attributed to the coarser porosity that results from the elevated temperatures[13,57,62,94].

5.3.2 Water vapour desorption isotherms

Figure 5.5 shows water desorption isotherms for the synthetic C-S-H samples prepared using dropwise precipitation and double decomposition method. The characterization techniques confirmed the formation of a pure and single-phase C-S-H. However, the water desorption isotherms indicate that the samples are not porous but rather an agglomeration of particles. This behaviour could be observed irrespective of the Ca/Si ratio, or the solvent used for washing the samples. Any microstructural or sorption assessment, hence, could not be made on these C-S-H samples using water desorption isotherms
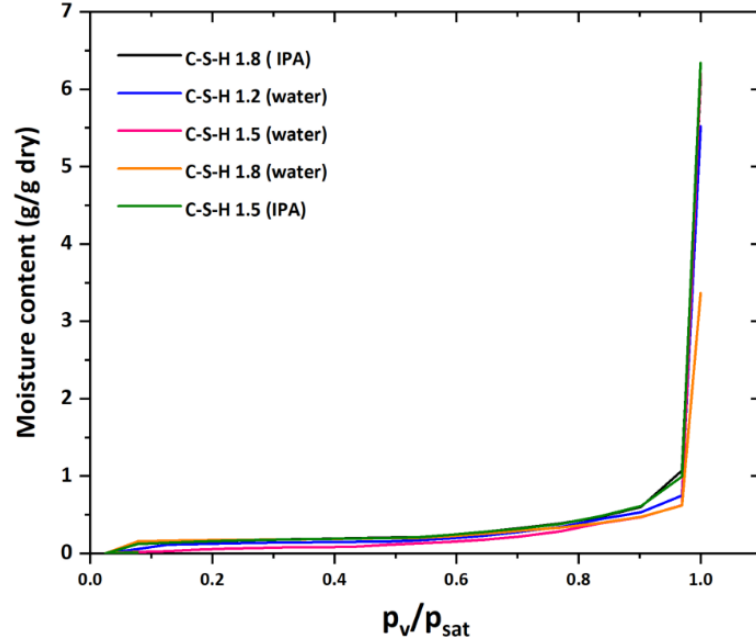
Figure 5.5: Water vapour desorption isotherms of various samples with varying Ca/Si ratio prepared using double decomposition and dropwise precipitation. The solvent used to wash these samples is indicated in the brackets; ISOPROPANOL stands for isopropanol).

Figure 5.6 (a) shows desorption isotherms of the various samples synthesized with the belite hydration technique. The step corresponding to homogeneous cavitation was observed at 0.33-0.38 p_v/p_{sat} for all the isotherms. Figure 5.6 (b)
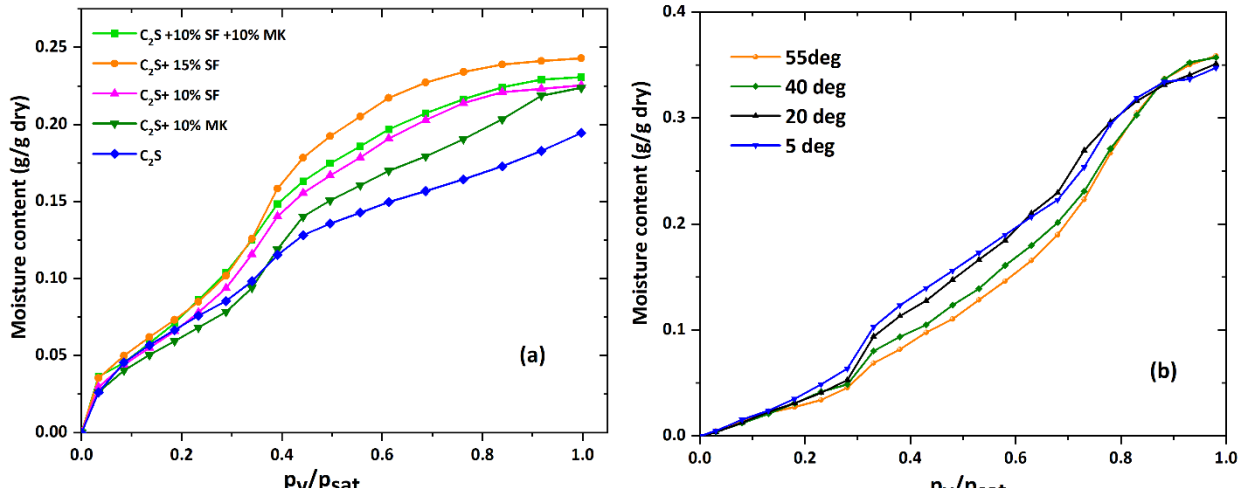
Figure 5.6: Desorption isotherms for the (a) C-S-H samples synthesized using belite hydration technique iusing SCMs; and (b) samples prepared with white cement and SF and cured at 5, 20, 40 and 55 °C.

shows the desorption isotherms for samples prepared using white cement and SF and cured at various temperatures. The step for homogeneous cavitation was observed at the usual position of 0.29-0.32 p_v/p_{sat}.

This shift in the position of homogeneous cavitation towards higher p_v/p_{sat} for samples prepared with the belite hydration technique can be explained by the reduced surface tension of water caused by the superplasticizer used in this study. MasterGlenium ACE30 is polycarboxylate-based-superplasticizer. Several studies have investigated the effect of polycarboxylate superplasticizer dosage on the surface tension of the water. For instance, Li *et al.* studied the hydroxyethyl acrylate-type/ethyl acrylate-type polycarboxylate superplasticizers and reported a 12% decrease in the value of surface tension of water with a dosage of 1% [124]. Similar observations have been reported by several other studies which report a 10-20% decrease in the surface tension of water with low concentration (0.5-1.5 % by wt.) of superplasticizer[125–127].

Assuming, an optimum 10% decrease in the bulk value of surface tension of water, the cavitation pressure for a measurable nucleation rate of 1 cm^{-3}s^{-1} using classical nucleation theory can be calculated as:

$$P^0 \approx \sqrt{\frac{16\pi\sigma_{lv}{}^3}{3kT \ln(\frac{N_A kT}{v_m h})}} \tag{5.2}$$

N_A: Avogadro's constant (6.023×10^{23})

v_m: molar volume of water (1.805 × 10^{-5} m^3/mol)

k: Boltzmann constant

h: Planck's constant

Therefore, for $\sigma_{lv} = 65.57 \, mN.m^{-1}, P^0 \approx 125.5 \, MPa$, and using the Kelvin-Laplace equation, the induced stress at the 0.33-0.38 p_v/p_{sat} is 128-135 MPa. This is in good agreement with the cavitation pressure predicted by the classical nucleation theory.

Further, using BJH method (described in the detail elsewhere [88]), the pore size distributions from the desorption isotherms could be obtained and are shown in figure 5.7. The position of the artefact peak, caused by the homogeneous cavitation
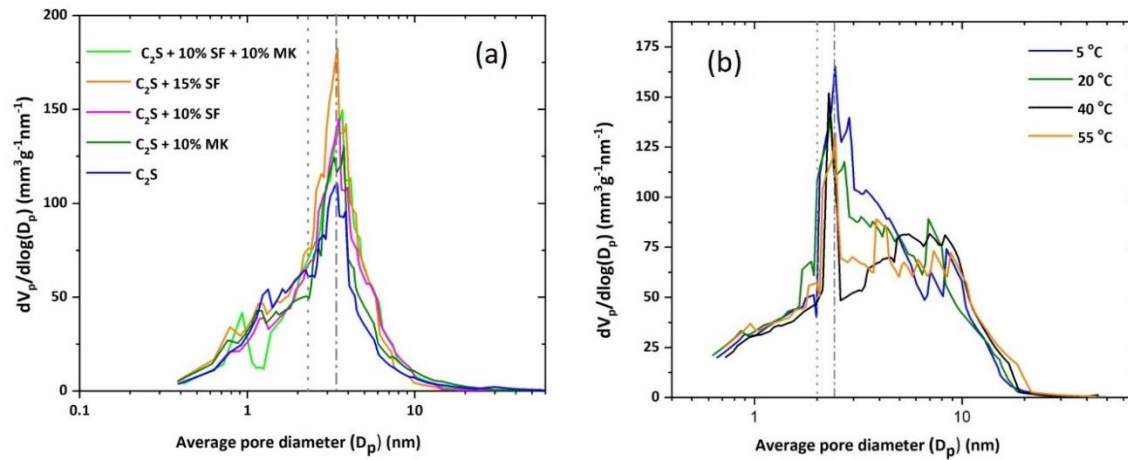
Figure 5.7: BJH pore size distribution for the (a) C-S-H samples synthesized using belite hydration technique including SCMs; and (b) samples prepared with white cement and SF and cured at 5, 20, 40, and 55 °C.

of water, has been indicated by the dashed line (not dotted). For samples prepared using the belite hydration technique, this peak is observed around 3.4 nm (diameter), whereas for the samples prepared by mixing white cement and silica fume it is observed around the usual position of 2.3 nm (diameter).

Assuming that most of the gel pores (70-80%) are emptied before homogeneous cavitation, the gel pore volume can be estimated by integrating the
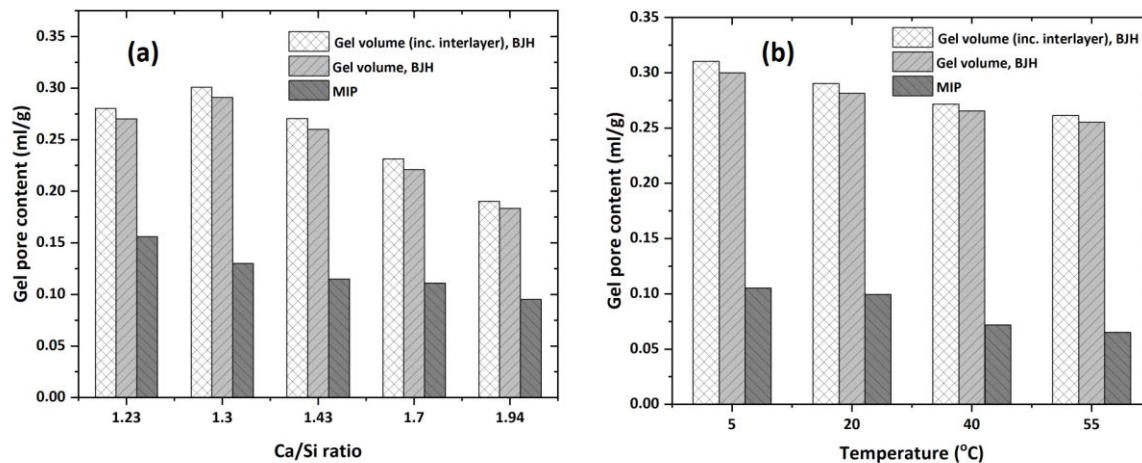
Figure 5.8: A comparative overview of gel pore volumes determined using BJH pore size distribution before and after homogeneous cavitation and that determined from MIP analysis for the samples prepared with (a) belite hydration technique; and (b) technique involving mixing white cement and silica fume.

area under the curve in the range between the dashed line (after the artefacts peak) and 10 nm. This gel pore content has been shown in figure 5.8(a) and (b) for the samples prepared with belite hydration and the technique involving mixing white cement and silica fume, respectively.

Further, as stated in chapter 3 and 4, all the gel pores are emptied after homogeneous cavitation events and are accompanied by the loss of interlayer water as well. This is marked by a dotted line in the BJH pore size distributions and this volume (the total gel with some interlayer volume) has also been plotted in figure 5.8. This volume is equivalent to volume obtained in the regime of $m_{0.78} - m_{0.28}$ from the desorption isotherms. For a comparative overview, figure 5.8 also shows the gel pore volume that has been determined using the MIP data in the range of 2-10 nm for samples prepared through belite hydration and technique involving mixing white cement and silica fume.

As shown in figure 5.8, the gel pore volume determined using MIP is significantly lower (50% or lower) than that determined using DVS technique, an observation previously reported as well[106]. Apart from the fact that mercury only intrudes the connected porosity and the assumptions of the Washburn equation, this difference can also be attributed to the difficulty in determining an accurate value of contact angle, which depends on the surface chemistry, drying techniques, and sample age etc. These factors differ from sample to sample and the contact angle has been reported to vary in the range of 120° to 150°. It is also crucial to note that in this study a contact angle of 120° has been assumed. Increasing the contact angle θ would increase the values for calculated diameters, thus increasing the determined gel pore volume[69].

Furthermore, as reported in chapter 3, some proportion of gel pores (varying from 25-35%) can be only accessed by the interlayer spaces. Therefore, these pores would also not be detected by MIP, despite the smallest diameter which can be probed by MIP is 2.5 nm. Nevertheless, more investigations are required to make further speculations from the MIP data.

5.4   Conclusions

In this paper, we examine the desorption behaviour of C-S-H samples synthesized using three different techniques. The technique involving double

decomposition and dropwise precipitation produces a single-phase C-S-H at the desired Ca/Si molar ratio but lacking in the porous structure. This behaviour was found to be independent of the Ca/Si ratio or the solvent used for washing the samples. Therefore, no microstructural or sorption assessment could be made on C-S-H samples synthesized using this technique. For samples prepared using the other two synthesis techniques, microstructural and sorption assessments could be made using desorption isotherms. The water desorption isotherms prepared using belite hydration method showed that samples containing SF have a finer morphology. This is indicated by the higher gel pore volume. The MIP analysis also indicated a lower threshold diameter for samples containing SF and can be explained by its filler effect. The desorption isotherms of C-S-H samples prepared using white cement and SF at different curing temperatures showed coarsening of the microstructure for the samples cured at higher temperatures (40 and 55 °C). No direct relationship was observed between the Ca/Si ratio and desorption isotherms of C-S-H samples.

Acknowledgements

Chapter 6   On water vapour absorption behaviour of cementitious materials

Monisha Rastogi[ab], Mohsen Ben Haha[a], Karen L. Scrivener[b]

[a]HeidelbergCement Technology Center, Leimen, Germany

[b]École polytechnique fédérale de Lausanne, Switzerland

Note: This chapter is a "manuscript in preparation" that shall be communicated as a research article.

Contribution of the doctoral candidate: Writing of the first manuscript draft, experimental design, Carrying out the experiments presented in the manuscript, editing and compilation of input from the other authors.

Abstract

This study examines the moisture absorption response of hardened cement paste with maximized calcium-silicates-hydrates (C-S-H) content. Both dynamic and static tests are used to study the sorption behaviour. The differential moisture uptake (the difference in the moisture uptake at every step) was found to decrease from 0.18-0.33 p_v/p_{sat} with dynamic vapour absorption tests. In the static tests, this differential moisture uptake increased monotonically. However, for a few p_v/p_{sat} steps, the kinetics revealed that the differential moisture uptake is followed by a gradual decrease in moisture content. Further,sorption isotherms of MCM-41 have been acquired to study the role of surface interactions of water vapour. Finally, the case of isopropanol as an adsorptive has also been discussed.

Keywords: C-S-H, MCM 41, absorption isotherm, isopropanol sorption.

6.1   Introduction

Since the pioneering work of Powers and Brownyard in the 1940s[21], water vapour sorption isotherms (WVSIs) have been used extensively to understand the microstructure of cementitious materials. However, owing to the complex nature of cementitious materials as well as the unusual properties of water at the nanoscale, several aspects of water sorption are still not understood.

For instance, as documented in the work of Powers and Brownyard, sorption experiments on the fine granular samples revealed an initial uptake of the moisture upon exposure to the moist CO_2-free air stream. Thereafter, it decreased marginally with time. This behaviour was observed up to at least 53% RH and disappeared at higher humidity[21,128]. Atlassi *et al.* also reported a similar gain and subsequent moisture loss for the 2-4 mm thick mortar specimens prepared with condensed silica fume and equilibrated at 43% RH[129]. Recently, Burgh *et al.* also studied water vapour absorption and desorption behaviour of hardened cement pastes (hcp) in the form of 4.33 mm thick discs (mean thickness). For samples with sorption behaviour acquired at 23 °C, the kinetics revealed that the moisture uptake is followed by moisture loss, particularly at 33% and 43% RH. This trend was found to be more apparent if the sorption temperature was increased to 40 and 60 °C[13].

In this study, we aim to examine the water vapour absorption behaviour on hcps with respect to structural changes using dynamic and static tests. Dynamic tests allow the control of RH with higher sensitivity. Hence, the structural changes concerning small variations in RH are better reflected. The calcium-silicate-hydrate (C-S-H) content has been maximized in the pastes as most of the moisture-induced structural changes are controlled by C-S-H. The sorption isotherms have also been acquired using the static method (using desiccators with salt solutions) and have been compared with DVS isotherms. Further, the sorption behaviour of MCM-41, a known ordered mesoporous SiO_2 has also been investigated and compared with the cement samples. Finally, the absorption behaviour of common organic solvent, isopropanol has also been investigated as it has significantly lesser polarity compared to the water molecule, and is extensively used in the solvent exchange drying procedure.

6.2   Materials and methods

The white cement samples were prepared in the similar manner as described in previous chapters (3 and 4). Briefly, white cement clinker (Aalborg Portland) with the following phase composition was used: C_3S (65.3 wt.%), C_2S (28.8 wt.%), C_3A (1.9 wt.%), and CH (2.51 wt.%) with the rest of the phases below 1%. To maximise hydration, the clinker was ground to d_{50} and d_{90} values of ~6 and 18 µm, respectively. The condensed silica fume (SF) provided by ELKEM was used to obtain more C-S-H by its reaction with the portlandite. Finally, the following composition was used to maximize the content of C-S-H: ground white-cement clinker 84.5% by wt.; hemihydrate 5.5% by wt., and silica fume 10% by wt. This binder was mixed with water at a water-to-binder (w/b) ratio of 0.7 using a high-speed mechanical mixer (Ultraturrax) at 24000 rpm for 90 s and then for 30 s during lowering the speed (24000-0 rpm). Samples were cured underwater at 5, 20, and 55 ℃ for 90 days.

MCM (Mobil Composition of Matter) no -41 (hexagonal type SiO_2) was provided by Merck. This is an ordered mesoporous material . The material is known to have a simple structure with a well-defined pore shape, narrow pore size distribution. Further, it also has good thermal and mechanical stability. Most importantly, it has deprotonated silanol groups that also exist on the surface of C-S-H. Therefore, absorption isotherms have also been acquired for this relatively simpler material.

Dynamic tests: Measurements were carried out on the dried samples using DVS Adventure and DVS Endeavour (Surface Measurement Systems) devices. The samples were cured underwater at 5, 20, and 55°C for 90 days before measurement of the isotherms. The sorption temperature was 20 °C for all samples. Samples weighing ~25 mg were crushed and subjected to drying at 0.0 p_v/p_{sat}. Thereafter, the absorption isotherm was acquired till 0.98 p_v/p_{sat} with a step size of 0.05. The error in maintaining the desired p_v/p_{sat} was ±0.01. Mass equilibrium was identified as the point at which the mass change was less than 0.0001 mg/min or exceeding the assigned time limit which was 1440 mins. If the equilibrium was not attained in the given time interval, the moisture content was extrapolated by using the using two-phase exponential association equation or parallel exponential kinetics (PEK), which was found to be more suitable for the absorption data.

$$MR = \frac{m_t - m_0}{m_{eq} - m_0} = P\left[1 - \exp\left(-\left(\frac{t}{t_{w1}}\right)\right)\right] + Q\left[1 - \exp\left(-\left(\frac{t}{t_{w2}}\right)\right)\right] \quad (6.1)$$

m_t: mass at time t

m_0: mass at time 0

m_{eq}: Equilibrium mass at a given p_v/p_{sat}

t: Equilibration time in minutes

P, Q, t_{w1}, and t_{w2} are obtained by fitting the equation (6.1).

Static tests: Sorption isotherms were acquired using climate box/desiccators, wherein the salt solutions control the relative humidity. For gentle drying of the samples, silica gel dessicators were used which were purged with nitrogen frequently. Salt solutions of lithium chloride, magnesium chloride, potassium carbonate, magnesium nitrate, potassium chloride, and potassium nitrate were used to create ~ 0.11, 0.33, 0.43, 0.54, 0.85, and 0.95 p_v/p_{sat}, respectively. The samples used were in the form of crushed pieces. The weight of the sample varied from 0.5 to 3 g and the dimension ranged from 1 to 3 cm.

Sorption with isopropanol: A 3 mm thick slice of the sample was cut from the hcp cylinder using an electric saw. This slice was ground using a mortar and pestle and immersed in isopropanol for ~35 days. The isopropanol was changed regularly to maximize the replacement of water-based pore solution. The saturated samples were shipped to Surface Measurements Systems headquarters and isopropanol sorption isotherms were acquired using DVS advantage plus. Around 30 mg of isopropanol saturated sample was introduced in the sample pan and the device was equilibrated at 0.98 p_v/p_{sat} prior to insertion. The samples were dried to 0 p_v/p_{sat} in a stepwise manner with a step size of 0.05 in an isopropanol environment. Thereafter, the absorption isotherm was acquired till 0.98 p_v/p_{sat}, again with the step size of 0.05 p_v/p_{sat}. The error in maintaining the desired p_v/p_{sat} was ±0.01. Mass equilibrium was identified as the point at which the mass change was less than 0.0001 mg/min or exceeding the assigned time limit which was 1440 mins.

6.3   Results and discussions

6.3.1   Dynamic vapour sorption analysis

Figure 6.1 (a) and (b) shows the 'as-acquired' sorption isotherm and the final isotherm obtained after extrapolations for samples cured at 5, 20 and 55°C, respectively. Using sorption kinetics data from each sample, differential moisture uptake (%) has been plotted as a function of p_v/p_{sat} and shown in figure 6.2 (a) and (b). It can be observed that the differential moisture uptake generally increases with an in increase p_v/p_{sat}. An exception is the range from 0.18 to 0.33 p_v/p_{sat} as also indicated by the downward arrow in figure 6.2 (a).

According to classical theories/models such as BET that suggest unrestricted sorption, the differential moisture uptake (%) should monotonically increase as p_v/p_{sat} increases. However, a different behaviour is seen when the adsorbent is C-S-H and the adsorptive is water vapour. C-S-H is comprised of interlayer spaces and
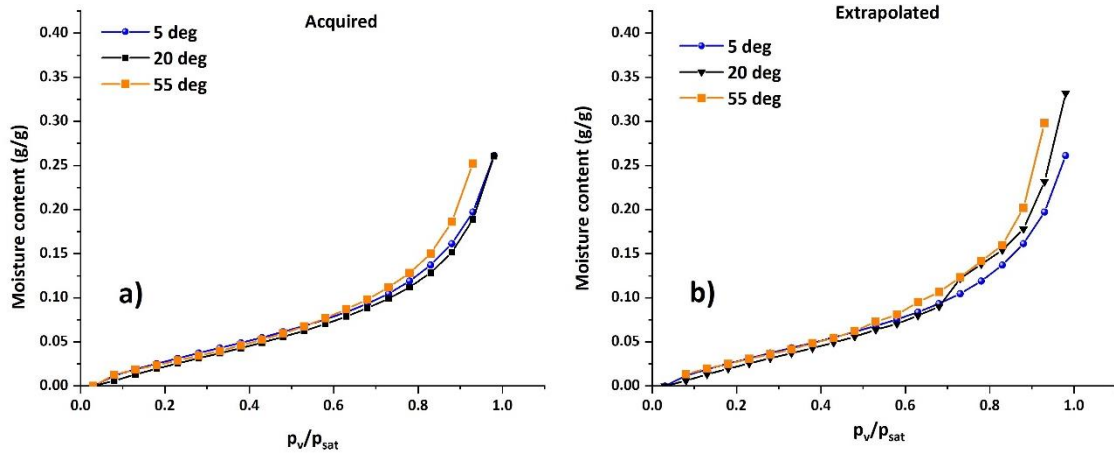
Figure 6.1: (a) As acquired and (b) extrapolated sorption isotherms of the samples cured at 5, 20, and 55°C.

gel pores [130]. It has long been stated that the water sorption in micropores is significantly different than that in mesopores.
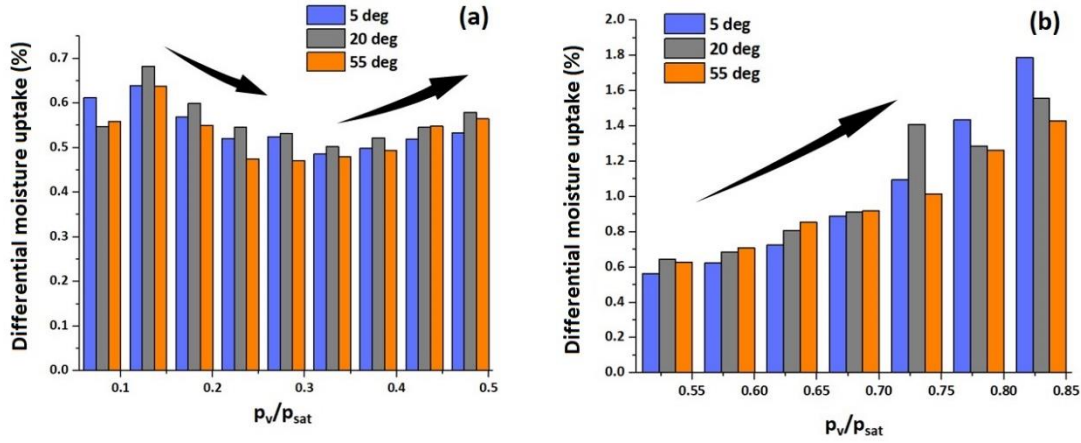
Figure 6.2: Trend of the differential moisture uptake as a function of p_v/p_{sat} in the range (a) 0.08-0.48 and (b) 0.53-0.83 p_v/p_{sat}.

In case of C-S-H, at initial p_v/p_{sat} the water molecules get adsorbed on the interlayer spaces (micropores) which has a higher adsorption potential as the opposite walls overlaps (see chapter 2, section 2.3.1). This explains the increase in the differential moisture uptake up to 0.13 p_v/p_{sat} . When the p_v/p_{sat} is further increased (till 033-0.38 p_v/p_{sat}), the differential moisture uptake decreases. This can be explained by the attractive forces/formation of the water bridges as indicated by green dotted lines in figure 6.3 (b) which will restrict the microstrutural changes by decreasing the differential moisture uptake. Upon further increasing the p_v/p_{sat}, differential moisture uptake increase as well, possibly at the expense of microstructural changes.
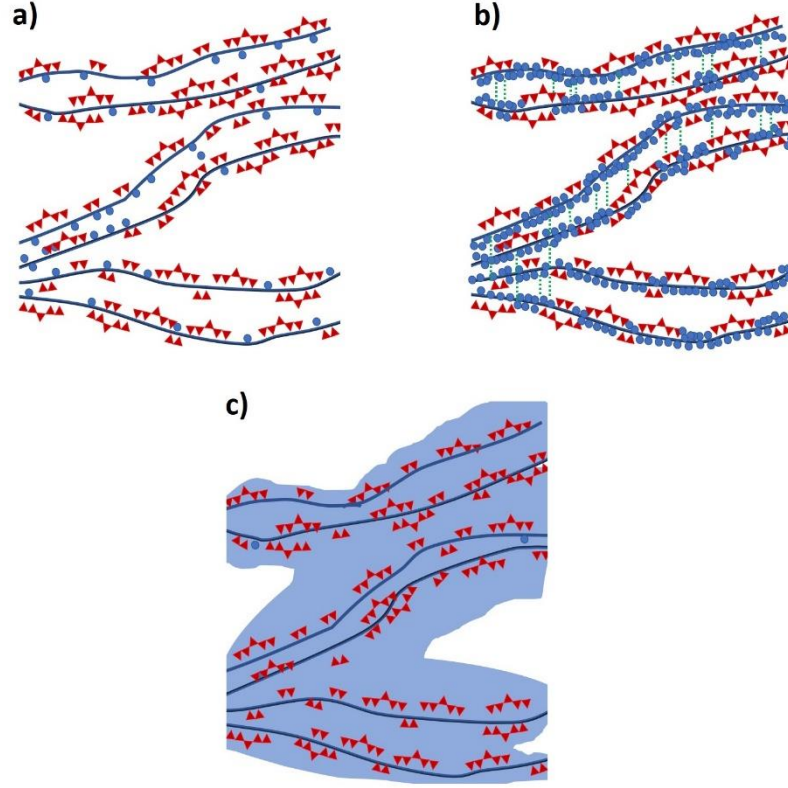
Figure 6.3: Moisture absorption at lower p_v/p_{sat} (till 0.18) (b) as the p_v/p_{sat} increases the differential moisture uptake may decrease because of the attractive surface forces/ briding of the water molecules (as indicated green dotted lines) (c) Further increase in the p_v/p_{sat} results in the microstructural changes and increases the differential moisture uptake.

This behaviour can also be explained using the concept of disjoining pressure. The thermodynamic parameter disjoining pressure (or solvation pressure) Π was initially proposed by Derjaguin and Kusakov[132]. Π physically corresponds to the pressure difference between the pore pressure that acts locally on the surface of the pore walls and the bulk liquid pressure that is in equilibrium with the pore. It is usually expressed as a function of the surface excess concentration (Γ) or the thickness of the film (t_f), and therefore denoted as $\Pi(\Gamma)$ or $\Pi(t_f)$, respectively.

By converting the isotherm into excess surface work (ESW) plot, as introduced by Adolph and Setzer, the explanation becomes a lot simpler[133,134]. The concept of ESW is also based on disjoining pressure. According to this concept, assuming that the absorption is taking place in an open system, a thermal

equilibrium is established if the chemical potential of water in pore μ_w^{liq} with pressure P is equal to the chemical potential of the vapour μ_w^{vap} with pressure p_v.

$$\mu_w^{\text{liq}}(P, T) = \mu_w^{vap}(p_v, T) \tag{6.2}$$

From integrating the Gibbs-Duhem equation, we get

$$\mu_w^{\text{liq}}(P, T) = \mu_o(T) + v_m(P - p_{sat}) \tag{6.3}$$

Where $\mu_o(T)$ is the reference chemical potential of the bulk liquid in equilibrium with the vapour and v_m is the molar volume of liquid water at temperature T.

Using Kelvin equation, the difference in the chemical potential $\Delta\mu$ can be given as:

$$\Delta\mu = RT \, ln\left(\frac{p_v}{p_{sat}}\right) \tag{6.4}$$

R: Universal gas constant.

As derived in [133], $\Delta\mu\Gamma$ can be considered equivalent to Πt and the parameter can be termed as excess surface work Φ such that

$$\Phi = : \Delta\mu\Gamma = : \Pi t \tag{6.5}$$

Physically, ESW can be considered equivalent to the sum of surface free energy and the isothermal work of sorption. ESW results from the counteracting process between the surface free energy and the work of sorption. Surface free energy is dependent on the intermolecular interactions at an interface such as London dispersive force, Debye inductive force, hydrogen bonding among others. [131]. While the work of sorption corresponds to the microtructural changes induced due to water sorption. In the lower p_v/p_{sat} regime, the surface free energy dominates whereas at higher sorption capacities the work of sorption is more relevant. Upon balancing these two forces, a minimum can be observed if Φ is plotted as a function of $\Delta\mu$, Γ, or p_v/p_{sat}. Figure 6.4 shows the excess surface work for samples cured at 5, 20, and 55 °C as a function of change in chemical potential and p_v/p_{sat} .
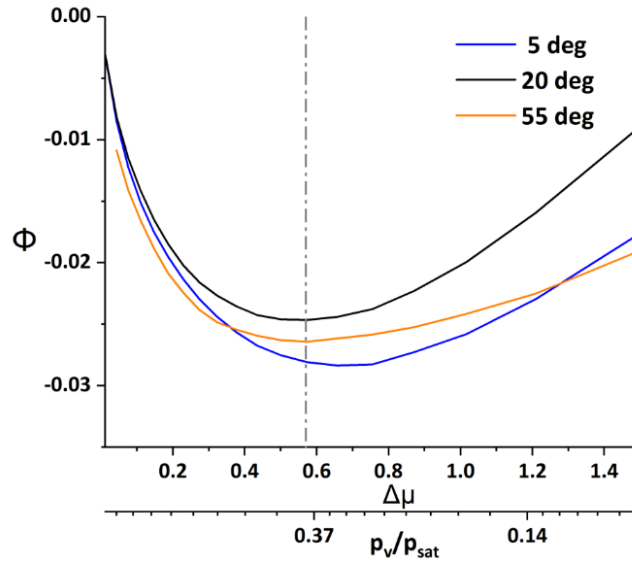
Figure 6.4: Excess surface work Φ as a function of difference in chemical potential $\Delta\mu$ and p_v/p_{sat}.

It is interesting that for all the samples this minimum was found to be at around 0.33- 0.38 p_v/p_{sat}, which is the p_v/p_{sat} at which the differential moisture uptake (%) starts increasing (see figure 6.2) as p_v/p_{sat} increases. This explanation is also comparable to the recent model for sorption hysteresis in which the ESW minimum can be attributed to the balance of elastic free energy and adhesion energy[135].

Bazant and co-workers used the disjoining pressure to explain the concept of multilayer hindered adsorption[47][136]. In nanoporous materials, if p_v/p_{sat} exceeds the value corresponding to complete filling, the adsorption layer is hindered from developing its full thickness. The area of multimolecular hindered adsorbed layer increases with increasing p_v/p_{sat} because of which the area for unhindered adsorption layers would decrease. This could also result in non-monotonic behaviour of the differential moisture uptake (%) in the lower RH regime. Nevertheless, any explanations concerning the disappearance of hindered sorption (such as at sufficiently high p_v/p_{sat}) were not reported.

To further understand the role of surface energy and work of sorption from the ESW model, several scanning isotherms were acquired on the samples cured at 55 °C as shown in figure 6.5.
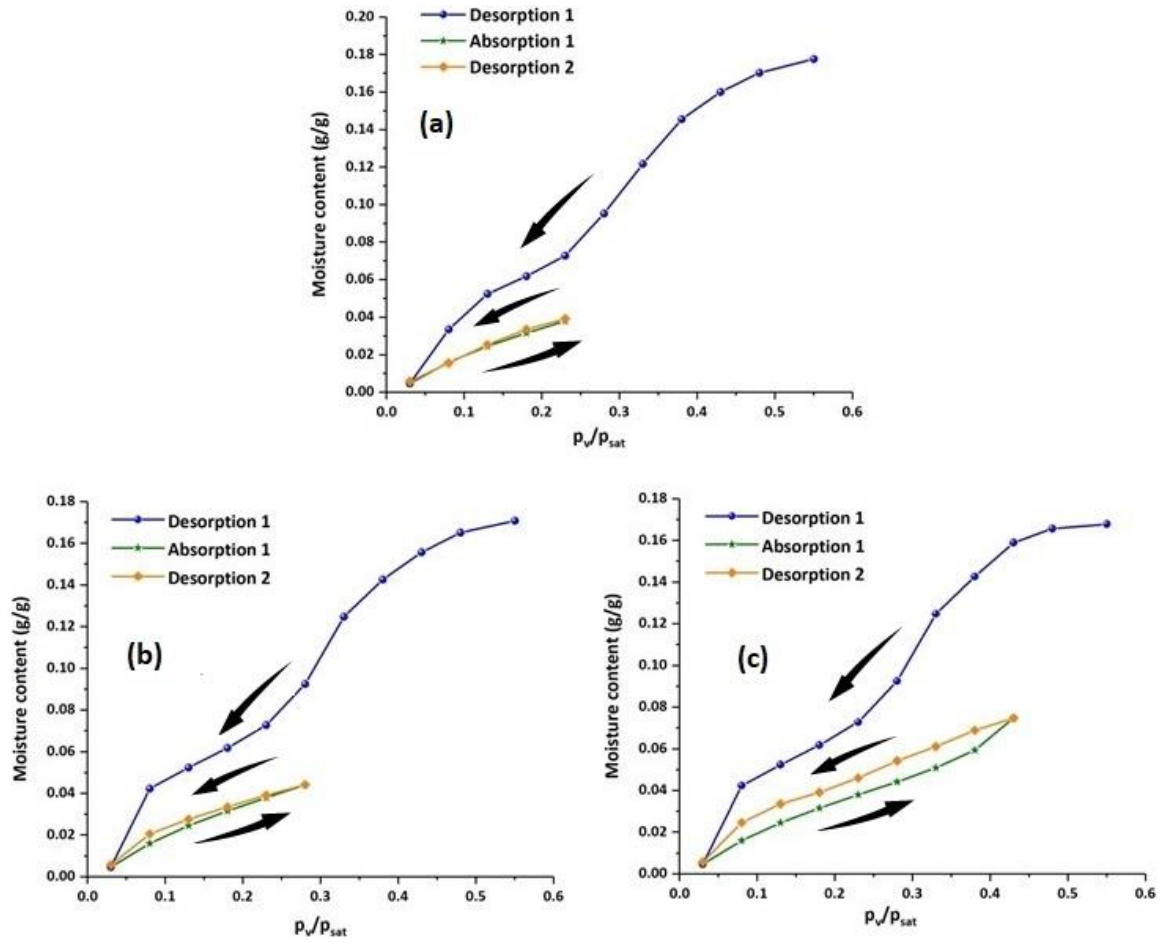
Figure 6.5: Scanning isotherms corresponding to (a) desorption 1 (0.53-0.03 p_v/p_{sat}) → absorption 1 (0.03-0.23 p_v/p_{sat}) → desorption 2 (0.23-0.03 p_v/p_{sat}). (b) Desorption 1 (0.53-0.03 p_v/p_{sat}) → absorption 1 (0.03-0.28 p_v/p_{sat}) → desorption 2 (0.28-0.03 p_v/p_{sat}). (c) Desorption 1 (0.53-0.03 p_v/p_{sat}) → absorption 1 (0.03-0.43 p_v/p_{sat}) → desorption 2 (0.43-0.03 p_v/p_{sat}).

As shown in figure 6.5 (a), if subjected to stepwise absorption till 0.23 p_v/p_{sat} and dried back to 0.03p_v/p_{sat}, the dried sample showed almost no hysteresis between absorption 1 and desorption 2. Similarly, in figure 6.5(b) up to 0.28 p_v/p_{sat} again no hysteresis is observed between absorption 1 and desorption 2. However, if the absorption if up to 0.43 p_v/p_{sat} after desorption 1 and dried back again (desorption 2), the hysteresis between absorption 1 and desorption 2 is significant. The isotherms clearly show that the microstructurural changes that induce hysteresis only occurs after the minimum of ESW is reached and the work of sorption is greater than the surface free energy

6.3.2 Static sorption analysis

Figure 6.6 (a) shows the sorption isotherms acquired on samples cured at 5, 20, and 55°C using the static desiccator-based method. Figure 6.6 (b) shows the moisture absorption kinetics for the samples cured at 55° C. The major difference between the long- and short-term sorption isotherm is that the final moisture uptake (%) does not decrease as p_v/p_{sat} increases. However, mass loss after the initial gain is observed with the time, particularly at 0.11, 0.33, and 0.45 p_v/p_{sat}.

This could be explained by the difference in equilibrium which results from the difference in sample size. In the dynamic sorption tests, owing to a considerably
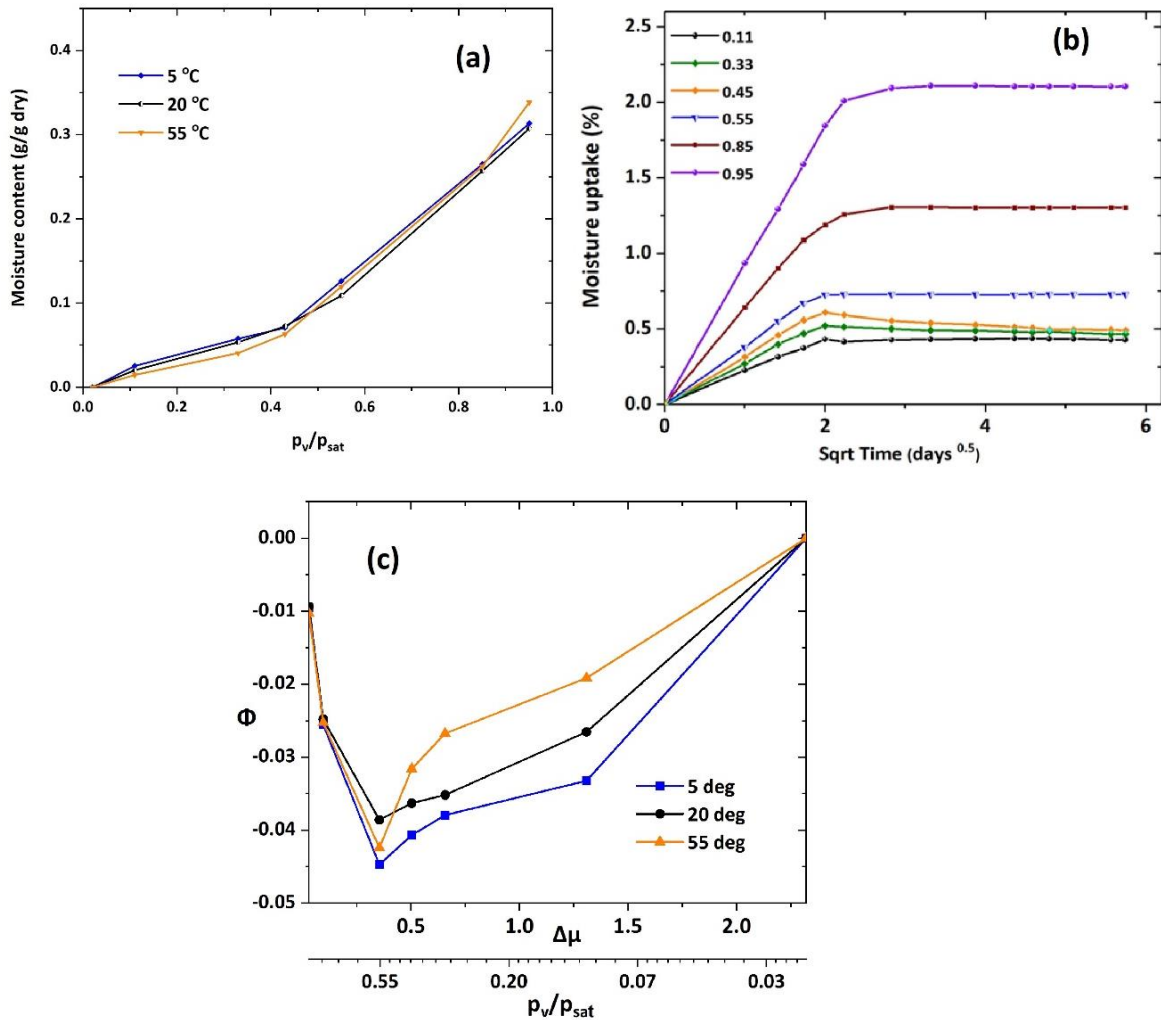
Figure 6.6: (a) Absorption isotherms for samples cured at 5, 20, and 55 °C obtained using the static tests. (b) Moisture absorption profiles for the sample cured at 55 °C at various p_v/p_{sat} values. (c) ESW representation of the isotherms as function of $\Delta\mu$ and p_v/p_{sat}.

smaller sample size (in the order of mg) and more exposed surface area, the diffusion of water throughout the sample volume is faster. However, in static tests with a relatively larger sample (in the order of grams), the moisture uptake is initially governed by interhydrates and capillary pores (or mesopores and macropores). Thereafter, the redistribution of the water occurs in the finer pores. The initial uptake and the distribution of water into the finer pores has also been reported by McDonald and co-workers using ^{1}H NMR relaxometry. The authors observed that the water content first quickly increases in capillary and interhydrates pores. However, it decreased afterwards owing to the redistribution of water in the finer pores[137]. As the system minimizes ESW prior to microstructural changes, this moisture loss is observed after the water redistribution. From the static tests, this minimum was observed at 0.54 p_v/p_{sat} for the sample cured at 55° C, as shown in figure 6.5 (c).

6.3.3 On analysing water absorption isotherms for microstructural assessments

Water vapour absorption isotherms are routinely used to obtain information on the microstructure such as pore size distributions and specific surface area[12,58,138]. Often, the theories and equations used for analysing the gas sorption isotherms are also directly used to interpret the water sorption behaviour. For example, BET equation and its extensions are frequently used to derive the monolayer capacity which is then used for calculating the specific surface area[51,139–141]. However, there is a striking difference in assumptions made in BET and the practical sorption process, particularly for a polar molecule like water as adsorbate and C-S-H as adsorbent. It has been observed that water sorption can lower the glass transition temperature, act as a plasticizer, and affect the number of physical and chemical properties in a variety of amorphous adsorbents[142–145].

In this study, to fully investigate the effects originating from the interaction of water with adsorbents, we also acquired sorption isotherms on a well-known mesoporous material MCM-41 (hexagonal type, SiO_2). This material is known to have a simple structure (well-defined pore shape, narrow pore distribution, and negligible pore networking). It also has good thermal and mechanical stability and, most importantly, deprotonated silanol groups that are also known to be present on the surface of C-S-H[146]. The absorption isotherms were acquired on dry (as-obtained) sample as well as the sample saturated with water and that has been dried again after wetting. This wet sample was prepared by placing a few drops of water on MCM-41 and gently mixing it followed by drying at 0 p_v/p_{sat} till the desired equilibrium was achieved.
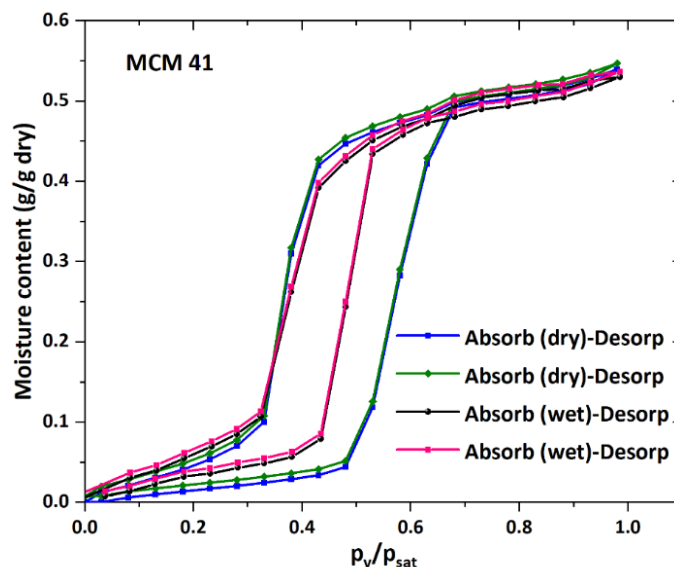
Figure 6.7: Absorption-desorption behaviour of MCM 41 starting from a wet (black and pink colour) and dry (blue and green colour) state.

Figure 6.7 shows the sorption isotherms for the same sample but with a different starting state. The absorption→desorption isotherms of the dry samples have been indicated by blue and green colour. The absorption→desorption isotherms of the re-dried sample after wetting have been indicated in black and pink colour. The significant difference between the absorption isotherms owing to the change in the starting state of the material occurs because of the hydroxylation of silanol groups. Similar results have been reported by Kittaka *et al.* where a

considerable difference has been observed in the first and second absorption isotherms and the hydroxylation was confirmed by FTIR analysis. The absorption isotherms in subsequent cycles were found to be the same[147].

Apart from surface interactions and forces acting between the surface of C-S-H (such as long-range double-layer repulsion, short-range hydration force, and steric repulsion etc.), the biggest challenge is the dynamic microstructural changes /porosity relaxation which occurs at higher RH. Small-angle scattering of X rays (SAXS) or neutron (SANS) are capable of obtaining the specific surface area in both saturated and dry states. It has been observed that the specific surface area is 3-4 times higher in a saturated state than in a dry state [52,148–150]. Many authors agree with the interlayer water absorption isotherm by Feldman and Sereda which suggests that water enters the interlayer throughout the entire p_v/p_{sat} regime[29,40,55,135,151]. Therefore, if the BET equations and its extensions are used to evaluate the microstructure (even ignoring the erroneous assumptions), the obtained information reflects the microstructure that neither corresponds to the dry state nor the saturated state, but is rather dynamic. Furthermore, it has long been pointed out that if micropores are present in the material, the monolayer capacity loses its physical meaning and rather should be interpreted as strong retention capacity of the adsorbate[152], which again puts a limitation on accurate determination of specific surface area. Therefore, the theories and models that are implemented to obtain information on the microstructure from the absorption isotherms must consider the challenges associated with the effect of surface interactions in the lower p_v/p_{sat} regime and microstuructural rearrangements at the higher p_v/p_{sat} regime.

6.3.4 Sorption with isopropanol

Figure 6.8 (a) shows the adsorption isotherm acquired on the sample cured at 55°C using isopropanol as adsorptive. As shown in figure 6.7 (b), very strong adsorption was observed as the sample was exposed to 0.03 p_v/p_{sat} suggesting strong surface interaction (perhaps chemisorption)[70,153,154]. Thereafter, the differential uptake first decreased with an increase in p_v/p_{sat} after which it increased again.
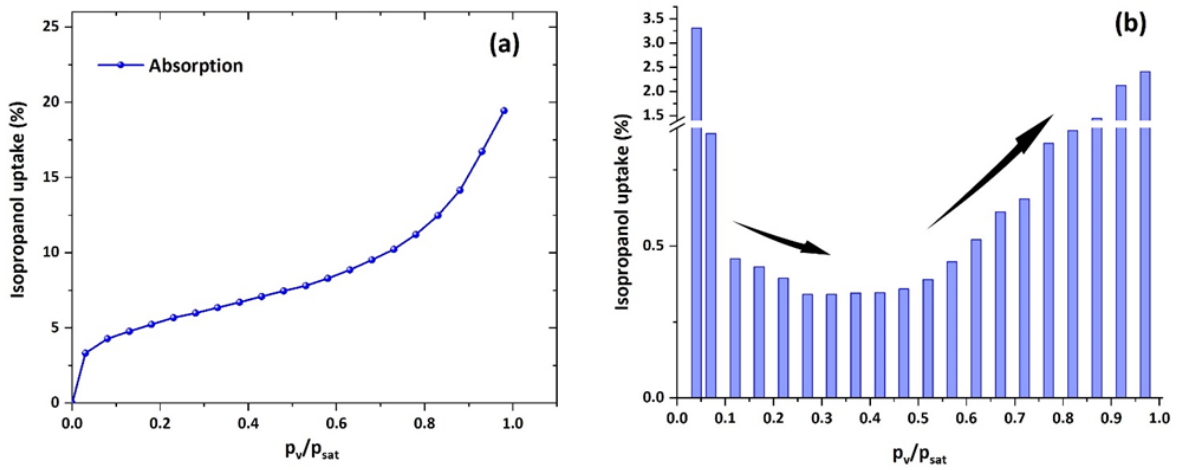
Figure 6.8: Absorption isotherm on the sample cured at 55 °C using isopropanol as adsorptive. (b) Isopropanol uptake (%) as a function of p_v/p_{sat}.

The adsorption behaviour was further analysed in detail by obtaining the sorption profile for each p_v/p_{sat} step. The same has been shown in figure 6.8 (a) and (b) which corresponds to the kinetics in low (0.03-0.33) and high (0.43-0.98) p_v/p_{sat} regime, respectively. The sorption was found to be very unstable which could be attributed to the fast evaporation of isopropanol thus, making it difficult to maintaining the desired p_v/p_{sat}. Furthermore as shown in the figure 6.8 (b) and 6.9 (c), the final differential utake at 0.03 p_v/p_{sat} is already higher than than that at 0.98 p_v/p_{sat}. This could indicate that the sorption of isopropanol is already completed at 0.03p_v/p_{sat} Thereafter, possibly there is no sorption, but accumulation of the isopropanol at the surface of the sample.

The isotherm was converted into an ESW plot as shown in figure 6.8 (c). A typical U-shaped curve was not obtained in the ESW plot, and the minimum, therefore, has not been determined. Nonetheless, no inferences on the microstructural changes can be drawn from this analysis and more research is needed to understand isopropanol sorption behaviour of cementitious materials.
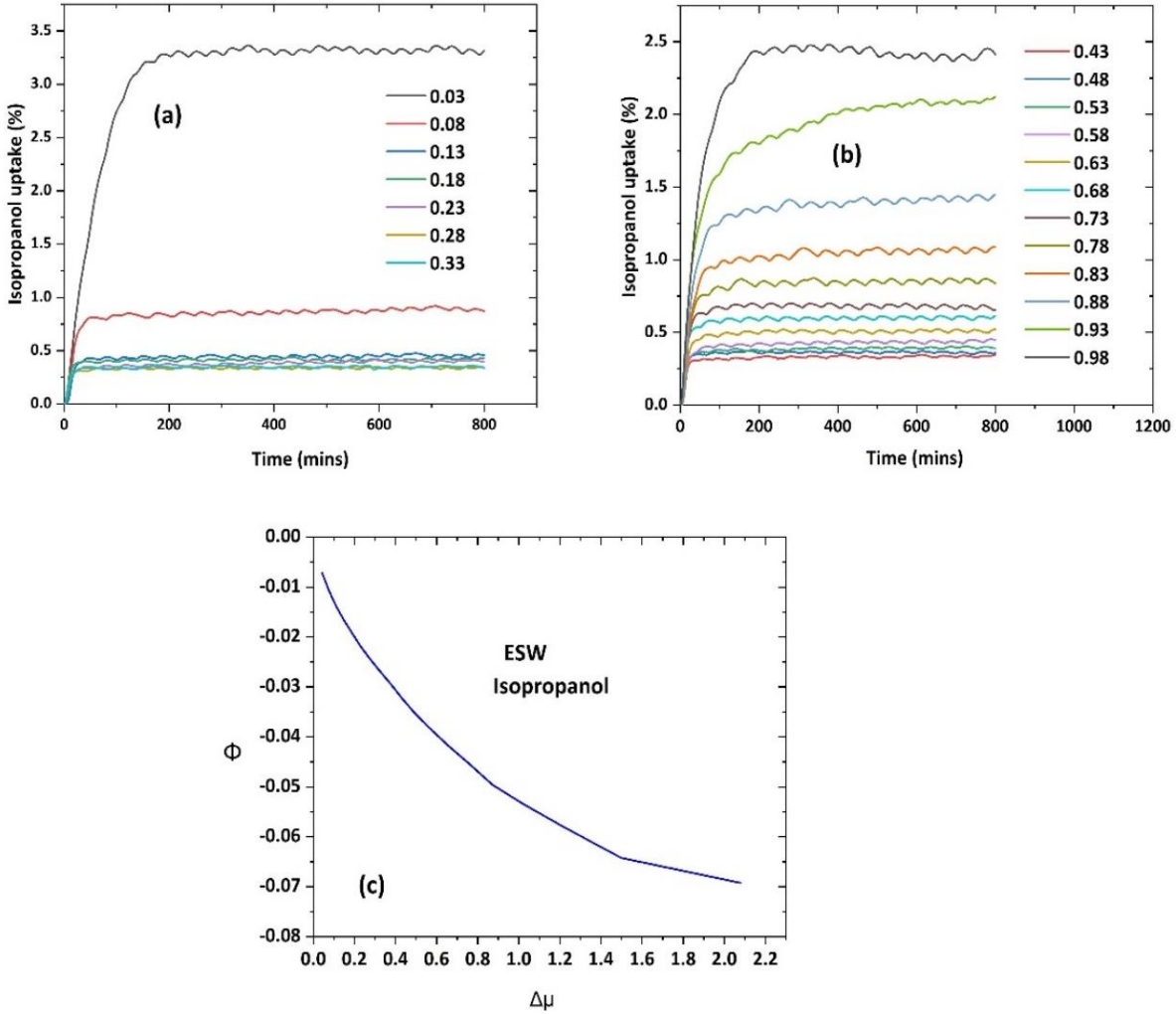
Figure 6.9: Sorption kinetics for the sample cured at 55 °C with ISOPROPANOL as adsorptive in (a) low 0.03-0.33 p_v/p_{sat} and (b) high 0.43-0.98 p_v/p_{sat} sorption regime . ESW representation of the isotherm the absorption isotherm shown in figure 6.7(a).

6.4 Conclusions

In this paper, we examine the water absorption behaviour on samples with maximized C-S-H content. The dynamic vapour sorption analysis on various samples showed that the differential moisture uptake (%) increases (up to $0.18 p_v/p_{sat}$) then decreases (till 0.33-0.38 p_v/p_{sat}) before increasing again. This behaviour has been explained by converting the absorption isotherms into an ESW plot. According to the ESW concept, the surface free energy governs the sorption behaviour in the lower p_v/p_{sat} regime (before the ESW minimum) whereas at higher sorption capacities (after the ESW minimum) the work of sorption is more significant. The moisture uptake is governed by the interplay of these two forces and a minimum in the ESW plot is observed when these forces are balanced. Dynamic vapour sorption analysis revealed this minimum to be around 0.33-0.38 p_v/p_{sat} for all samples considered in this study. Investigating several scanning isotherms also suggest that microstructural changes that results in hysteresis occur after the ESW minimum is reached.

The static tests revealed the ESW minima to be at 0.54 p_v/p_{sat}. To understand the difference in ESW minimum from dynamic and static tests, more research is needed to identify the influence of spatial and temporal structural evolution of the C-S-H with respect to time scales and sample size. Additionally, absorption isotherms of MCM-41 showed the influence of surface interaction/adsorbent history on water absorption isotherms. Finally, ESW plot of isopropanol absorption isotherm showed no minimum, nonetheless more investigations are required to draw any conclusions from these sorption isotherms.

Acknowledgements

Chapter 7   Conclusion and future work

In this thesis, the water desorption and absorption behaviour of the samples with maximized C-S-H content was investigated.

7.1   Main findings

7.1.1 Understanding factors affecting the desorption of cementitious materials

- o A detailed investigation of water vapour desorption isotherms helped to understanding the role of cavitation in drying cementitious materials. It was observed that heterogeneous cavitation occurs around 0.8 p_v/p_{sat} (25-30 MPa) owing to the presence of pre-existing bubbles and surface imperfections among other factors. As p_v/p_{sat} decreases, the connected porosity is dried out. Thereafter, at around 0.3 p_v/p_{sat} there is a homogeneous cavitation event, which should be occuring in pores isolated from the rest of the porosity. The volume balance analysis indicated that homogeneous cavitation probably occurs in the gel pores of the inner product.

- o Classical nucleation theory helped to identify the parameters that influence cavitation pressure. Surface tension at the liquid-vapour interface was identified as the most important parameter. If the surface tension is reduced by introducing shrinkage reducing admixtures or by increasing sorption temperature, the homogeneous cavitation was found to occur at lower capillary pressures.

- o The results indicate that it is important to consider the peculiarities of water at nanoscale when considered as an adsorbate molecule for investigating the microstructure of cementitious materials using desorption isotherm.

7.1.2 Microstructural evaluations using desorption analysis

o Analysis of the desorption isotherms was carried out to study the effect of hydration temperature (5, 20, 40, and 55 °C) on the microstructure of the samples with maximized C-S-H content. Mass balance calculations were made using multiple techniques including XRD, SEM, and ^{1}H NMR. The amount of capillary and gel water content obtained from the desorption isotherms were found to be in good agreement with those obtained from the mass balance calculations. Further, the amount of gel pores that were emptied after homogeneous cavitation was found to decrease as the curing temperature increased. This is consistent with the trend of increase in the bulk density of C-S-H as the temperature increases, as determined by other techniques.

o The moisture desorption behaviour of the C-S-H samples synthesized using three different techniques was compared. The C-S-H synthesized using double decomposition and dropwise precipitation method did not show features of a porous microstructure irrespective of the solvent used for washing the samples or the Ca/Si ratio. The C-S-H prepared using belite hydration technique with added silica fume showed finer pore structure and more gel water content upon analyzing through desorption isotherms. The desorption isotherms of C-S-H samples prepared using white cement and silica fume at different curing temperatures showed coarsening of the microstructure for samples cured at higher temperatures (40 and 55 °C). No direct relationship was observed between the Ca/Si ratio and desorption isotherms of C-S-H samples.

7.1.3 Insights from the absorption isotherms

o The non-monotonic behaviour of the differential moisture uptake (%) in dynamic absorption isotherms is explained by converting the absorption isotherms into ESW plots. In the lower p_v/p_{sat} regime, the

surface free energy dominates, whereas at higher sorption capacities the work of sorption is more significant. The moisture uptake is governed by the interplay of these two forces and a minimum in the ESW plot is observed upon balancing these forces. Analysis of scanning isotherms indicated that microstructural changes occurs after the ESW minimum has been reached.

o The static sorption test on the same samples indicated a different ESW minimum at 0.54 p_v/p_{sat} as compared to 0.38 p_v/p_{sat}, using dynamic sorption tests.

o The influence of surface interaction owing to different starting states (adsorbent history) on water absorption isotherms was showed by the sorption isotherms of MCM-41. The sorption behaviour of isopropanol was found to be very different from that of water.

7.2 Future work

Acoustic emissions (AE) could be used to detect homogeneous and heterogeneous cavitation events. AE are conventionally used to detect crack formation and damage in cementitious materials that occurs during loading, freeze-thaw cycles, and uniaxial compression etc. [155–158]. Lura *et al.* used AE to indicate the time zero which corresponds to the liquid-solid transition takes place in a cement paste. Gault and co-workers extensively investigated the AE of calcium aluminate cement at an early age. The authors reported that most of the AE events occur during the first 3 to 6 h of mixing and the central frequency of waveform varies from 120 kHz to 170 kHz [159]. A Fourier transform of the AE waveforms revealed that the signal may be attributed to the emptying of capillary pores[160]. Investigations made by Gault and co-workers and Lura *et al.*, could also indicate the AE signal can be attributed to the heterogeneous cavitation occurring at 25-30 MPa. As the samples harden and the p_v/p_{sat} decreases to 0.85-0.80, the heterogeneous cavitation would already lead to emptying of the capillary pores. AE experiments can be carried out to investigate the homogeneous cavitation events as well.

In-situ FTIR study as a function of p_v/p_{sat} can help in understanding the role of surface interaction of water with C-S-H. Some preliminary investigations were

made in this direction. As shown by figure 7.1 (a-c), a small custom-built pilot setup was developed in which the desired p_v/p_{sat} is achieved by bubbling the water with nitrogen gas. Mass flow controllers would facilitate better control of p_v/p_{sat}. A thin slice of cement sample is placed on the attenuated total reflection (ATR) crystal and
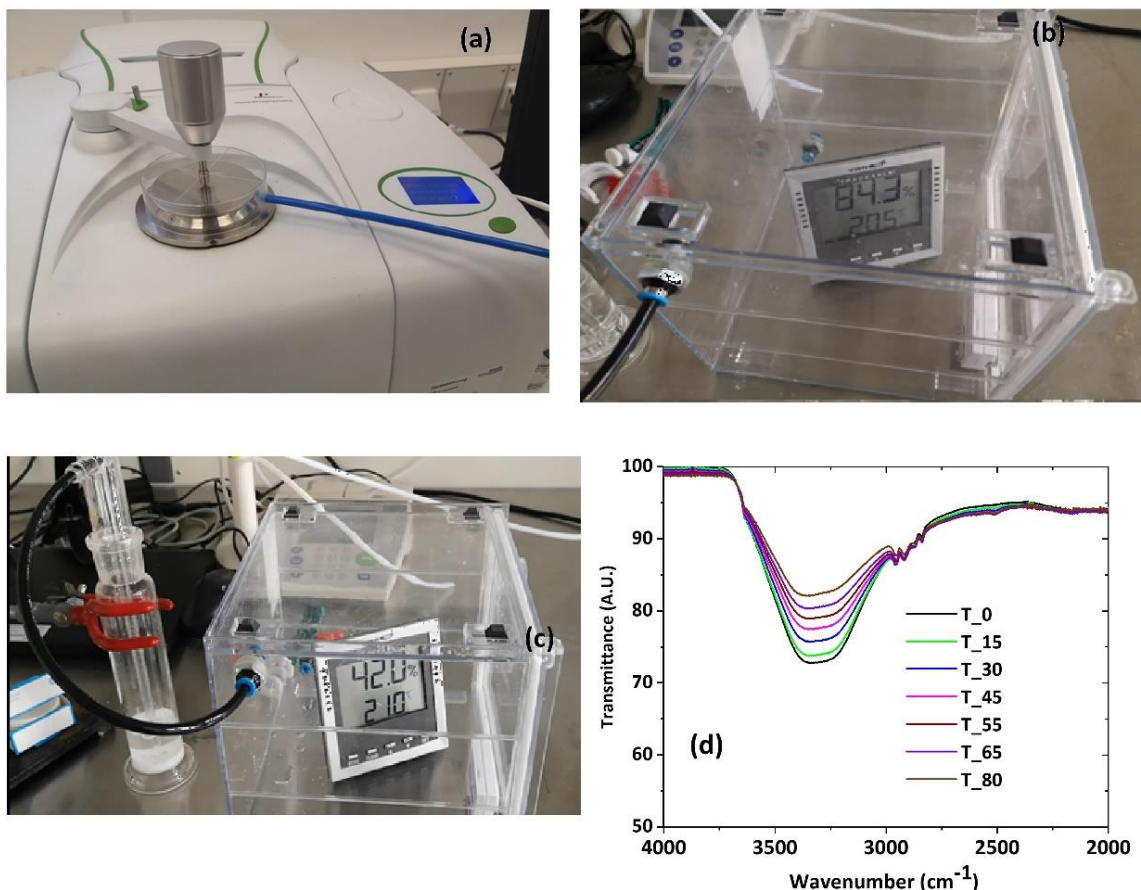
Figure 7.1: (A) An air tight chamber where the sample is kept on the ATR crystal and the pressure is applied to ensure enough contact between the crystal and the sample. (b) and (c) Examples of RH obtained using bubbling of nitrogen gas over water. (d) The vibration spectra as the RH is changed subsequently (Note: preliminary results, RH has not been carefully monitored).

the pressure is applied with the hand clutch till sufficient contact is made with the diamond.

As shown in figure 7.1 (d), the stretching bands obtained between 3000 and 3800 cm^{-1} as a function of p_v/p_{sat} can be deconvoluted using the bands associated with coordinated water[161,162]. A detailed description of this procedure can be found in the study carried out by Baumgartner *et al.* [163]. The authors studied the

pore size-dependent structure of water in mesoporous silica films from water sorption using ATR-FTIR spectroscopy. Such investigations could also help in understanding the reasons for low-pressure hysteresis particularly if the nature of confined water is different during absorption than desorption.

For understanding the difference in ESW minimum from dynamic and static tests, more research is needed to identify the influence of spatial and temporal microstructural evolution of the C-S-H with respect to time scales and sample size.

Finally, the nanofluidic systems in which the fluids are studied under confinement at the nanoscale could also help in answering some of the open questions. At the nano level, the fluid behaviour deviates from the continuum assumptions. The surface forces including strong ion-covalent attraction, Van der Waals force, long-range double-layer repulsion, hydration forces, and steric repulsion etc. governs the fluid behaviour[164–166]. These forces lead to a spectrum of anomalous transport and thermodynamic phenomena concerning fluid transport, condensation and vaporization, as shown in figure 7.2[167].
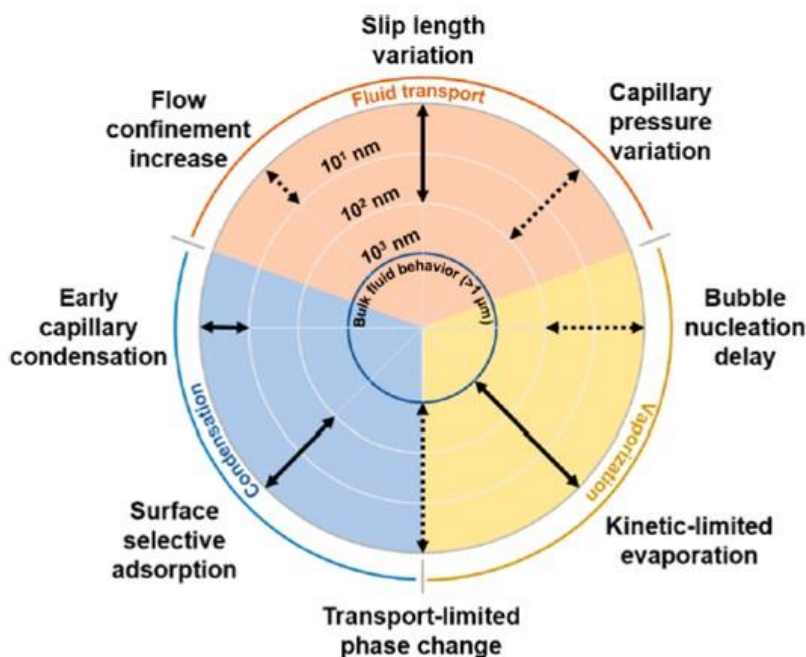
Figure 7.2: Key anomalies of nanoscale fluid behaviours. The double-sided arrows indicate the dimensions of interest for different anomalies and whether they promote (solid) or impede (dashed) fluid behaviours compared with classical bulk fluid theories.

Bibliography

[1]   J.J. Beaudoin, V.S. Ramachandran, R.F. Feldman, Interaction of chloride and CSH, Cem. Concr. Res. (1990). https://doi.org/10.1016/0008-8846(90)90049-4.

[2]   K. De Weerdt, B. Lothenbach, M.R. Geiker, Comparing chloride ingress from seawater and NaCl solution in Portland cement mortar, Cem. Concr. Res. (2019). https://doi.org/10.1016/j.cemconres.2018.09.014.

[3]   S. von Greve-Dierfeld, B. Lothenbach, A. Vollpracht, B. Wu, B. Huet, C. Andrade, C. Medina, C. Thiel, E. Gruyaert, H. Vanoutrive, I.F. Saéz del Bosque, I. Ignjatovic, J. Elsen, J.L. Provis, K. Scrivener, K.C. Thienel, K. Sideris, M. Zajac, N. Alderete, Ö. Cizer, P. Van den Heede, R.D. Hooton, S. Kamali-Bernard, S.A. Bernal, Z. Zhao, Z. Shi, N. De Belie, Understanding the carbonation of concrete with supplementary cementitious materials: a critical review by RILEM TC 281-CCC, Mater. Struct. Constr. (2020). https://doi.org/10.1617/s11527-020-01558-w.

[4]   S. Steiner, B. Lothenbach, T. Proske, A. Borgschulte, F. Winnefeld, Effect of relative humidity on the carbonation rate of portlandite, calcium silicate hydrates and ettringite, Cem. Concr. Res. (2020). https://doi.org/10.1016/j.cemconres.2020.106116.

[5]   V. Dutzer, W. Dridi, S. Poyet, P. Le Bescop, X. Bourbon, The link between gas diffusion and carbonation in hardened cement pastes, Cem. Concr. Res. (2019). https://doi.org/10.1016/j.cemconres.2019.105795.

[6]   H. Wierig, Longtime studies on the carbonation of concrete under normal outdoor exposure, Proc. RILEM, Hann. Univ. (1984).

[7]   K. Van Balen, D. Van Gemert, Modelling lime mortar carbonation, Mater. Struct. (1994). https://doi.org/10.1007/BF02473442.

[8]   M. Thiery, V. Baroghel-Bouny, G. Villain, P. Dangla, Numerical modeling of concrete carbonation based on durability indicators, in: Am. Concr. Institute, ACI Spec. Publ., 2006.

[9]   S.K. Roy, K.B. Poh, D.O. Northwood, Durability of concrete - Accelerated carbonation and weathering studies, Build. Environ. (1999). https://doi.org/10.1016/S0360-1323(98)00042-0.

[10]   D. Gawin, F. Pesavento, B.A. Schrefler, Hygro-thermo-chemo-mechanical modelling of concrete at early ages and beyond. Part II: Shrinkage and creep of concrete, Int. J. Numer. Methods Eng. (2006). https://doi.org/10.1002/nme.1636.

[11]   C.E. Majorana, Mathematical modelling of creep and shrinkage of concrete, edited by Z. P. Bazant, Wiley, Chichester, 1988. ISBN 0 471920576, Int. J. Numer. Methods Eng. (1990). https://doi.org/10.1002/nme.1620290214.

[12]   V. Baroghel-Bouny, Water vapour sorption experiments on hardened cementitious materials. Part I: Essential tool for analysis of hygral behaviour and its relation to pore structure, Cem. Concr. Res. (2007). https://doi.org/10.1016/j.cemconres.2006.11.019.

[13]   J.M. de Burgh, S.J. Foster, Influence of temperature on water vapour sorption isotherms and kinetics of hardened cement paste and concrete, Cem. Concr. Res. (2017). https://doi.org/10.1016/j.cemconres.2016.11.006.

[14]   T. Powers, T. Brownyard, Studies of hardened paste by means of specific volume measurements, J. Am. Concr. Inst. (1947). https://doi.org/10.14359/8745.

[15]   H.F.W. Taylor, Cement chemistry, 1997. https://doi.org/10.1680/cc.25929.

[16]   M. Alexander, A. Bentur, S. Mindess, Durability of concrete: Design and construction, 2017. https://doi.org/10.1201/9781315118413.

[17]   and D.D. S. Mindess, J.F. Young, Prentice Hall, Pearson Education, 2nd edition, 2003., Concrete. (n.d.).

[18]   Handbook of Porous Solids, 2002. https://doi.org/10.1002/9783527618286.

[19]   P.C. Hewlett, M. Liska, Lea's chemistry of cement and concrete, 2019. https://doi.org/10.1016/C2013-0-19325-7.

[20]   M. Wu, Using low temperature calorimetry and moisture fixation method to study the pore structure of cement based materials, Technical University of Denmark, 2014.

[21]   T.C. Powers, T.L. Brownyard, Studies of the Physical Properties of Hardened Portland Cement Paste Part 9. General Summary of Findings on the Properties of Hardened portland Cement Paste, J. Am. Concr. Inst. (1947).

[22]   R.F. Feldman, P.J. Sereda, A model for hydrated Portland cement paste as deduced from sorption-length change and mechanical properties, Matériaux Constr. (1968). https://doi.org/10.1007/BF02473639.

[23]   P.J. SEREDA, R.F. Feldman, V.S. Ramachandran, Structure formation and development in hardened cement pastes, in: 7th Int. Congr. Chem. Cem. Vol. 1, 1980.

[24] P.J. Sereda, R.F. Feldman, E.G. Swenson, Effect of sorbed water on some mechanical properties of hydrated Portland cement pastes and compacts, Highw. Res. Board …. (1966).

[25] F.H. WITTMANN, Interaction of Hardened Cement Paste and Water, J. Am. Ceram. Soc. (1973). https://doi.org/10.1111/j.1151-2916.1973.tb12711.x.

[26] M. Wyrzykowski, P.J. McDonald, K.L. Scrivener, P. Lura, Water Redistribution within the Microstructure of Cementitious Materials due to Temperature Changes Studied with 1H NMR, J. Phys. Chem. C. (2017). https://doi.org/10.1021/acs.jpcc.7b08141.

[27] H.M. Jennings, P.D. Tennis, Model for the Developing Microstructure in Portland Cement Pastes, J. Am. Ceram. Soc. (1994). https://doi.org/10.1111/j.1151-2916.1994.tb04565.x.

[28] P.D. Tennis, H.M. Jennings, Model for two types of calcium silicate hydrate in the microstructure of Portland cement pastes, Cem. Concr. Res. (2000). https://doi.org/10.1016/S0008-8846(00)00257-X.

[29] H.M. Jennings, Refinements to colloid model of C-S-H in cement: CM-II, Cem. Concr. Res. (2008). https://doi.org/10.1016/j.cemconres.2007.10.006.

[30] J.J. Thomas, A.J. Allen, H.M. Jennings, Structural changes to the calcium-silicate-hydrate gel phase of hydrated cement with age, drying, and resaturation, J. Am. Ceram. Soc. (2008). https://doi.org/10.1111/j.1551-2916.2008.02636.x.

[31] A. Kunhi Mohamed, S.C. Parker, P. Bowen, S. Galmarini, An atomistic building block description of C-S-H - Towards a realistic C-S-H model, Cem. Concr. Res. (2018). https://doi.org/10.1016/j.cemconres.2018.01.007.

[32] A.C.A. MULLER, Characterization of porosity & C-S-H in cement pastes by 1H NMR, Cem. Concr. Res. (2015). https://doi.org/10.1007/b95236.

[33] M. Wyrzykowski, A.M. Gajewicz-Jaromin, P.J. McDonald, D.J. Dunstan, K.L. Scrivener, P. Lura, Water Redistribution-Microdiffusion in Cement Paste under Mechanical Loading Evidenced by 1H NMR, J. Phys. Chem. C. (2019). https://doi.org/10.1021/acs.jpcc.9b02436.

[34] A.C.A. Muller, K.L. Scrivener, A.M. Gajewicz, P.J. McDonald, Use of bench-top NMR to measure the density, composition and desorption isotherm of C-S-H in cement paste, Microporous Mesoporous Mater. (2013). https://doi.org/10.1016/j.micromeso.2013.01.032.

[35] A. Valori, P.J. McDonald, K.L. Scrivener, The morphology of C-S-H: Lessons from 1H nuclear magnetic resonance relaxometry, Cem. Concr. Res. (2013). https://doi.org/10.1016/j.cemconres.2013.03.011.

[36] P.J. McDonald, V. Rodin, A. Valori, Characterisation of intra- and inter-C-S-H gel pore

water in white cement based on an analysis of NMR signal amplitudes as a function of water content, Cem. Concr. Res. (2010). https://doi.org/10.1016/j.cemconres.2010.08.003.

[37]   J.P. Korb, NMR and nuclear spin relaxation of cement and concrete materials, Curr. Opin. Colloid Interface Sci. (2009). https://doi.org/10.1016/j.cocis.2008.10.004.

[38]   H.M. Jennings, A. Kumar, G. Sant, Quantitative discrimination of the nano-pore-structure of cement paste during drying: New insights from water sorption isotherms, Cem. Concr. Res. (2015). https://doi.org/10.1016/j.cemconres.2015.05.006.

[39]   M. Wu, B. Johannesson, M. Geiker, A study of the water vapor sorption isotherms of hardened cement pastes: Possible pore structure changes at low relative humidity and the impact of temperature on isotherms, Cem. Concr. Res. (2014). https://doi.org/10.1016/j.cemconres.2013.11.008.

[40]   J.M. De Burgh, S.J. Foster, H.R. Valipour, Prediction of water vapour sorption isotherms and microstructure of hardened Portland cement pastes, Cem. Concr. Res. (2016). https://doi.org/10.1016/j.cemconres.2015.11.009.

[41]   L.A.G. Aylmore, Hysteresis in gas sorption isotherms, J. Colloid Interface Sci. (1974). https://doi.org/10.1016/0021-9797(74)90050-2.

[42]   F. Rouquerol, J. Rouquerol, K.S.W. Sing, P. Llewellyn, G. Maurin, Adsorption by powders and porous solids: Principles, Methodology and Applications, 2014.

[43]   T.L. Hill, Thermodynamics of adsorption, Trans. Faraday Soc. (1951). https://doi.org/10.1039/tf9514700376.

[44]   M. Thommes, Physical adsorption characterization of nanoporous materials, Chemie-Ingenieur-Technik. (2010). https://doi.org/10.1002/cite.201000064.

[45]   E. Kierlik, P.A. Monson, M.L. Rosinberg, L. Sarkisov, G. Tarjus, Capillary condensation in disordered porous materials: Hysteresis versus equilibrium behavior, Phys. Rev. Lett. (2001). https://doi.org/10.1103/PhysRevLett.87.055701.

[46]   A. Vishnyakov, A. V. Neimark, Studies of liquid-vapor equilibria, criticality, and spinodal transitions in nanopores by the gauge cell Monte Carlo simulation method, J. Phys. Chem. B. (2001). https://doi.org/10.1021/jp003994o.

[47]   Z.P. Bažant, M.Z. Bazant, Theory of sorption hysteresis in nanoporous solids: Part I: Snap-through instabilities, J. Mech. Phys. Solids. (2012). https://doi.org/10.1016/j.jmps.2012.04.014.

[48]   M.Z. Bazant, Z.P. Bažant, Theory of sorption hysteresis in nanoporous solids: Part II Molecular condensation, J. Mech. Phys. Solids. (2012). https://doi.org/10.1016/j.jmps.2012.04.015.

[49]   H.M. Jennings, J.J. Thomas, J.S. Gevrenov, G. Constantinides, F.J. Ulm, A multi-technique investigation of the nanoporosity of cement paste, Cem. Concr. Res. (2007). https://doi.org/10.1016/j.cemconres.2006.03.021.

[50]   P. Suwanmaneechot, A. Aili, I. Maruyama, Creep behavior of C-S-H under different drying relative humidities: Interpretation of microindentation tests and sorption measurements by multi-scale analysis, Cem. Concr. Res. (2020). https://doi.org/10.1016/j.cemconres.2020.106036.

[51]   D. Snoeck, L.F. Velasco, A. Mignon, S. Van Vlierberghe, P. Dubruel, P. Lodewyckx, N. De Belie, The influence of different drying techniques on the water sorption properties of cement-based materials, Cem. Concr. Res. (2014). https://doi.org/10.1016/j.cemconres.2014.06.009.

[52]   D.N. WINSLOW, S. DIAMOND, Specific Surface of Hardened Portland Cement Paste as Determined by Small-Angle X-Ray Scattering, J. Am. Ceram. Soc. (1974). https://doi.org/10.1111/j.1151-2916.1974.tb10856.x.

[53]   and M.Y. S. Brunay, I. Odler, New Model of Hardened Portland Cement Paste, Hinhw. Res. Rec. 328 (1970) 89-101,105-107.

[54]   I.C. Fita, J.M. Cruz, C. Calvo, L. Soriano, J. Payá, I. Sánchez, Drying-rewetting cycles in ordinary Portland cement mortars investigated by electrical impedance spectroscopy, Constr. Build. Mater. (2018). https://doi.org/10.1016/j.conbuildmat.2018.07.227.

[55]   M.B. Pinson, E. Masoero, P.A. Bonnaud, H. Manzano, Q. Ji, S. Yip, J.J. Thomas, M.Z. Bazant, K.J. Van Vliet, H.M. Jennings, Hysteresis from multiscale porosity: Modeling water sorption and shrinkage in cement paste, Phys. Rev. Appl. (2015). https://doi.org/10.1103/PhysRevApplied.3.064009.

[56]   M. Wu, B. Johannesson, M. Geiker, Application of water vapor sorption measurements for porosity characterization of hardened cement pastes, Constr. Build. Mater. (2014). https://doi.org/10.1016/j.conbuildmat.2014.06.004.

[57]   S. Bahafid, S. Ghabezloo, P. Faure, M. Duc, J. Sulem, Effect of the hydration temperature on the pore structure of cement paste: Experimental investigation and micromechanical modelling, Cem. Concr. Res. (2018). https://doi.org/10.1016/j.cemconres.2018.06.014.

[58]   N. De Belie, J. Kratky, S. Van Vlierberghe, Influence of pozzolans and slag on the microstructure of partially carbonated cement paste by means of water vapour and nitrogen sorption experiments and BET calculations, Cem. Concr. Res. (2010). https://doi.org/10.1016/j.cemconres.2010.08.014.

[59]   A.C.A. MULLER, Characterization of porosity & C-S-H in cement pastes by 1H NMR, Thesis. 52 (2015) 246.

[60]   I. Maruyama, G. Igarashi, Y. Nishioka, Bimodal behavior of C-S-H interpreted from short-term length change and water vapor sorption isotherms of hardened cement paste, Cem. Concr. Res. (2015). https://doi.org/10.1016/j.cemconres.2015.03.010.

[61]   S. Brunauer, R.S. Mikhail, E.E. Bodor, Some remarks about capillary condensation and pore structure analysis, J. Colloid Interface Sci. (1967). https://doi.org/10.1016/0021-9797(67)90041-0.

[62]   A.M. Gajewicz-Jaromin, P.J. McDonald, A.C.A. Muller, K.L. Scrivener, Influence of curing temperature on cement paste microstructure measured by 1H NMR relaxometry, Cem. Concr. Res. (2019). https://doi.org/10.1016/j.cemconres.2019.05.002.

[63]   C. Duan, R. Karnik, M.C. Lu, A. Majumdar, Evaporation-induced cavitation in nanofluidic channels, Proc. Natl. Acad. Sci. U. S. A. (2012). https://doi.org/10.1073/pnas.1014075109.

[64]   T.D. Wheeler, A.D. Stroock, Stability limit of liquid water in metastable equilibrium with subsaturated vapors, Langmuir. (2009). https://doi.org/10.1021/la9002725.

[65]   F. Caupin, A.D. Stroock, The Stability Limit and other Open Questions on Water at Negative Pressure, in: 2013. https://doi.org/10.1002/9781118540350.ch3.

[66]   I. Maruyama, J. Rymeš, M. Vandamme, B. Coasne, Cavitation of water in hardened cement paste under short-term desorption measurements, Mater. Struct. Constr. (2018). https://doi.org/10.1617/s11527-018-1285-x.

[67]   Q. Zheng, D.J. Durben, G.H. Wolf, C.A. Angell, Liquids at large negative pressures: Water at the homogeneous nucleation limit, Science (80-.). (1991). https://doi.org/10.1126/science.254.5033.829.

[68]   P.R. Williams, R.L. Williams, On anomalously low values of the tensile strength of water, Proc. R. Soc. A Math. Phys. Eng. Sci. (2000). https://doi.org/10.1098/rspa.2000.0564.

[69]   A Practical Guide to Microstructural Analysis of Cementitious Materials, 2018. https://doi.org/10.1201/b19074.

[70]   J. Zhang, G.W. Scherer, Comparison of methods for arresting hydration of cement, Cem. Concr. Res. (2011). https://doi.org/10.1016/j.cemconres.2011.06.003.

[71]   C. Gallé, Effect of drying on cement-based materials pore structure as identified by mercury intrusion porosimetry - A comparative study between oven-, vacuum-, and freeze-drying, Cem. Concr. Res. (2001). https://doi.org/10.1016/S0008-8846(01)00594-4.

[72]   A. Korpa, R. Trettin, The influence of different drying methods on cement paste microstructures as reflected by gas adsorption: Comparison between freeze-drying

(F-drying), D-drying, P-drying and oven-drying methods, Cem. Concr. Res. (2006). https://doi.org/10.1016/j.cemconres.2005.11.021.

[73] S. Tada, K. Watanabe, Dynamic determination of sorption isotherm of cement based materials, Cem. Concr. Res. (2005). https://doi.org/10.1016/j.cemconres.2005.01.002.

[74] M.S. Åhs, Sorption scanning curves for hardened cementitious materials, Constr. Build. Mater. (2008). https://doi.org/10.1016/j.conbuildmat.2007.08.009.

[75] R.M. Kowalczyk, A.M. Gajewicz, P.J. Mcdonald, The mechanism of water-isopropanol exchange in cement pastes evidenced by NMR relaxometry, RSC Adv. (2014). https://doi.org/10.1039/c4ra00889h.

[76] A.M. Gajewicz, E. Gartner, K. Kang, P.J. McDonald, V. Yermakou, A 1H NMR relaxometry investigation of gel-pore drying shrinkage in cement pastes, Cem. Concr. Res. (2016). https://doi.org/10.1016/j.cemconres.2016.04.013.

[77] A. Gajewicz, Characterisation of cement microstructure and pore – water interaction by 1H Nuclear Magnetic Resonance Relaxometry, Dep. Phys. Sci. (2014).

[78] A. Malijevsk, G. Jackson, A perspective on the interfacial properties of nanoscopic liquid drops, J. Phys. Condens. Matter. (2012). https://doi.org/10.1088/0953-8984/24/46/464121.

[79] L. Gránásy, Cahn-Hilliard-type density functional calculations for homogeneous ice nucleation in undercooled water, J. Mol. Struct. (1999). https://doi.org/10.1016/S0022-2860(99)00095-2.

[80] G.S. Haar, L., Gallagher, J.S. and Kell, National Bureau of Standards/National Research Council Steam Tables, (1984).

[81] M. Blander, J.L. Katz, Bubble nucleation in liquids, AIChE J. (1975). https://doi.org/10.1002/aic.690210502.

[82] J.C. Fisher, The fracture of liquids, J. Appl. Phys. (1948). https://doi.org/10.1063/1.1698012.

[83] G.W. Scherer, D.M. Smith, Cavitation during drying of a gel, J. Non. Cryst. Solids. (1995). https://doi.org/10.1016/0022-3093(95)00222-7.

[84] F.F. Abraham, The Nature of the Nucleation Process, in: Homog. Nucleation Theory, 1974. https://doi.org/10.1016/b978-0-12-038361-0.50007-7.

[85] M.C. Sukop, D. Or, Lattice Boltzmann method for homogeneous and heterogeneous cavitation, Phys. Rev. E - Stat. Nonlinear, Soft Matter Phys. (2005). https://doi.org/10.1103/PhysRevE.71.046703.

[86]   G. Menzl, M.A. Gonzalez, P. Geiger, F. Caupin, J.L.F. Abascal, C. Valeriani, C. Dellago, Molecular mechanism for cavitation in water under tension, Proc. Natl. Acad. Sci. U. S. A. (2016). https://doi.org/10.1073/pnas.1608421113.

[87]   C.J. Rasmussen, G.Y. Gor, A. V. Neimark, Monte Carlo simulation of cavitation in pores with nonwetting defects, Langmuir. (2012). https://doi.org/10.1021/la300078k.

[88]   E.P. Barrett, L.G. Joyner, P.P. Halenda, The Determination of Pore Volume and Area Distributions in Porous Substances. I. Computations from Nitrogen Isotherms, J. Am. Chem. Soc. (1951). https://doi.org/10.1021/ja01145a126.

[89]   R. Badmann, N. Stockhausen, M.J. Setzer, The statistical thickness and the chemical potential of adsorbed water films, J. Colloid Interface Sci. (1981). https://doi.org/10.1016/0021-9797(81)90395-7.

[90]   J. Hagymassy, S. Brunauer, R.S. Mikhail, Pore structure analysis by water vapor adsorption. I. t-Curves for water vapor, J. Colloid Interface Sci. (1969). https://doi.org/10.1016/0021-9797(69)90132-5.

[91]   P. Alto, The International Association for the Properties of Water and Steam, Water. (2008).

[92]   G. Sant, A. Eberhardt, D. Bentz, J. Weiss, Influence of Shrinkage-Reducing Admixtures on Moisture Absorption in Cementitious Materials at Early Ages, J. Mater. Civ. Eng. (2010). https://doi.org/10.1061/(asce)0899-1561(2010)22:3(277).

[93]   J. Weiss, P. Lura, F. Rajabipour, G. Sant, Performance of shrinkage-reducing admixtures at different humidities and at early ages, ACI Mater. J. (2008). https://doi.org/10.14359/19977.

[94]   E. Gallucci, X. Zhang, K.L. Scrivener, Effect of temperature on the microstructure of calcium silicate hydrate (C-S-H), Cem. Concr. Res. (2013). https://doi.org/10.1016/j.cemconres.2013.06.008.

[95]   K. Scrivener, A. Ouzia, P. Juilland, A. Kunhi Mohamed, Advances in understanding cement hydration mechanisms, Cem. Concr. Res. (2019). https://doi.org/10.1016/j.cemconres.2019.105823.

[96]   O. Vincent, D.A. Sessoms, E.J. Huber, J. Guioth, A.D. Stroock, Drying by cavitation and poroelastic relaxations in porous media with macroscopic pores connected by nanoscale throats, Phys. Rev. Lett. (2014). https://doi.org/10.1103/PhysRevLett.113.134501.

[97]   B. Lothenbach, F. Winnefeld, C. Alder, E. Wieland, P. Lunk, Effect of temperature on the pore solution, microstructure and hydration products of Portland cement pastes, Cem. Concr. Res. (2007). https://doi.org/10.1016/j.cemconres.2006.11.016.

[98] M. Wu, K. Fridh, B. Johannesson, M. Geiker, Influence of frost damage and sample preconditioning on the porosity characterization of cement based materials using low temperature calorimetry, Thermochim. Acta. (2015). https://doi.org/10.1016/j.tca.2015.03.005.

[99] B. Lothenbach, F. Winnefeld, Thermodynamic modelling of the hydration of Portland cement, Cem. Concr. Res. (2006). https://doi.org/10.1016/j.cemconres.2005.03.001.

[100] P.W. Brown, J. V. Bothe, The stability of ettringite, Adv. Cem. Res. (1993). https://doi.org/10.1680/adcr.1993.5.18.47.

[101] I.G. Richardson, The calcium silicate hydrates, Cem. Concr. Res. (2008). https://doi.org/10.1016/j.cemconres.2007.11.005.

[102] J.W. Bullard, P.E. Stutzman, Analysis of CCRL proficiency cements 151 and 152 using the Virtual Cement and Concrete Testing Laboratory, Cem. Concr. Res. (2006). https://doi.org/10.1016/j.cemconres.2006.05.024.

[103] J.E. Rossen, K.L. Scrivener, Optimization of SEM-EDS to determine the C–A–S–H composition in matured cement paste samples, Mater. Charact. (2017). https://doi.org/10.1016/j.matchar.2016.11.041.

[104] M. Elsalamawy, A.R. Mohamed, E.M. Kamal, The role of relative humidity and cement type on carbonation resistance of concrete, Alexandria Eng. J. (2019). https://doi.org/10.1016/j.aej.2019.10.008.

[105] A.C.A. Muller, K.L. Scrivener, A.M. Gajewicz, P.J. McDonald, Densification of C-S-H measured by 1H NMR relaxometry, J. Phys. Chem. C. (2013). https://doi.org/10.1021/jp3102964.

[106] A.C.A. Muller, K.L. Scrivener, A reassessment of mercury intrusion porosimetry by comparison with 1H NMR relaxometry, Cem. Concr. Res. (2017). https://doi.org/10.1016/j.cemconres.2017.05.024.

[107] G.W. Scherer, J. Valenza, Mechanisms of Frost Damage, Mater. Sci. Concr. VII. (2005).

[108] T. Zhou, K. Ioannidou, F.J. Ulm, M.Z. Bazant, R.J.M. Pellenq, Multiscale poromechanics of wet cement paste, Proc. Natl. Acad. Sci. U. S. A. (2019). https://doi.org/10.1073/pnas.1901160116.

[109] M.J. Abdolhosseini Qomi, L. Brochard, T. Honorio, I. Maruyama, M. Vandamme, Advances in atomistic modeling and understanding of drying shrinkage in cementitious materials, Cem. Concr. Res. (2021). https://doi.org/10.1016/j.cemconres.2021.106536.

[110] J.J. Chen, J.J. Thomas, H.F.W. Taylor, H.M. Jennings, Solubility and structure of calcium silicate hydrate, Cem. Concr. Res. (2004). https://doi.org/10.1016/j.cemconres.2004.04.034.

[111] S. Soyer-Uzun, S.R. Chae, C.J. Benmore, H.R. Wenk, P.J.M. Monteiro, Compositional evolution of calcium silicate hydrate (C-S-H) structures by total X-ray scattering, J. Am. Ceram. Soc. (2012). https://doi.org/10.1111/j.1551-2916.2011.04989.x.

[112] X. Cong, R. James Kirkpatrick, 29Si MAS NMR study of the structure of calcium silicate hydrate, Adv. Cem. Based Mater. (1996). https://doi.org/10.1016/s1065-7355(96)90046-2.

[113] G. Renaudin, J. Russias, F. Leroux, F. Frizon, C. Cau-dit-Coumes, Structural characterization of C-S-H and C-A-S-H samples-Part I: Long-range order investigated by Rietveld analyses, J. Solid State Chem. (2009). https://doi.org/10.1016/j.jssc.2009.09.026.

[114] I.G. Richardson, Model structures for C-(A)-S-H(I), Acta Crystallogr. Sect. B Struct. Sci. Cryst. Eng. Mater. (2014). https://doi.org/10.1107/S2052520614021982.

[115] M.J.A. Qomi, M. Bauchy, F.J. Ulm, R.J.M. Pellenq, Anomalous composition-dependent dynamics of nanoconfined water in the interlayer of disordered calcium-silicates, J. Chem. Phys. (2014). https://doi.org/10.1063/1.4864118.

[116] A.J. Allen, J.J. Thomas, H.M. Jennings, Composition and density of nanoscale calcium-silicate-hydrate in cement, Nat. Mater. (2007). https://doi.org/10.1038/nmat1871.

[117] K. Fujii, W. Kondo, Heterogeneous equilibrium of calcium silicate hydrate in water at 30 °c, J. Chem. Soc. Dalt. Trans. (1981). https://doi.org/10.1039/DT9810000645.

[118] E. L'Hôpital, B. Lothenbach, D.A. Kulik, K. Scrivener, Influence of calcium to silica ratio on aluminium uptake in calcium silicate hydrate, Cem. Concr. Res. (2016). https://doi.org/10.1016/j.cemconres.2016.01.014.

[119] A. Kumar, K. Scrivener, P. Bowen, Synthesis of nano-structured calcium silicate hydrate, in: NSTI Adv. Mater. - TechConnect Briefs 2015, 2015.

[120] K.S. Harris Maya, Simpson Grace, Bowen Paul, A method for the reliable and reproducible precipitation of phase pure high Ca/Si ratio (>1.5) synthetic calcium silicate hydrates (C-S-H), 2021.

[121] M. Benaicha, A. Belcaid, A.H. Alaoui, O. Jalbaud, Y. Burtschell, Effects of limestone filler and silica fume on rheology and strength of self-compacting concrete, Struct. Concr. (2019). https://doi.org/10.1002/suco.201900150.

[122] K.T. Koh, S.H. Park, G.S. Ryu, G.H. An, B.S. Kim, Effect of the type of silica fume and filler on mechanical properties of ultra high performance concrete, in: Key Eng. Mater., 2018. https://doi.org/10.4028/www.scientific.net/KEM.774.349.

[123] Effect of Silica Fume on Workability and Compressive Strength of OPC Concrete, J. Environ. Nanotechnol. (2014). https://doi.org/10.13074/jent.2014.09.143086.

[124] M. Li, Y. Wang, H. Jiang, C. Zheng, Z. Guo, Synthesis, characterization and mechanism of polycarboxylate superplasticizer with slump retention capability, in: IOP Conf. Ser. Mater. Sci. Eng., 2017. https://doi.org/10.1088/1757-899X/182/1/012036.

[125] M.M.A. El-Sukkary, N.O. Shaker, D.A. Ismail, S.M. Ahmed, A.I. Awad, Preparation and evaluation of some amide ether carboxylate surfactants, Egypt. J. Pet. (2012). https://doi.org/10.1016/j.ejpe.2012.02.002.

[126] X. Liu, Z. Wang, J. Zhu, Y. Zheng, S. Cui, M. Lan, H. Li, Synthesis, characterization and performance of a polycarboxylate superplasticizer with amide structure, Colloids Surfaces A Physicochem. Eng. Asp. (2014). https://doi.org/10.1016/j.colsurfa.2014.02.022.

[127] J. Dey, S. Shrivastava, Can molecules with an anionic head and a poly(ethylene glycol) methyl ether tail self-assemble in water? A surface tension, fluorescence probe, light scattering, and transmission electron microscopic investigation, Soft Matter. (2012). https://doi.org/10.1039/c2sm06931h.

[128] T.C. Powers, T.L. Brownyard, Studies of the Physical Properties of Hardened Portland Cement Paste Part 3. Theoretical Interpretation of adsorption Data, J. Am. Concr. Inst. (1946).

[129] E.H. Atlassi, Influence of Silica Fume on the Pore Structure of Mortar when Measured by Water Vapour Sorption Isotherms, in: Model. Microstruct. Its Potential Stud. Transp. Prop. Durab., 1996. https://doi.org/10.1007/978-94-015-8646-7_12.

[130] D.H. Everett, Reporting data on adsorption from solution at the SOlid/SOlution interface (Recommendations 1986), Pure Appl. Chem. (1986). https://doi.org/10.1351/pac198658070967.

[131] M.L. Lakhanpal, E.A. Flood, Stresses and strains in adsorbate–adsorbent systems: iv. Contractions of activated carbon on adsorption of gases and vapors at low initial pressures, Can. J. Chem. (1957). https://doi.org/10.1139/v57-121.

[132] B.V. Derjaguin, N.V. Churaev, V.M. Muller, Wetting Films. In: Surface Forces., Springer. (1987).

[133] N. V. Churaev, M.J. Setzer, J. Adolphs, Influence of surface wettability on adsorption isotherms of water vapor, J. Colloid Interface Sci. (1998). https://doi.org/10.1006/jcis.1997.5292.

[134] J. Adolphs, Excess surface work-A modelless way of getting surface energies and specific surface areas directly from sorption isotherms, Appl. Surf. Sci. (2007). https://doi.org/10.1016/j.apsusc.2006.12.089.

[135] P. Schiller, M. Wahab, T. Bier, H.J. Mögel, A model for sorption hysteresis in hardened cement paste, Cem. Concr. Res. (2019).

https://doi.org/10.1016/j.cemconres.2019.05.005.

[136] H.T. Nguyen, S. Rahimi-Aghdam, Z.P. Bažant, Sorption isotherm restricted by multilayer hindered adsorption and its relation to nanopore size distribution, J. Mech. Phys. Solids. (2019). https://doi.org/10.1016/j.jmps.2019.03.003.

[137] N. Fischer, R. Haerdtl, P.J. McDonald, Observation of the redistribution of nanoscale water filled porosity in cement based materials during wetting, Cem. Concr. Res. (2015). https://doi.org/10.1016/j.cemconres.2014.10.013.

[138] D.K. Panesar, J. Francis, Influence of limestone and slag on the pore structure of cement paste based on mercury intrusion porosimetry and water vapour sorption measurements, Constr. Build. Mater. (2014). https://doi.org/10.1016/j.conbuildmat.2013.11.022.

[139] A. Kumar, S. Ketel, K. Vance, T. Oey, N. Neithalath, G. Sant, Water Vapor Sorption in Cementitious Materials-Measurement, Modeling and Interpretation, Transp. Porous Media. (2014). https://doi.org/10.1007/s11242-014-0288-5.

[140] Q. Zeng, D. Zhang, K. Li, Kinetics and Equilibrium Isotherms of Water Vapor Adsorption/Desorption in Cement-Based Porous Materials, Transp. Porous Media. (2015). https://doi.org/10.1007/s11242-015-0531-8.

[141] D. Zhang, X. Pang, K. Li, Water vapor sorption isotherm of cement-based porous materials, Kuei Suan Jen Hsueh Pao/Journal Chinese Ceram. Soc. (2015). https://doi.org/10.14062/j.issn.0454-5648.2015.05.01.

[142] C. Ahlneck, G. Zografi, The molecular basis of moisture effects on the physical and chemical stability of drugs in the solid state, Int. J. Pharm. (1990). https://doi.org/10.1016/0378-5173(90)90221-O.

[143] B.C. Hancock, G. Zografi, Characteristics and Significance of the Amorphous State in Pharmaceutical Systems, J. Pharm. Sci. (1997). https://doi.org/10.1021/js9601896.

[144] S.L. Shamblin, G. Zografi, The effects of absorbed water on the properties of amorphous mixtures containing sucrose, Pharm. Res. (1999). https://doi.org/10.1023/A:1018960405504.

[145] J. Zhang, G. Zografi, The relationship between 'BET'- and 'Free Volume'-derived parameters for water vapor absorption into amorphous solids, J. Pharm. Sci. (2000). https://doi.org/10.1002/1520-6017(200008)89:8<1063::AID-JPS11>3.0.CO;2-0.

[146] E. Bernard, Y. Yan, B. Lothenbach, Effective cation exchange capacity of calcium silicate hydrates (C-S-H), Cem. Concr. Res. (2021). https://doi.org/10.1016/j.cemconres.2021.106393.

[147] S. Kittaka, S. Ishimaru, M. Kuranishi, T. Matsuda, T. Yamaguchi, Enthalpy and interfacial free energy changes of water capillary condensed in mesoporous silica,

MCM-41 and SBA-15, Phys. Chem. Chem. Phys. (2006). https://doi.org/10.1039/b518365k.

[148] K.K. Aligizaki, Pore Structure of Cement-Based Materials, 2005. https://doi.org/10.1201/9781482271959.

[149] W.S. Chiang, E. Fratini, P. Baglioni, D. Liu, S.H. Chen, Microstructure determination of calcium-silicate-hydrate globules by small-angle neutron scattering, J. Phys. Chem. C. (2012). https://doi.org/10.1021/jp300745g.

[150] S. Grangeon, F. Claret, Y. Linard, C. Chiaberge, X-ray diffraction: A powerful tool to probe and understand the structure of nanocrystalline calcium silicate hydrates, Acta Crystallogr. Sect. B Struct. Sci. Cryst. Eng. Mater. (2013). https://doi.org/10.1107/S2052519213021155.

[151] R.F. Feldman, P.J. Sereda, A New Model for Hydrated Portland Cement and its Practical Implications, Eng. J. (1970).

[152] J. Rouquerol, P. Llewellyn, F. Rouquerol, Is the BET equation applicable to microporous adsorbents?, Stud. Surf. Sci. Catal. (2007). https://doi.org/10.1016/s0167-2991(07)80008-5.

[153] J.J. Beaudoin, P. Gu, J. Marchand, B. Tamtsia, R.E. Myers, Z. Liu, Solvent replacement studies of hydrated portland cement systems: The role of calcium hydroxide, Adv. Cem. Based Mater. (1998). https://doi.org/10.1016/S1065-7355(98)00008-X.

[154] Z. Zhang, G.W. Scherer, Physical and chemical effects of isopropanol exchange in cement-based materials, Cem. Concr. Res. (2021). https://doi.org/10.1016/j.cemconres.2021.106461.

[155] I. Stavrakas, D. Triantis, S.K. Kourkoulis, E.D. Pasiou, I. Dakanali, Acoustic emission analysis of cement mortar specimens during three point bending tests, Lat. Am. J. Solids Struct. (2016). https://doi.org/10.1590/1679-78252486.

[156] D. Kocáb, L. Topolář, B. Kucharczyková, R. Halamová, The analysis of acoustic emission signals detected during the loading of cement-based materials, Eng. Fail. Anal. (2019). https://doi.org/10.1016/j.engfailanal.2019.01.002.

[157] Q. Gu, Q. Ma, Y. Tan, Z. Jia, Z. Zhao, D. Huang, Acoustic emission characteristics and damage model of cement mortar under uniaxial compression, Constr. Build. Mater. (2019). https://doi.org/10.1016/j.conbuildmat.2019.04.090.

[158] J.P. Kaufmann, Experimental identification of ice formation in small concrete pores, Cem. Concr. Res. (2004). https://doi.org/10.1016/j.cemconres.2004.01.022.

[159] T.J. Chotard, J. Barthelemy, A. Smith, N. Gimet-Breat, M. Huger, D. Fargeot, C. Gault, Acoustic emission monitoring of calcium aluminate cement setting at the early age, J. Mater. Sci. Lett. (2001). https://doi.org/10.1023/A:1010942005907.

[160] T.J. Chotard, A. Smith, D. Rotureau, D. Fargeot, C. Gault, Acoustic emission characterisation of calcium aluminate cement hydration at an early stage, J. Eur. Ceram. Soc. (2003). https://doi.org/10.1016/S0955-2219(02)00152-8.

[161] F. Mallamace, M. Broccio, C. Corsaro, A. Faraone, D. Majolino, V. Venuti, L. Liu, C.Y. Mou, S.H. Chen, Evidence of the existence of the low-density liquid phase in supercooled, confined water, Proc. Natl. Acad. Sci. U. S. A. (2007). https://doi.org/10.1073/pnas.0607138104.

[162] A. Vasylieva, I. Doroshenko, Y. Vaskivskyi, Y. Chernolevska, V. Pogorelov, FTIR study of condensed water structure, J. Mol. Struct. (2018). https://doi.org/10.1016/j.molstruc.2018.05.002.

[163] B. Baumgartner, J. Hayden, J. Loizillon, S. Steinbacher, D. Grosso, B. Lendl, Pore Size-Dependent Structure of Confined Water in Mesoporous Silica Films from Water Adsorption/Desorption Using ATR-FTIR Spectroscopy, Langmuir. (2019). https://doi.org/10.1021/acs.langmuir.9b01435.

[164] R. Kjellander, S. Marcělja, Correlation and image charge effects in electric double layers, Chem. Phys. Lett. (1984). https://doi.org/10.1016/0009-2614(84)87039-6.

[165] B. Jönsson, A. Nonat, C. Labbez, B. Cabane, H. Wennerström, Controlling the cohesion of cement paste, Langmuir. (2005). https://doi.org/10.1021/la051048z.

[166] R.J.M. Pellenq, N. Lequeux, H. van Damme, Engineering the bonding scheme in C-S-H: The iono-covalent framework, Cem. Concr. Res. (2008). https://doi.org/10.1016/j.cemconres.2007.09.026.

[167] J. Zhong, M.A. Alibakhshi, Q. Xie, J. Riordon, Y. Xu, C. Duan, D. Sinton, Exploring Anomalous Fluid Behavior at the Nanoscale: Direct Visualization and Quantification via Nanofluidic Devices, Acc. Chem. Res. (2020). https://doi.org/10.1021/acs.accounts.9b00411.

Curriculum Vitae

Monisha RASTOGI

Leimen, Baden-Württemberg, Germany

✉ monisharastogiepfl@gmail.com   📞 +49-1747349221

Summary

- Experienced researcher with training in thermal analysis and characterization of a variety of materials including catalysts, glasses, and cementitious materials.
- Author and co-author of several original research articles, reviews, and letters in peer-reviewed journals.
- Active contributions to massive open online courses (MOOCs) for EPFL.

Education

EPFL
École Polytechnique fédérale de Lausanne, Switzerland
Doctor of Philosophy – PhD
2018 – 2021

universität innsbruck
Leopold-Franzens Universität Innsbruck, Austria
Research associate, Ion Physics and Applied Physics
2016 - 2017

Indian Institute of Technology, Mandi, India
Master of Science, Materials Science, CGPA: 9
Thesis: Ceramics, glasses, and cement for photocatalytic applications.
2014 – 2016

Uttar Pradesh Technical University
Bachelor's in Mechanical Engineering, CGPA: 8
2008 – 2012

Awards and scholarships

- Marie Skłodowska Curie Fellowship for pursuing an industrial doctorate at HeidelbergCement Technology centre with the academic partner, EPFL . **(2018)**
- Doktoratskolleg Atoms, Light, and Molecules scholarship, Austria for pursuing doctorate in Austria. **(2016)**
- Second place in the national level competition of prototype development for environmental remediation, India. **(2015)**
- GATE scholarship for master's studies, Ministry of Human Resources Development, India. **(2014)**

Selected publications

- M Rastogi et. al. Janus nanostructures for heterogeneous photocatalysis. Applied Physics Reviews. **2018**, 5, 041111. *(Editor' s pick, awarded 200 USD)*
- Rastogi et. al. Lithium ions solvated in helium. Physical Chemistry Chemical Physics. **2018**, 381, 25569-25576. *(Cover article).*
- M Rastogi *et al.* 'Reaping the benefits of ferroelectricity in selectively precipitated lithium niobate microcrystals in silica matrix for photocatalysis.' **2016** Applied Physics Letters 109 (22),223901.
- M Rastogi, R Vaish, 'Visible light-induced water detoxification through Portland cement composites reinforced with photocatalytic filler: A leap away from TiO_2.' Construction and Building Materials, **2016**, 120, 364-372.
- M Rastogi et al. 'The role of cavitation in drying cementitious materials.' arXiv preprint arXiv:2101.02433, **2021**

Personal information

Date of birth: 7.12.1990

Languages: English (Fluent), German (B1), Hindi (native)

Nationality: Indian